The Role of Cilia Motility in Axial Morphogenesis

by

Zoe Irons

A dissertation accepted and approved in partial fulfillment of the
requirements for the degree of
Doctor of Philosophy
in Biology

Dissertation Committee:
Dr. Judith Eisen, Chair
Dr. Daniel T. Grimes, Advisor
Dr. Adam Miller, Core Member
Dr. Victoria Herman, Core Member
Dr. Michael Harms, Institutional Representative

University of Oregon

Spring 2024

© 2024 Zoe Irons

DISSERTATION ABSTRACT

Zoe Irons

Doctor of Philosophy in Biology

Title: The Role of Cilia Motility in Axial Morphogenesis

The spine is the core of the vertebrate body axis, providing structural support and playing a role in establishing body shape. The linearity of the spine is essential for proper function. Scoliosis, or curvature of the spine, is present in 3-4% of the human population and can cause chronic pain as well as compression of the lungs and heart in severe cases. In this dissertation, I used zebrafish to study the role of cilia motility in morphogenesis of the body axis and the development of scoliosis. Previous work has established cilia motility as essential for zebrafish embryos to uncurl their bodies from around the yolk during the first 24 hours post fertilization. In Chapter I, I found that the protein Daw1 regulates the timely onset of cilia motility, and that embryos are able to remodel their body axes up to 3 days post fertilization.

In Chapter II, I investigated factors functioning downstream of cilia motility that control body and spine morphogenesis. The Reissner fiber assembles downstream of cilia motility. Using zebrafish lacking Daw1, I showed that this fiber also assembles in response to a delayed cilia motility cue. The expression of the Urotensin-like peptides, Urp1 and Urp2, is increased as a result of cilia motility in the central canal. By generating mutants lacking both peptides, I showed that these peptides are dispensable for early body morphogenesis, but critical for the

maintenance of spinal straightness in adulthood. This work revealed new components of spinal morphology that could be playing roles in human scoliosis.

Lastly, in Chapter IV I investigated the mechanism stops further morphogenetic tissue movements once a linear body axis is generated. This occurs in embryos lacking Pkd2, a calcium ion channel known to play a role in flow sensory pathways. Using epistatic tests, I showed that *pkd2* acts in a pathway independent of cilia motility and fluid flow to prevent axis over-straightening. Collectively, this dissertation advances our understanding of the role of cilia motility, fluid flow, and downstream factors in body axis straightening and the maintenance of spinal straightness.

This work contains both unpublished and published co-authored materials.

CURRICULUM VITAE

NAME OF AUTHOR: Zoe Irons

GRADUATE AND UNDERGRADUATE SCHOOLS ATTENDED:

University of Oregon, Eugene OR
Dickinson College, Carlisle PA

DEGREES AWARDED:

Doctor of Philosophy, Biology, 2024, University of Oregon
Bachelor of Science, Biochemistry and Molecular Biology, 2018, Dickinson College

AREAS OF SPECIAL INTEREST:

Developmental Biology
Molecular Biology
Genetics

PROFESSIONAL EXPERIENCE:

Graduate Teaching Assistant, Department of Biology, University of Oregon,
Eugene, OR, 2018-2019

Undergraduate Teaching Assistant, Dickinson College,
Carlisle, PA, 2015-2018

Undergraduate Research Assistant, Department of Biology, Dickinson College,
Carlisle, PA, 2016-2017

Laboratory Technician, Yale University Child Study Center,
New Haven, CT, 2015

GRANTS, AWARDS, AND HONORS:

DeLill Nasser Travel Award for Professional Development in Genetics, University of Oregon, 2023

Pete von Hippel Graduate Scholar Award, University of Oregon, 2022

Society for Developmental Biology Student Travel Award
University of Oregon, 2022

NIH F31 Predoctoral Fellowship, Discovering Mechanisms Underlying the Formation of a Straight Body Axis, University of Oregon, 2021

NIH T32 – Developmental Biology Training Grant, University of Oregon, 2019

Roethenmund International Travel Award, Dickinson College, 2017

PUBLICATIONS:

Bearce, E. A., Irons, Z. H., O'Hara-Smith, J. R., Kuhns, C. J., Fisher, S. I., Crow, W. E., & Grimes, D. T. (2022). Urotensin II-related peptides, Urp1 and Urp2, control zebrafish spine morphology. *Elife*, *11*. https://doi.org/10.7554/eLife.83883

Leslie, J. S., Hjeij, R., Vivante, A., Bearce, E. A., Dyer, L., Wang, J., Rawlins, L., Kennedy, J., Ubeyratna, N., Fasham, J., Irons, Z. H., Craig, S. B., Koenig, J., George, S., Pode-Shakked, B., Bolkier, Y., Barel, O., Mane, S., Frederiksen, K. K., . . . Baple, E. L. (2022). Biallelic DAW1 variants cause a motile ciliopathy characterized by laterality defects and subtle ciliary beating abnormalities. *Genet Med*, *24*(11), 2249-2261. https://doi.org/10.1016/j.gim.2022.07.019

Bearce, E. A.*, Irons, Z. H.*, Craig, S. B., Kuhns, C. J., Sabazali, C., Farnsworth, D. R., Miller, A. C., & Grimes, D. T. (2022). Daw1 regulates the timely onset of cilia motility during development. *Development*, *149*(12). https://doi.org/10.1242/dev.200017

Garno, C., Irons, Z. H., Gamache, C. M., McKim, Q., Reyes, G., Wu, X., Shuster, C. B., & Henson, J. H. (2021). Building the cytokinetic contractile ring in an early embryo: Initiation as clusters of myosin II, anillin and septin, and visualization of a septin filament network. *PLoS One*, *16*(12), e0252845. https://doi.org/10.1371/journal.pone.0252845

Grimes, D. T., Patterson, V. L., Luna-Arvizu, G., Schottenfeld-Roames, J., Irons, Z. H., & Burdine, R. D. (2020). Left-right asymmetric heart jogging increases the robustness of dextral heart looping in zebrafish. *Dev Biol*, *459*(2), 79-86. https://doi.org/10.1016/j.ydbio.2019.11.012

ACKNOWLEDGMENTS

First and foremost, I would like to thank my advisor, Dr. Dan Grimes, for his support and mentorship during this project. He accepted me as a rotation student when the lab barely existed, brought me to my first conference of graduate school that very same term, and throughout my entire graduate education continued to help me become the scientist I am today. I truly could not have asked for a better mentor during this process. He regularly challenged me to try new techniques, pursue unique opportunities, and think critically about my experimental results. When I entered graduate school, my father (who also completed a Ph.D.) reminded me it was a marathon, not a sprint, and it would be important to find people that could get me over the finish line. Dr. Grimes, along with every member of my wonderful and supportive dissertation committee: Drs. Judith Eisen, Adam Miller, Tory Herman, and Michael Harms were all instrumental in this pursuit, and I would not have half the success I have achieved without them. Thank you also to my collaborators outside of the University of Oregon, Drs. Joe Leslie and Emma Baple at the University of Exeter Medical School, who kindly shared resources and data that exponentially increased the depth and breadth of my first project.

I would also like to thank the funding sources for this project, which allowed me to devote all my energy to research at graduate school. I was supported by an NIH T32 Fellowship (T32 HD007348), F31 Fellowship (F31 HD105435), and an NIH R00 (R00 AR70905) and R35 (R35 GM142949) awarded to Dr. Grimes at the University of Oregon.

Next, I would like to thank Dr. Elizabeth Bearce, who contributed massively to this body of work, and was an absolute joy to collaborate with an almost every project. They taught me so much about being a scientist over the years, and were always there for me both in and out of the

lab to commiserate, cat-sit, or exchange memes about Dungeons and Dragons. Sitting in front of a microscope for hours was never more fun, and it was an honor to have them by my side for every triumph and failure. I think, after five years and endlessly patiently re-delivered lessons, I finally have a loose grasp of how to process videos on Fiji.

And of course I would like to thank my other colleagues in lab, current and former, for their contributions to this work in practice or in spirit, making the Grimes Lab an incredible place to work for the past several years. In particular, John O'Hara-Smith, Samuel Craig, Colin Kuhns, and Gabriel Luna-Arvizu made significant contributions to this work and I am very grateful. Judy Peirce helped me take excellent care of all my fish, and very patiently looked at lots of cat photos.

I would like to thank my mentors and professors at Dickinson College who introduced me to research whose instruction and guidance could not have prepared me better for graduate school. Their faith in me has meant so much, and I am so excited to return as a visiting assistant professor this coming year.

And finally, a million thanks to my friends and family who have supported me over the years. To my parents, for reminding me to call more often and providing me a refuge whenever I needed it. To my aunt and uncle in Berkeley for being my home away from home. To the staff at Greenhill Humane Society, where I spent every Sunday from 2 to 5, and to Arwen, my sweet, sassy, fluffy cuddle buddy. To Collin H., for his endless patience.

DEDICATION

To my parents, for showing me it could be done

TABLE OF CONTENTS

Chapter Page

I. INTRODUCTION 16

II. DAW1 REGULATES THE TIMELY ONSET OF CILIA MOTILITY DURING DEVELOPMENT 24

Introduction 24

Results 29

daw1^{b1403} mutants exhibit phenotypes of cilia motility mutants at early stages, but not later stages. 29

daw1^{b1403} mutants exhibit delayed onset of robust cilia motility in the central canal 37

daw1^{b1403} mutants contain a loss-of-function allele. 39

Zebrafish embryos are able to recover from CTD upon return of cilia motility up to 3 days post fertilization. 42

Phenotypes seen in *daw1*^{b1403} zebrafish mutants model symptoms seen in patients with mutations in *DAW1* 46

Discussion 49

Bridge to Chapter III 53

III. THE REISSNER FIBER IS REQUIRED FOR EARLY AXIS STRAIGHTENING, WHILE UROTENSIN II-RELATED PEPTIDES ARE REQUIRED FOR LONG-TERM MAINTENANCE OF THE SPINE 54

Introduction 54

Results 56

sspo^{b1446} mutants exhibit curly tail down, and the Reissner fiber fails to assemble in the absence of cilia motility 56

Chapter Page

Urp1 and Urp2 peptides are dispensable for embryonic axial straightening ... 60

Urp1 and Urp2 function semi-redundantly to maintain spine morphology 65

Urp1 and Urp2 signal through the Uts2r3 receptor to control spine morphology ... 69

Discussion ... 70

Bridge to Chapter IV ... 75

IV. CHAPTER IV: PKD2 ACTS INDEPENDENTLY OF MOTILE CILIA AND FLUID FLOW TO PREVENT AXIS OVER-STRAIGHTENING ... 76

Introduction ... 76

Results ... 78

Zebrafish embryos develop curly tail up in the absence of Pkd2 or Pkd1 and Pkd1b ... 78

Curly tail up occurs independently of Urp1 and Urp2 ... 83

Pkd2 functions downstream of cilia motility or in a parallel pathway ... 84

Investigating a notochord-specific role of Pkd2 in axial straightening ... 86

Assessing the role of the Pkd2 ciliary localization motif in development ... 88

Discussion ... 89

V. CONCLUDING REMARKS ... 92

APPENDICES ... 96

A. MATERIALS AND METHODS ... 96

B. TABLES ... 109

C. MOVIE LEGENDS ... 116

Chapter Page

REFERENCES CITED.. 120

LIST OF FIGURES

Figure Page

1.1. Zebrafish embryos gradually uncurl from the yolk during the first 32 hpf. 19

1.2. Types of axial defects in zebrafish embryos. 19

1.3. Model of axial straightening. 23

2.1. *daw1*^{b1403} mutants exhibit motile cilia-associated defects. 30

2.2. Schematic of the *daw1*^{b1403} mutation. 31

2.3. μCT and calcein staining of *daw1*^{b1403} mutants and sibling controls. 32

2.4. Expression of *daw1* across 1-5 d.p.f. zebrafish larvae from a single-cell RNA sequencing atlas. 33

2.5. Body axis curvature self-corrects after delayed onset cilia motility. 35

2.6. Axial phenotypes and central canal cilia in *daw1*^{b1403} mutants. 36

2.7. Cilia kymograph and frequency data from live imaging in the central canal..... 37

2.8. *daw1*^{b1403} encodes a loss-of-function protein.. 38

2.9. *daw1* crispants phenocopy mutants and are rescued by over-expression of wild-type, but not *daw1*^{b1403} mRNA. 40

2.10. *daw1*^{b1422} mutants harbor a large deletion and premature truncation codon and phenocopy *daw1*^{b1403} mutants. 41

2.11. Self-correction of curves can occur throughout developmental stages. 43

2.12. Body axis curvature in *cfap298*^{tm304} mutants is temperature dependent............ 44

2.13. Body axis recovery in *cfap298*^{tm304} mutants after temperature shifts. 45

2.14. In vivo modeling of *DAW1* variants using zebrafish mutants. 47

Figure Page

3.1. *sspo*^{b1446} mutants display CTD due to their inability to form a Reissner fiber. .. 57

3.2. The Reissner fiber assembles in a delayed fashion in *daw1*^{b1403} mutants.......... 59

3.3. Urp1 and Urp2 are dispensable for axial straightening. 62

3.4. Generation of *urp1*$^{\Delta P}$ and *urp2*$^{\Delta P}$ mutants. 64

3.5. Phenotyping spinal curves. 66

3.6. Spinal curves in *urp1*$^{\Delta P}$, *urp2*$^{\Delta P}$, *urp1*$^{\Delta P}$*;urp2*$^{\Delta P}$*,* and *pkd2l1*^{icm02} mutants degenerate with age.. 67

3.7. Urp1 and Urp2 are required for proper adult spine morphology. 68

3.8. Generation of *uts2r3*^{b1436} mutants.. 70

4.1. Zebrafish embryos lacking *pkd2* develop curly tail up by 28 hpf...................... 80

4.2. *pkd1*^{b1428}*;pkd1b*^{b1442} mutants develop CTU without left-right patterning defects. 82

4.3. *pkd2* mutants develop CTU in the absence of cilia motility and the Reissner fiber. 85

4.4. *pkd2* is not necessary in the notochord to prevent CTU. 87

4.5. Mutations in *pkd2* near the ciliary targeting motif do not cause CTU............... 89

LIST OF TABLES

Table Page

1. Mutant Fish Lines 109

2. Oligonucleotides for Mutagenesis 110

3. Oligonucleotides for CRISPR/Cas9 Mosaic Mutagenesis 112

4. Miscellaneous Primers 114

CHAPTER I: INTRODUCTION

Chapter I contains unpublished material by me.

Chapter II contains published co-authored material by me and Dr. Elizabeth Bearce, and Dr. Daniel Grimes

Chapter III contains unpublished and published co-authored material by me, Dr. Elizabeth Bearce, and Dr. Daniel Grimes

Chapter IV contains unpublished material by me.

The spine is the center of the vertebrate body axis. It provides internal stability, and serves as a point of connection for other axial structures such as muscle, vasculature, and the nervous system (Bagnat & Gray, 2020). The most common condition associated with spinal morphology is scoliosis, a three-dimensional curvature of the spine. Worldwide, scoliosis occurs in approximately 3% of the population, more commonly in those assigned female at birth (Shakil et al., 2014; Rolton et al., 2014; Haleem et al., 2018). It can be categorized according to age of onset (e.g., infant, adolescent, or adult), or according to etiology: idiopathic, neuromuscular, or congenital (Shakil et al., 2014; Sung et al., 2021). Congenital scoliosis is often diagnosed at birth and characterized by the presence of vertebral deformities (Weiss, 2016). Neuromuscular scoliosis is curvature associated with an underlying condition such as Duchenne muscular dystrophy, in which muscle defects are thought to be the underlying cause of spinal deformities (Archer et al., 2016). However, the most common type of scoliosis is adolescent idiopathic scoliosis (AIS), which is diagnosed in adolescence, and typically onsets during adolescent growth. (Janicki et al., 2007; Sung et al., 2021). In severe cases, spinal curvature can impact both heart and lung function (Janicki et al., 2007; Huh et al., 2015); while highly invasive and expensive, the current most effective treatment is spinal corrective surgery (Shakil et al., 2014; Janicki et al., 2007). While many models and ideas have been proposed, there is still little evidence and few explanations of the underlying mechanisms occurring in AIS.

Many of the first animal models of scoliosis were avian, but due to low genetic tractability, mice quickly became a popular alternative. However, this system is complicated by the fact that quadrupeds experience vastly different biomechanical forces on their spines when compared to humans (Janssen et al., 2011; Terhune et al., 2022), leading to the rise of zebrafish as an alternative (Grimes et al., 2016, Terhune et al., 2022). First documented in guppies, teleost fish are known to develop idiopathic-like scoliosis at a relatively high rate (like humans), unlike quadrupeds, possibly due to biomechanical similarities of swimming through water and standing upright, parallel to the force of gravity (Gorman & Breden, 2009). Since then zebrafish have been successfully used to model scoliosis using mutants that present some attributes AIS (Grimes et al., 2016).

In zebrafish, mutations that disrupt the function of motile cilia invariably cause scoliosis-like spinal curves (Grimes et al., 2016). Cilia are small, hair-like organelles found on the surface of most cells that can be sensory or motile. Motile cilia, on specialized cells, are able to beat back and forth, generating fluid flows within body cavities (Drummond, 2012). In zebrafish, this function is particularly important within the central canal of the spinal canal. Grimes et al. showed that loss of cilia motility during juvenile growth stages, leading to impaired flow of cerebrospinal fluid, causes zebrafish to develop AIS-like spinal curves (Grimes et al., 2016).

In humans, primary ciliary dyskinesia (PCD) is a condition in which motile cilia do not function properly. PCD causes a range of symptoms, owing to the diverse role of motile cilia throughout organ systems. Prominent among these include pulmonary obstruction and infection resulting from impaired mucus clearance, male and female sub- or infertility, and heterotaxy (Waters & Beales, 2011; Newman et al., 2023). In this condition, placement of internal organs across the left-right axis is fully or partially reversed, as internal left-right asymmetry is established through a motile cilia- and fluid flow-based mechanism during embryogenesis (Nonaka et al., 1998; Grimes & Burdine, 2017; Grimes, 2019b). This occurs in a temporary organ called the node in mammals and Kuppfer's Vesicle (KV) in zebrafish (Nonaka et al., 1998; McGrath et al., 2003; Essner et al., 2005; Kramer-Zucker et al., 2005). Loss of cilia-generated flow or flow sensory mechanisms causes randomization of internal laterality (McGrath et al., 2003; Essner et al., 2005; Grimes & Burdine, 2017). In human development, this often has the knock-on effect of congenital heart defects (Jin et al., 2017) due to the influence of left-right asymmetry on cardiac morphogenesis (Kathiriya & Srivastava, 2000).

While zebrafish are often used to study left-right patterning and heart looping (Essner et al., 2005; Kramer-Zucker et al., 2005; Gourronc et al., 2007; Jaffe et al., 2016; Grimes & Burdine, 2017), zebrafish with defective cilia motility were first identified by a different, more immediately obvious phenotype (Haffter et al., 1996; Brand et al., 1996, Sullivan-Brown et al., 2007) referred to as curly tail down (CTD). During the latter part of the first day post fertilization, the zebrafish body axis elongates and uncurls from around the yolk (Figure 1.1), eventually forming a straight body axis (Grimes, 2019a). In cilia motility mutants, this process fails and embryos develop a ventrally curved body axis, CTD (Figure 1.2B). Usually, this

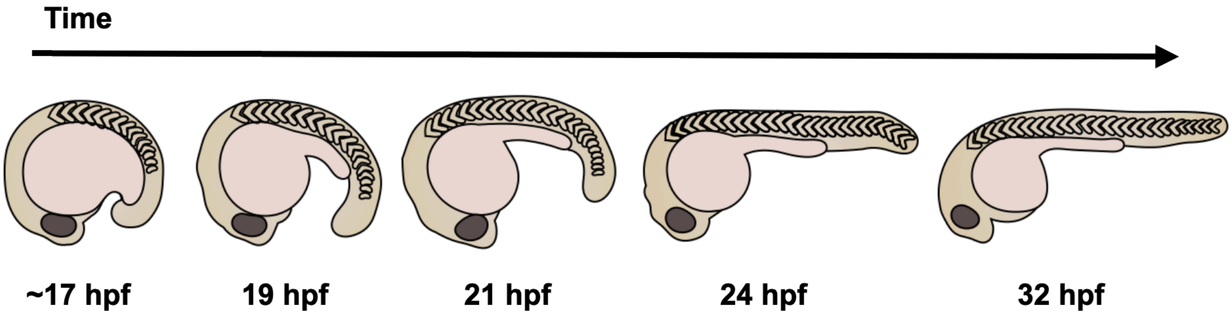

Figure 1.1. Zebrafish embryos gradually uncurl from the yolk during the first 32 hpf. In early development, zebrafish embryos begin curled around the yolk. As they grow during the first day post fertilization, their body axis gradually uncurls and becomes straight.

condition is lethal as embryos are unable to eat during larval stages and typically arrest around 7-10 days post fertilization (dpf). Indeed, the discovery of the adolescent growth role for motile cilia in spinal morphogenesis was only discovered by rescuing the early CTD phenotype using mRNA injection approaches and a temperature-sensitive mutant (Grimes et al., 2016). The fact that motile cilia (as well as other factors) control initial axial straightening during embryogenesis and long-term maintenance of the shape of the body and spine hinting at a connection between pathways that generate and then maintain the body axis. As such, initial axial straightening could serve as a tractable surrogate system for understanding, at least in part, pathways operating later in life to maintain the spine.

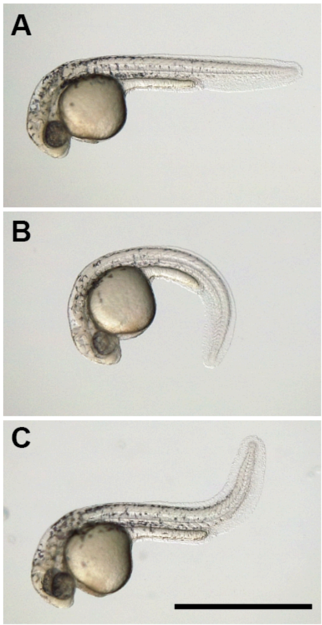

Figure 1.2. Two types of axial defects in zebrafish embryos. (A) A wild type zebrafish larva at 28 hpf. (B) A zebrafish larva at 28 hpf with curly tail down (CTU). (C) A zebrafish larva at 28 hpf with curly tail up (CTU). Scale bar: 1mm

In Chapter II, I discovered novel mechanisms of action of the cilia-associated protein Daw1. Daw1 had previously been studied in the single-celled alga *Chlamydomonas* (Ahmed & Mitchell, 2005; Ahmed et al., 2008) and in zebrafish injected with morpholinos (Gao et al., 2010), where it was shown to control cilia motility by assisting in the import of dynein motor complexes. However, its roles in embryonic and juvenile development had never been studied. In collaboration with Dr. Elizabeth Bearce, I discovered that Daw1 is required for timely onset of cilia motility, causing full penetrance of PCD phenotypes early in development (laterality defects and CTD), while only weak penetrance of scoliosis in juvenile stages and adulthood (Bearce, Irons, Craig, et al., 2022). Additionally, I used the temperature-sensitive allele $cfap298^{tm304}$, which can be used to stop and start cilia motilty by shifting incubation temperatures, to show that the body axis is able to "recover" from CTD if cilia motility is restored as late as 3 days post fertilization. This recovery took longer and is sometimes less complete than when cilia motility is restored earlier (Bearce, Irons, Craig, et al., 2022). This demonstrated that the zebrafish body axis displays plasticity and can remodel, a kind of "shape regeneration". The results of our study on *daw1* in zebrafish were complemented by work we performed in collaboration with Dr. Emma Baple's group at the University of Exeter Medical School. They identified patients with sequence variants in *DAW1* that exhibited heterotaxy, a sign of cilia motility dysfunction during early development. However, patients exhibited only mild respiratory defects and no infertility, calling into question whether symptoms were indeed caused by cilia dysfunction (Leslie et al., 2022). We modeled the human variants in zebrafish, showing that they do disrupt Daw1 function. Moreover, our findings in zebrafish also explained the unusal form of PCD in this patient cohort, because, as in zebrafish, patients exhibited disruptions to developmental events (left-right patterning) but not later homeostatic processes (airway clearance).

In chapter III, I investigate two factors that may function downstream of cilia motility and flow signals during axial morphogenesis: the Reissner fiber, a thin proteinaceous fiber running through the central canal (Cantaut-Belarif et al., 2018), and the urotensin-related peptides Urp1 and Urp2, small cyclic peptides expressed in flow-sensory neurons in the central canal (Zhang et al., 2018). The Reissner fiber is mostly comprised of the protein SCOspondin that runs down the length of the central canal of most vertebrates. It is known to assemble downstream of cilia motility and is required for axial straightening (Cantaut-Belarif et al., 2018). Recently, Troutwine et. al. endogenously tagged SCOspondin with GFP, allowing fiber assembly to be observed *in vivo* (Troutwine et al., 2020). In collaboration with Dr. Bearce, I combined this allele with *daw1*^{b1403} to show delayed assembly of the fiber in response to delayed onset of cilia motility. I also generated zebrafish lacking both urotensin-related peptides (Urp1 and Urp2), revealing that they are in fact dispensable for axial straightening, but instead are required for long-term maintenance of spinal straightness during juvenile growth, as adults lacking Urp1 and Urp2 developed severe spinal curves.

Lastly, in Chapter IV, to determine how axial straightening morphogenesis ceases once the linear axis is formed, I investigated mutants displaying the “opposite” phenotype to CTD, curly tail up, or CTU (Figure 1.2C). These mutants contained mutations in the zebrafish ortholog of the gene *PKD2*, one of two genes (the other being *PKD1*) previously identified as responsible for causing autosomal dominant polycystic kidney disease in humans (Boucher & Sandford, 2004). Zebrafish mutant for *pkd2* develop left-right patterning defects, as Pkd2 is known to act as a flow sensor downstream of cilia motility in KV in complex with Pkd1l1 (Field et al., 2011). I hypothesized that Pkd2 could similarly be acting downstream of fluid flow in the central canal, this time in complex with Pkd1 and Pkd1b. I generated zebrafish doubly mutant for *pkd1* and *pkd1b* showing that embryos developed CTU like *pkd2* mutants. This supports a model in which Pkd2 functions with Pkd1/Pkd1b to control axial morphogenesis. However, epistasis tests combing *pkd2*^{b1402} mutants with the cilia motility mutant *cfap298*^{tm304}*,* Reissner fiber mutant *sspo*^{b1446}, and *urp1*$^{\Delta P}$;*urp2*$^{\Delta P}$ mutants showed that *pkd2* is likely to act in a cilia-independent pathway to prevent axis over-straightening. In a final series of experiments, I developed tools which will allow for a future assessment of the requirement of Pkd2 function in the notochord, another tissue involved in axial straightening.

Taken together, my results provide new insights into the cilia-depedent and cilia-independent mechanisms that collaborate to straighten the body axis in zebrafish. The cilia-dependent pathway provides instructions for axial straightening, which is then countered by a cilia-independent mechanism involving the polycystin proteins Pkd2, Pkd1, and Pkd1b (Figure 1.3), possibly functioning in the notochord.

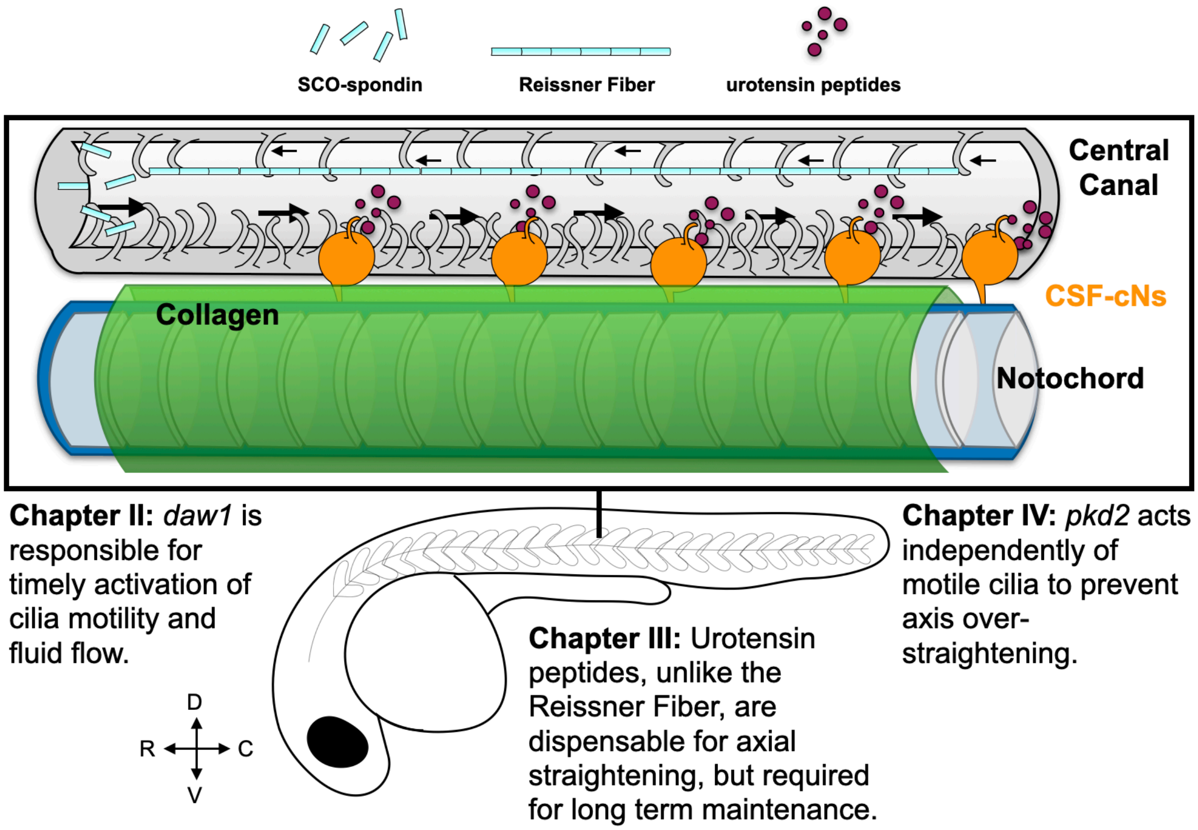
SCO-spondin
Reissner Fiber
urotensin peptides
Central Canal
CSF-cNs
Collagen
Notochord
D
R
C
V

Chapter II: *daw1* is responsible for timely activation of cilia motility and fluid flow.

Chapter III: Urotensin peptides, unlike the Reissner Fiber, are dispensable for axial straightening, but required for long term maintenance.

Chapter IV: *pkd2* acts independently of motile cilia to prevent axis over-straightening.

Figure 1.3. Model of axial straightening. My work spans multiple tissues to investigate the mechanisms of axial straightening in zebrafish. Motile cilia in the central canal generate cerebrospinal fluid (CSF) flow, which leads to Urotensin peptide expression, Reissner fiber formation and the gradual uncurling of the body axis from the yolk. Simultaneously, Pkd2 acts in a cilia-independent mechanism to prevent axis over-straightening.

CHAPTER II: DAW1 REGULATES THE TIMELY ONSET OF CILIA MOTILITY DURING DEVELOPMENT

Published in *Development* May 2022

Elizabeth A. Bearce[1,*], Zoe H. Irons[1,*], Samuel B. Craig[1], Colin J. Kuhns[1], Cynthia Sabazali[1], Dylan R. Farnsworth[2], Adam C. Miller[2] and Daniel T. Grimes[1,‡]

*These authors contributed equally to this work

[1]Institute of Molecular Biology, Department of Biology, University of Oregon, Eugene, OR 97403, USA.
[2]Institute of Neuroscience, Department of Biology, University of Oregon, Eugene, OR 97403, USA.

‡Correspondence (dtgrimes@uoregon.edu)

Introduction

Motile cilia are microtubule-based organelles that protrude from the cell membrane and beat to drive cell propulsion and generate extracellular fluid flows. They are involved in several developmental and homeostatic processes (Spassky & Meunier, 2017) including airway clearance, left-right (L-R) organ asymmetry and fertility (Wallmeier et al., 2020). Zebrafish, *Danio rerio*, is a powerful model for elucidating roles of motile cilia in development and disease (Austin-Tse et al., 2013; Becker-Heck et al., 2011; Kramer-Zucker et al., 2005). Zebrafish mutants with perturbed motile cilia exhibit aberrant L-R patterning as a result of impaired fluid flow within the L-R organizer, Kupffer's Vesicle (KV) (Kramer-Zucker et al., 2005; Essner et al., 2005).

Normally, leftward fluid flow within the KV results in the repression of *dand5* on the left side of KV, leading to the asymmetric activation of *nodal* in the left lateral plate mesoderm (LPM), therefore allowing for establishment of the Nodal pathway in the left, but not right, LPM (Grimes & Burdine, 2017). Nodal signaling in the left LPM signals to the developing heart cone, instructing cells to migrate to the left (Baker et al., 2008; Smith et. al., 2008), establishing the leftward position of the heart. This process, called jogging, is followed by cardiac looping, in which the heart tube bends rightward to produce a dextral S-shaped heart with the ventricle on the right side of the atrium (Desgrange et al., 2018; Grant et al., 2017). This process is analogous to heart looping in human heart development (Grant et al., 2017). Defects in the activity or sidedness of the LPM Nodal pathway result in abnormally lateralized heart jogs and loops (Grimes, 2019b).

In humans, disorders arising from defective cilia motility (termed motile ciliopathies) are characterized by a range of clinical features. One of the first of these noted was *situs inversus*, in which the laterality of the internal organs is reversed (Waters & Beales, 2011). While occasionally benign, this often has the added effect of causing congenital heart defects, as the previously described process of heart looping is sensitive to disruptions in Nodal signaling (Jin et al., 2017; Peeters & Devriendt, 2006). The most common motile ciliopathy is primary ciliary dyskinesia (PCD). In addition to laterality defects, PCD patients present with recurrent ear and lower respiratory infections, caused by a failure of mucus clearance in the lungs and ear canals. Both genetically male and female patients also commonly experience infertility or sub-fertility caused by defects in sperm flagella motility and impaired cilia motility within the fallopian tubes and along endometrium (Leigh et al, 2009; Newman et al, 2023). The genetic cause of PCD is often a homozygous mutation in one or more genes involved in cilia assembly, structure, or function (Leigh et al, 2009; Waters & Beales, 2011).

In zebrafish, motile cilia are responsible for generating flow of cerebrospinal fluid (CSF) in the central canal (Kramer-Zucker et al., 2005; Olstad et al., 2019; Thouvenin et al., 2020). In the absence of CSF flow, zebrafish are unable to straighten the body axis over the first day of development, causing ventral axis curves referred to as 'curly tail down' (CTD) (Kramer-Zucker et al., 2005). Transiently restoring cilia motility to rescue CTD showed that motility is also required for the maintenance of spinal straightness during juvenile growth, with late disruption of motility causing three-dimensional spinal curves (Grimes et al., 2016). These phenotypes mimicked the prevalent human spine disorder idiopathic scoliosis (IS) in which curves manifest during adolescent growth (Bearce & Grimes, 2021; Boswell & Ciruna, 2017; Chen et al., 2016; Grimes et al., 2016).

These examples attest that motile cilia play diverse roles during development, growth and homeostasis, across varied time scales. During L-R patterning, ~50-200 motile cilia act rapidly, over a few hours (Little & Norris, 2021). Otolith, or "ear stone", formation in zebrafish, is similarly closely tied to the first day of development, during which motile cilia on opposite poles of the otic vesicle create fluid vortices that attract otolith precursor particles to form two stones of approximately equal size (Colantino et al., 2009; Stooke-Vaughan et al., 2012). In other contexts, such as airway clearance, hundreds of thousands of cilia function throughout life, with a gradual turnover of ciliated cells. As such, the requirements for timely initiation of motility after cilia emerge from cells is likely to be context-dependent. Yet, little is known about the regulation of when cilia begin to beat as (or after) they form. In *Chlamydomonas reinhardtii*, a unicellular algae, cilia achieve periodic beating when 4 μm long, approximately one third of their final length (Bottier et al., 2019). In the zebrafish KV (Essner et al., 2005; Kramer-Zucker et al., 2005), the majority of cilia are immotile at the three-somite stage but become motile by the eight-somite stage, 2.5 hours later (Tavares et al., 2017). Similarly, airway cilia waveforms change as specific dynein arm motors are localized to the axoneme during cilia growth (Oltean et al., 2018). Discovering factors which regulate when cilia begin to beat robustly and determining their importance in cilia-dependent processes would lend support to a hypothesis that 'beat onset' is itself a regulatory step, beyond being some final consequence of cilia assembly.

Motile cilia consist of an axoneme of an outer ring of nine microtubule doublets and, usually, a central pair of microtubules (Ishikawa et al., 2021). Cilia form from basal bodies, modified centrioles, which have docked with the apical plasma membrane (Kumar & Reiter, 2021). They are built and maintained by intraflagellar transport (IFT), in which motors transport cargo along the axoneme (Kozminski et al., 1993; Lechtreck, 2015). Motility is generated by outer and inner dynein arms, which power cilia beat frequency and waveform, respectively (King, 2016; Oda et al., 2014). Outer dynein arms (ODAs) are assembled in the cytoplasm then imported into the cilium (Fowkes & Mitchell, 1998; Lechtreck, 2015; Omran et al., 2008). Import depends on ODA16, which physically bridges ODAs and the IFT-B complex protein IFT46 (Dai et al., 2018; Hou & Witman, 2017; Taschner et al., 2017). In *Chlamydomonas*, loss of ODA16 causes decreased axonemal localization of ODAs and defective motility (Ahmed & Mitchell, 2005; Ahmed et al., 2008). This function is conserved, with motile cilia-associated phenotypes being found in zebrafish, mice and planarian flatworms upon perturbation of ODA16 homologs (Gao et al., 2010; Lesko & Rouhana, 2020; Solomon et al., 2017). Some species-specific differences in ODA16 homolog structures also imply possible differences in the mechanics of ODA16 action (Wang et al., 2020). Moreover, ODA16 is not absolutely required for motility in some contexts; for example, in *Chlamydomonas*, ODA16 is not essential for ODA import, but instead enhances the efficiency of import (Ahmed and Mitchell, 2005; Ahmed et al., 2008).

While exploring the zebrafish ODA16 homolog, Daw1, we found that Daw1 controls the timely onset of cilia beating during development. Embryonic phenotypes were fully penetrant in *daw1* mutants but later phenotypes, including spinal curves, only occurred in a subset of mutants. Daw1-deficient zebrafish showed reduced cilia motility during the first day of development but, over the following days, motility increased to wild-type levels. Daw1 therefore ensures that timely and robust motility is achieved during development. The motility delay caused CTD during early stages which, remarkably, later self-corrected. Thus, zebrafish larvae can adapt to anatomical aberrations and re-organize to generate the 'target morphology' of a linear body. Overall, this demonstrates that Daw1 is a regulator of the timing of onset of cilia motility and establishes the requirements of this function in development.

Additionally, in collaboration with Emma Baple and Andrew Crosby (University of Sheffield), we were able to examine the consequences of impaired DAW1 function in a human disease context. In a cohort of patients homozygous for mutations in *DAW1*, the Baple/Crosby lab had identified the presence of *situs inversus*, a characteristic symptom of PCD, without a number of symptoms that often accompany it such as sub-fertility and chronic lower respiratory infections (Leslie et al., 2022). This unique combination prompted us to investigate the role of DAW1 in human development, and model the alleles seen in patients using zebrafish. We found that human *DAW1* variants were indeed non-functional, providing critical evidence that *DAW1* mutations cause a motile ciliopathy mostly characterized by L-R defects. Our model that Daw1 controls the timely onset of beating, and so is more important in cell types that form cilia and function on rapid timescales, like the LRO, and less essential where cilia function in great numbers with gradual tissue turnover, like the airways, can explain this unusual ciliopathy.

Results

***daw1^{b1403}* mutants exhibit phenotypes of cilia motility mutants at early stages, but not later stages.**

We generated a *daw1* mutant line harboring a deletion of two amino acids located centrally in a β-propeller structure (Figure 2.1A,B; Figure 2.2). This should disrupt Daw1 function as the β-propeller interacts with ODAs (Taschner et al., 2017). *daw1^{b1403}* homozygous adults were viable and fertile; most showed no obvious phenotypes. However, ~20% exhibited spinal curves in dorsal-ventral and medio-lateral directions (Figure 2.1C-E′; Figure 2.3A-C). Curves occurred in the absence of abnormalities in vertebra shape or patterning, suggesting that they were not caused by structural vertebral defects (Figure 2.3; Movie 1). Coupled with the 3D nature of the curves this suggested that phenotypic *daw1^{b1403}* mutants exhibited characteristics of IS.

Although other cilia motility mutants are known to develop IS-like spinal curves (Grimes et al., 2016), *daw1^{b1403}* mutants were unusual in that the penetrance of curves was low. We hypothesized this could be due to cilia motility being only partially affected in *daw1*^{b1403} mutants. We first investigated this by determining the consequences of *daw1*^{b1403} mutation in contexts beyond the spine, given that *daw1* is expressed in numerous motile ciliated tissues in the embryo (Figure 2.4; Gao et al., 2010). *daw1*^{b1403} mutants had high levels of L-R patterning defects and otolith placement abnormalities (Figure 2.1F,G). two processes partly controlled by motile cilia (Colantonio et al., 2009; Grimes & Burdine, 2017). In addition, 100% of *daw1*^{b1403} mutants exhibited CTD at 25 hours post fertilization (hpf) (Figure 2.1H), as also found in Daw1 morphants (Gao et al., 2010). Abnormal cilia motility-associated phenotypes were therefore fully penetrant in *daw1*^{b1403} mutants during early development.

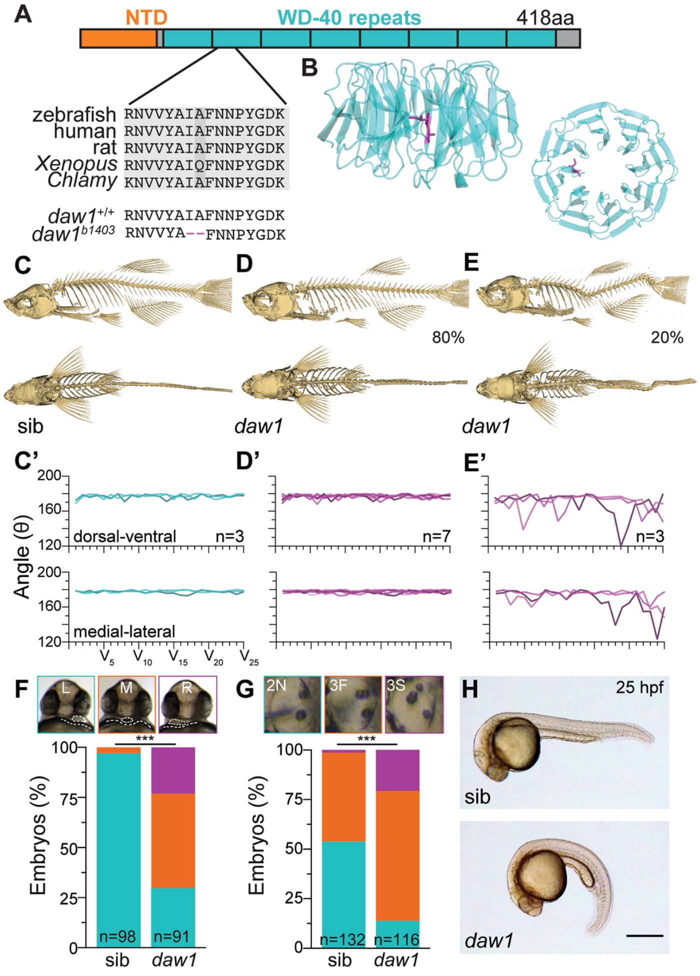

Figure 2.1. *daw1^{b1403}* mutants exhibit motile cilia-associated defects. (A) The 418 amino acid Daw1 protein with short N- terminal domain (NTD) and large β-propeller composed of WD40 repeats. *daw1^{b1403}* deletes two conserved residues, I140 and A141. (B) Human DAW1 X-ray structure (Protein Data Bank: 5NNZ) showing I140 and A141 location. (C-E) 3D reconstitutions of µCT data. Most *daw1^{b1403}* mutants showed normal spines (D), but 20% exhibited curves (E), compared with control (C). (C′-E′) Quantitation of curvature showed curved *daw1^{b1403}* mutants had a non-stereotyped pattern (E′), compared with control (C′) and non- curved *daw1^{b1403}* mutants. (F) Top: representative image of 25 hpf larvae showing the heart (dotted oval) on top of the yolk (dotted line). Bottom: *daw1^{b1403}* mutants exhibited randomized heart laterality including left (L; green), middle (M; orange) and right (R; magenta)-facing hearts (n=91 mutants and 98 sib controls; ***P=4.84×10^{-21}, chi square). (G) Top: otic vesicles at 25 hpf showed abnormal phenotypes in *daw1^{b1403}* mutants [2N (green) – two normal; 3F (orange) – three otoliths, posterior two fused; 3S (magenta) – three separate otoliths. Bottom: quantification of n=116 mutants and 132 sibs; ***P=1.31×10^{-12}, chi square. (H) CTD in *daw1^{b1403}* mutants was fully penetrant at 25 hpf. Scale bar: 0.5 mm (H).

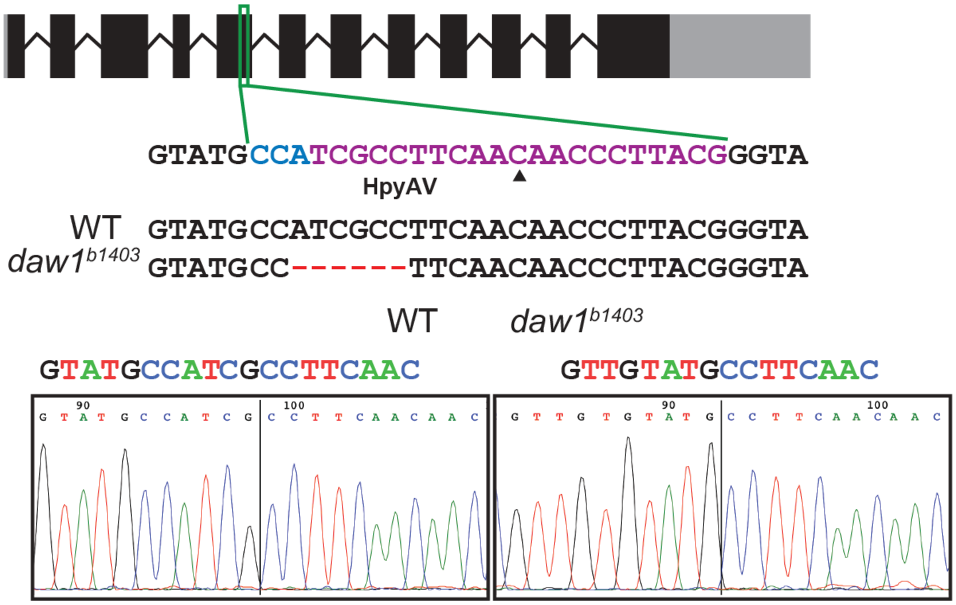
GTATGCCATCGCCTTCAACAACCCTTACGGGTA
HpyAV
WT
daw1b1403
GTATGCCATCGCCTTCAACAACCCTTACGGGTA
GTATGCC------TTCAACAACCCTTACGGGTA
WT
daw1b1403
GTATGCCATCGCCTTCAAC
GTTGTATGCCTTCAAC
90
100
G T A T G C C A T C G C C T T C A A C A A C
90
100
G T T G T G T A T G C C T T C A A C A A C

Figure 2.2. Schematic of the *daw1^{b1403}* mutation. The *daw1* locus is composed of 12 exons. An sgRNA target sequence (purple) with PAM (blue) disrupted exon 5. The presence of insertion-deletion mutations was initially screened in G0 embryos by protection from restriction enzyme digestion with HpyAV. The *daw1^{b1403}* allele that was isolated encodes a 6-base pair deletion, as shown in the Sanger sequencing traces.

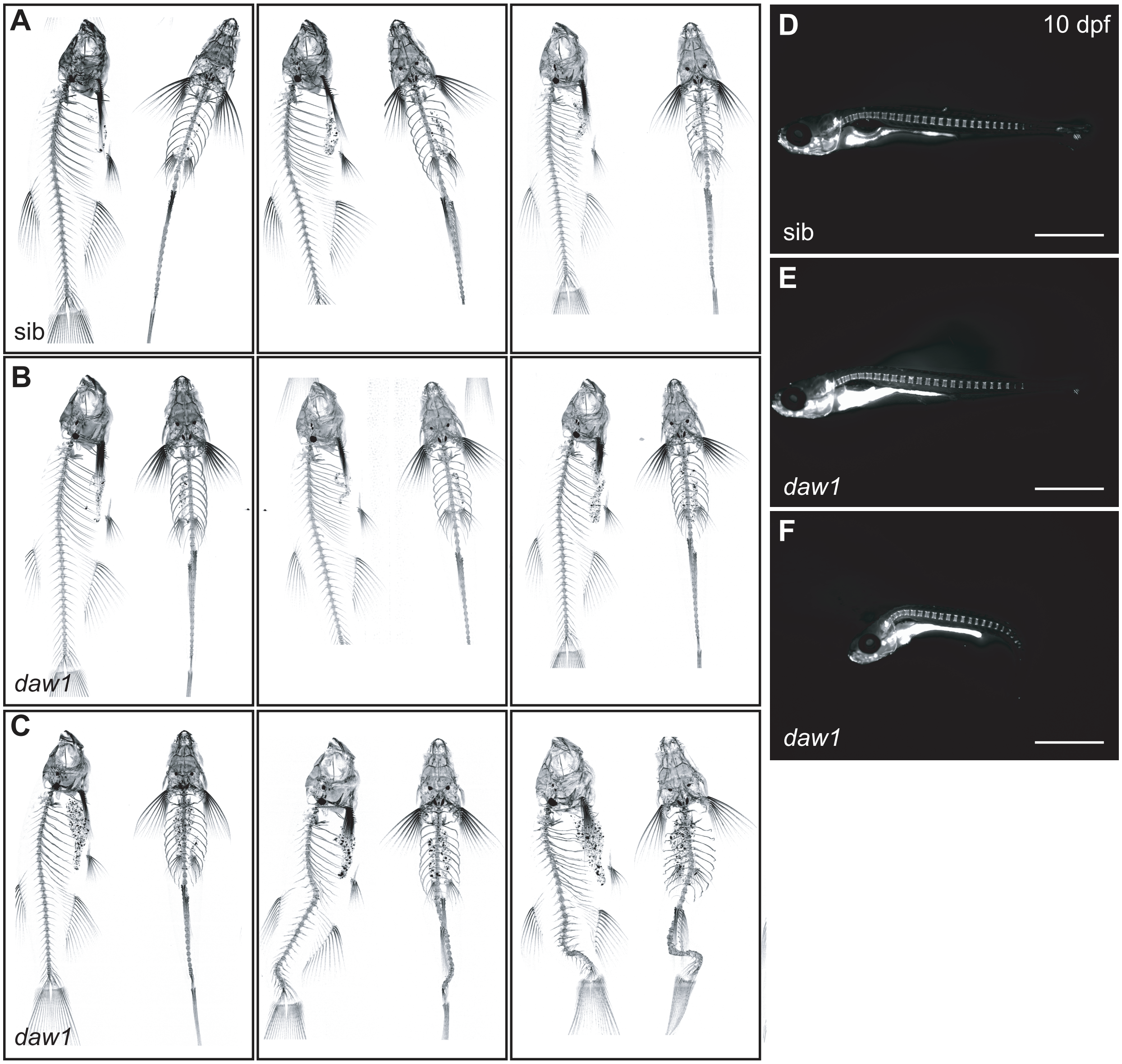

Figure 2.3. µCT and calcein staining of *daw1^{b1403}* mutants and sibling controls. (A-C) µCT data visualized as maximum intensity projections from nine fish: *daw1^{b1403}* heterozygotes (A); *daw1^{b1403}* homozygotes that were straight at 5 d.p.f. (B); and *daw1^{b1403}* homozygotes that retained axial kinks at 5 d.p.f. (C). Spinal curves were present only in a subset of fish within the latter category (C). (D-F) Epifluorescent stereoscope images of calcein-stained 10 d.p.f. *daw1^{b1403}* heterozygotes (D), and straight (E) or kinked (F) *daw1^{b1403}* homozygotes following incubation with calcein vital dye. Scale bars: D-F; 1 mm.

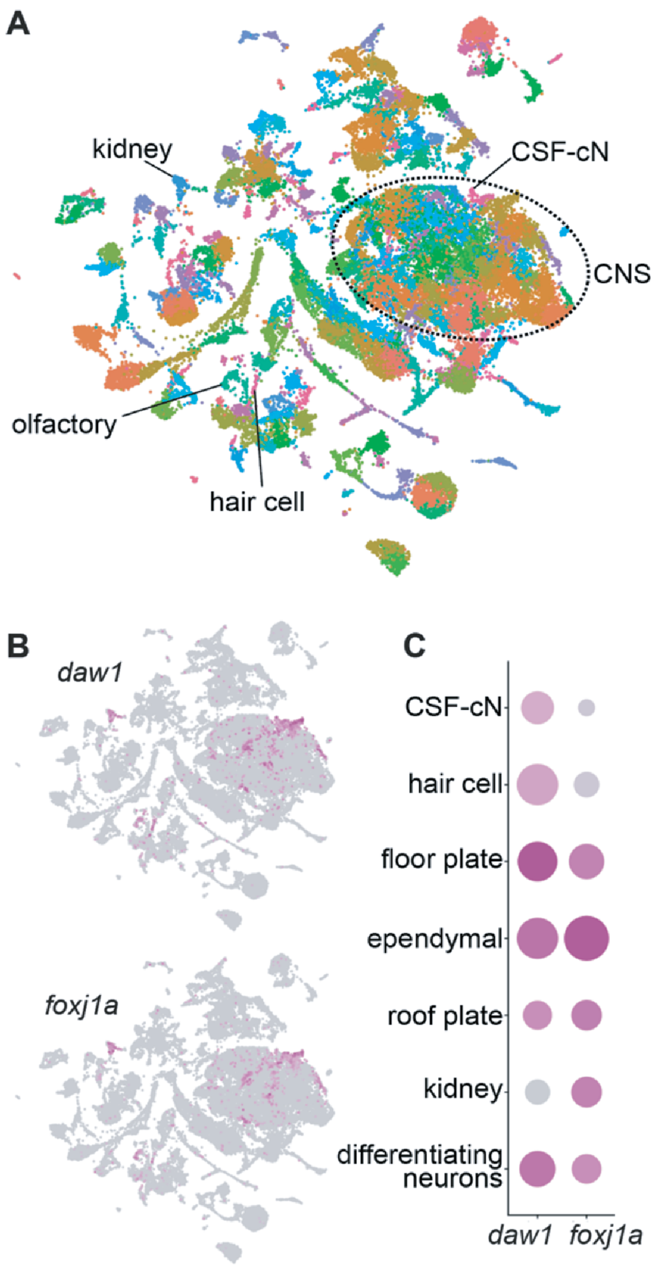

Figure 2.4. Expression of *daw1* across 1-5 d.p.f. zebrafish larvae from a single-cell RNA sequencing atlas. (A) UMAP plot visualizing whole-zebrafish single cell RNA sequencing data from 1-5 d.p.f. larvae. Some clusters corresponding to cell types harboring motile cilia are highlighted. (B-C) UMAP (B) and dot (C) plots of *daw1* and *foxj1a* expression, showing that both expression profiles closely overlap. Foxj1a is a master regulator of motile ciliogenesis and robust marker of motile-ciliated cell types. In (C), the size of the dot indicates the number of cells expressing the gene of interest in the cluster and the intensity of purple correlates with the average number of reads within cells in the cluster. Cell types were interpreted based on expression of 16 highly expressed marker genes (Farnsworth et al., 2020). CNS – central nervous system, CSF-cN –cerebrospinal fluid-contacting neuron.

To investigate why only 20% of *daw1*^{b1403} mutants developed adult spinal curves, we followed mutants through development and growth. Mutants initially exhibited CTD, but most recovered to generate a linear axis by 3-5 days post fertilization (dpf) (Figure 2.5A-E′), as shown by quantitation of body angle, θ. Although significantly different at 1 dpf, by 5 dpf, θ for mutants and controls was similar (177.8±12.1° for *daw1*^{b1403} and 190.4±0.8° for controls, mean±s.d.; Figure 2.5E′). Thus, the consequences of *daw1* mutation on body axis development are temporary, with mutants being able to self-correct early curves.

Although most recovered, some *daw1*^{b1403} mutants retained axial kinks (Figure 2.5E′; Figure 2.6A-B). To determine whether these caused later IS-like phenotypes, we followed kinked and straight mutants to adulthood. Of mutants that had attained straightness by 5 dpf, 0/28 (0%) showed spinal curves as adults (Figure 2.1D,D′; Figure 2.3B) but 23/65 (35%) mutants that exhibited kinks at 5 dpf developed curves (Figure 2.1E,E′; Figure 2.3C). Thus, spinal curves arose in mutants that failed to fully recover from CTD. This could explain why *daw1*^{b1403} mutants exhibit a different, more variable, curve pattern compared with other cilia-associated IS genetic models in which spinal curves are caused by reduced cilia motility during juvenile growth (Grimes et al., 2016).

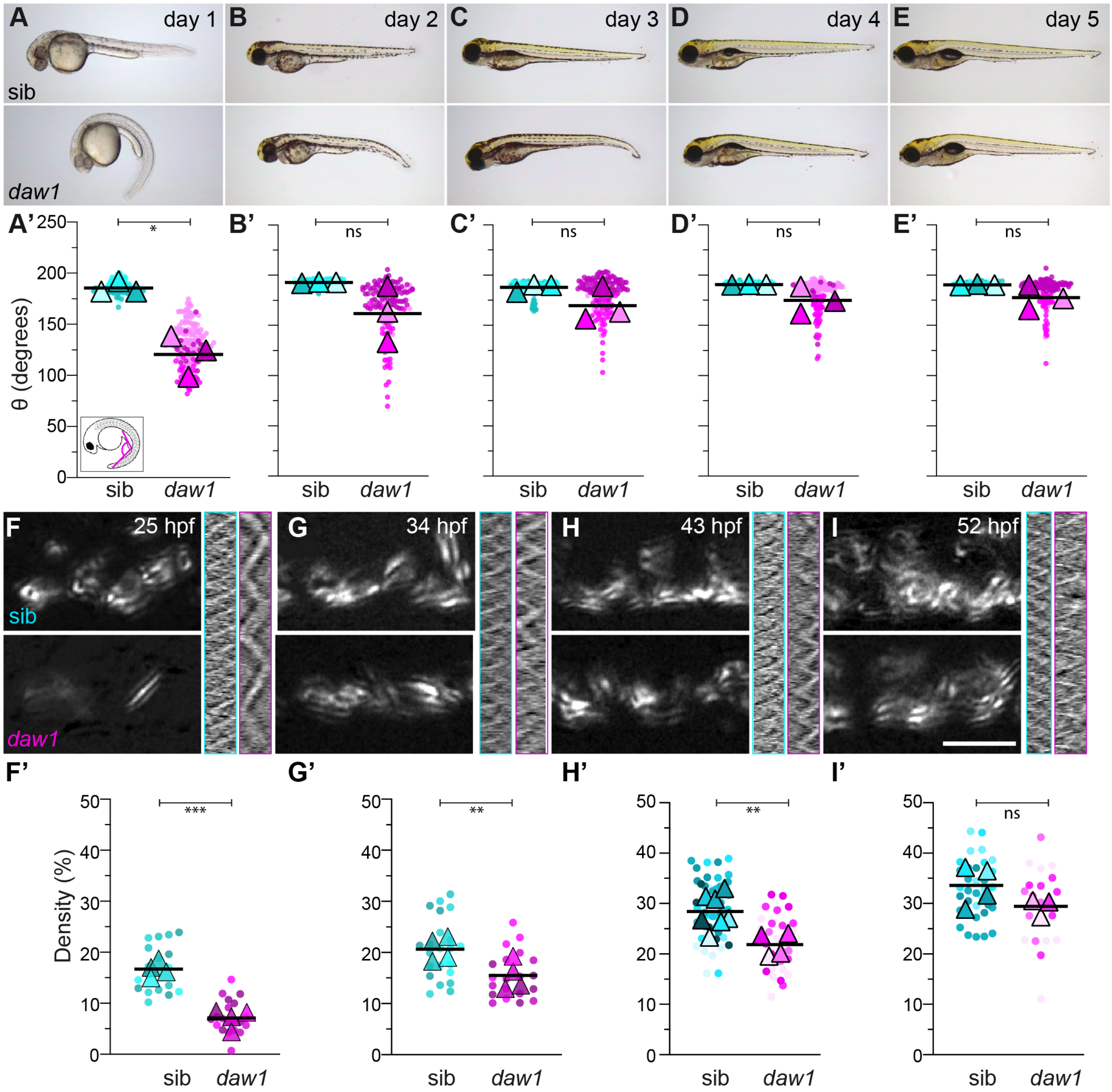

Figure 2.5. Body axis curvature self-corrects after delayed onset cilia motility. (A-E) The first 5 days of development show *daw1*^{b1403} mutants self-correct curves. (A′-E′) SuperPlots of body angle, θ (inset in A′). Pairwise comparisons used two-way ANOVA adjusted for multiple comparisons. (F-I) TICS of CC cilia motility at different time points. (F′-I′) SuperPlots of the proportion of the CC covered by cilia motility (motile area). ***P<0.001, **P<0.01, *P<0.05 (two-tailed unpaired t-tests). ns, not significant. Scale bars: 0.5 mm (A-E); 5 μm (F-I).

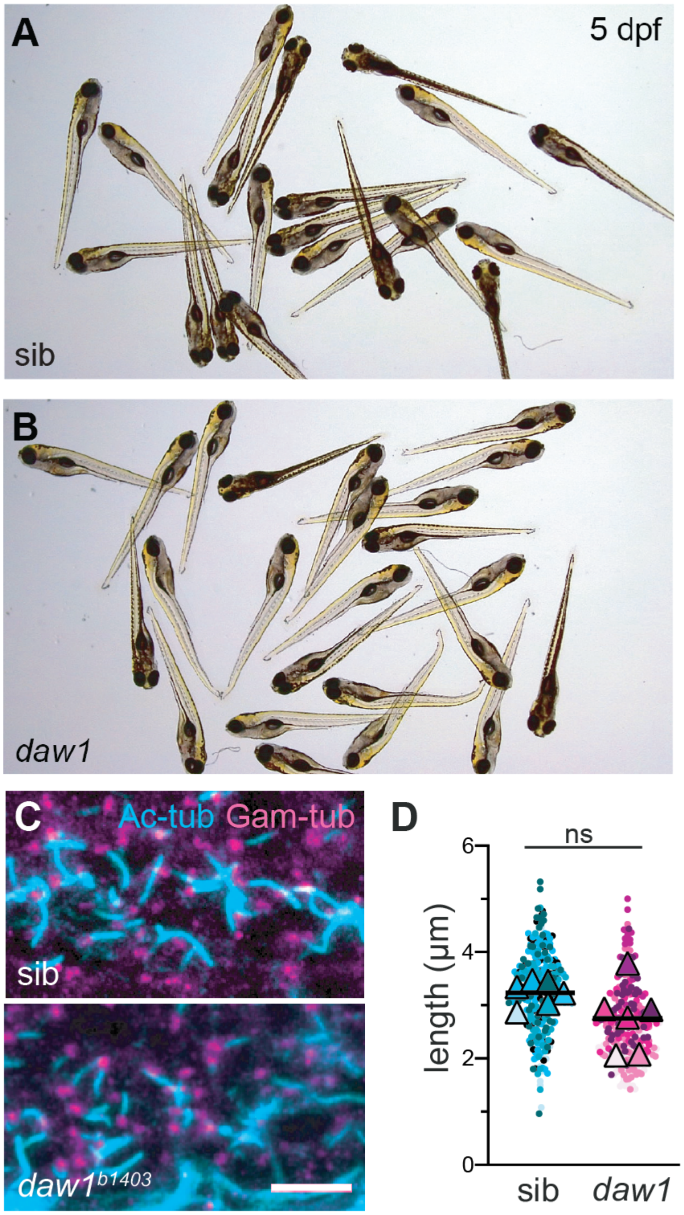

Figure 2.6. Axial phenotypes and central canal cilia in *daw1*^{b1403} mutants. (A-B) Group shots of *daw1*^{b1403} sibling (A) and *daw1*^{b1403} mutant (B) clutches at 5 d.p.f. While most mutants successfully straighten, a subset maintain mild axial kinks. (C) Acetylated alpha-tubulin (cilia) and gamma-tubulin (basal body) immunolabeling of *daw1*^{b1403} siblings and homozygous mutant fish at 28 h.p.f. (D) Cilia length quantification reveals no significant difference between controls and mutants (*t*-test applied). Dots represent individual cilia, triangles show averages of data from different individual embryos and black lines show means. Data are from 6 siblings and mutants with >50 cilia per field of view and 3-4 fields of view per individual. ns – not significant. Scale bar: A; 5 µm.

daw1*^{b1403} *mutants exhibit delayed onset of robust cilia motility in the central canal

To understand how *daw1*^{b1403} mutants self-corrected axial curves, we assessed motile cilia in the central canal (CC). Immunostaining showed normal length of CC cilia in mutants (Figure 2.6C-D), as expected (Gao et al., 2010). Although controls showed robust cilia beating (average frequency: 17.1±5.8 Hz) most cilia in *daw1*^{b1403} mutants were static (Figure 2.5F; Movie 2), something corroborated by quantitation of the area occupied by moving cilia, termed motile area (Figure 2.5F′). The few cilia in mutants that showed motility beat slowly (7.4±2.7 Hz) and erratically (Figure 2.5F; Figure 2.7). Thus, the motility of CC cilia was significantly reduced in *daw1*^{b1403} mutants at 25 hpf, explaining the fully penetrant CTD at this stage.

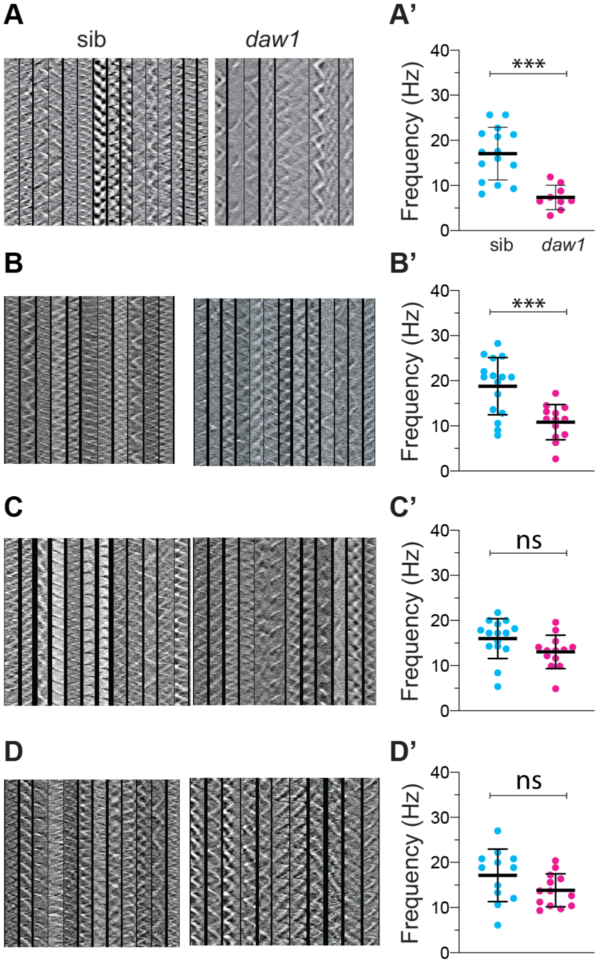

Figure 2.7. Cilia kymograph and frequency data from live imaging in the central canal. (A-D) Kymographs extracted from live imaging of either *daw1*^{b1403} sibling or homozygous mutant fish at 25 h.p.f. (A), 34 h.p.f. (B), 43 h.p.f. (C) and 52 h.p.f. (D). 1 pixel height corresponds to 1 frame (4 ms); total vertical height is equal to 1 second. (A'-D') Quantitation of cilia beat frequencies for the subset of cilia that display any movement (Hz), extracted from kymographs. Readings are from 3-5 cilia from at least 3 regions of interest. *** $P < 0.001$, ns – not significant.

We hypothesized that self-correction of CTD might occur if CC cilia motility increased over time. Quantitation of motility at 34, 43, and 52 hpf indeed showed such an increase (Figure 2.5G-I′; Figure 2.7; Movies 3-5). By 52 hpf, motility was no longer statistically different in *daw1*^{b1403} mutants compared with controls (Figure 2.5I′), showing that close to wild-type levels of motility were ultimately achieved, with a delay of ~1.5 days. Beyond the CC, motile cilia in the pronephric duct also displayed time-dependent phenotypes in *daw1*^{b1403} mutants. At 25 hpf, mutant cilia beat more slowly and were disorganized compared with controls (Movies 6,7). By 34 hpf, motility was similar to controls and cilia were correctly bundled (Movies 8,9). By contrast, we found no differences in sperm flagellum motility from samples extracted from *daw1*^{b1403} mutant males (Movies 10,11). This could be because short-term delays in motility onset are not evident in adult sperm cilia. Last, cilia in KV were immotile in *daw1*^{b1403} mutants (Movies 12,13), similar to what was previously shown in Daw1 morphants (Gao et al., 2010). This likely reflects that KV cilia are short-lived and have not had the necessary time to import ODAs in the absence of Daw1 function. Overall, this defines Daw1 as a factor which controls the timely onset of cilia motility on developmental timescales in zebrafish.

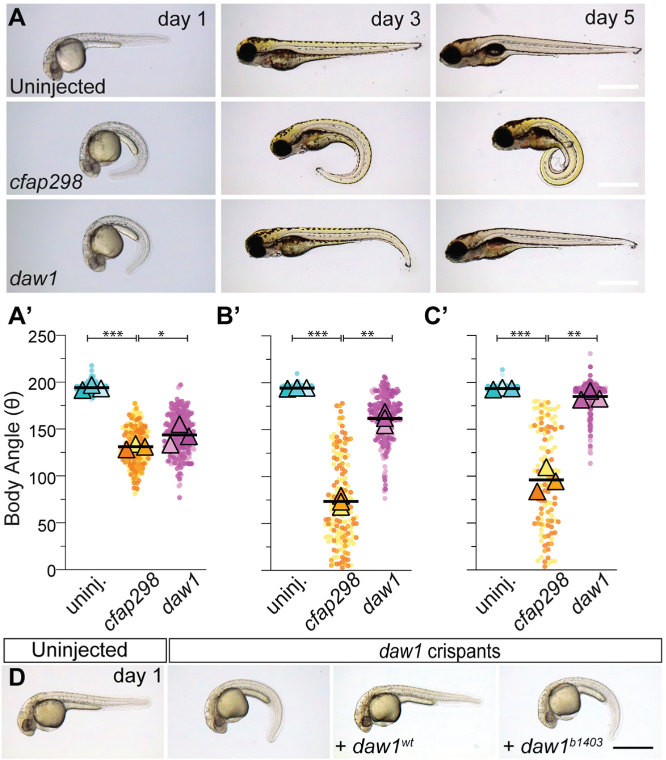

Figure 2.8. *daw1*^{b1403} encodes a loss-of-function protein. (A-C) Lateral views of controls and daw1 and cfap298 crispants. (A′-C′) SuperPlots of body angle quantitation. Pairwise comparisons used two-way ANOVA adjusted for multiple comparisons. ***$P<0.001$, **$P<0.01$, *$P<0.05$. ns, not significant. (D) Expression of Daw1^{WT} but not Daw1^{b1403} rescues the body curves of daw1 crispants. Scale bars: 0.5 mm (A-D).

This idea coheres with the model that Daw1/ODA16 enhances the efficiency of ODA import in *Chlamydomonas* (Ahmed and Mitchell, 2005; Ahmed et al., 2008). We suggest that inefficient ODA import in *daw1*^{b1403} mutants causes delayed onset of robust motility, explaining why motile cilia are more affected earlier in development (i.e. in KV as well as in the CC and pronephros at earlier time points) than later. This can also explain why early motile cilia-dependent processes, where cilia function is required over a short time period, such as L-R patterning and initial axial straightening, are severely impacted while later ones are not.

***daw1*^{b1403} mutants contain a loss-of-function allele.**

It is also possible that Daw1 is essential for the levels of ODA import needed for robust motility at all stages, as suggested by a previous morpholino knockdown study (Gao et al., 2010), but that the *daw1*^{b1403} line encodes a hypomorphic mutation that reduces but does not abolish Daw1 function. As *daw1*^{b1403} encodes a two amino acid deletion, it is conceivable that mutant protein retains some function. Both models could account for delayed motility in *daw1*^{b1403} mutants. To distinguish, we targeted *daw1* with multiple guide RNAs (gRNAs), generating crispant embryos with mosaic mutations. *daw1* crispants showed CTD at 1 dpf (Figure 2.8A,A′; Figure 2.9A,B) then self-corrected between days 2 and 5. The majority (91.2±6.1%) achieved a linear body axis by 5 dpf (Figure 2.8B-C′). Using the same approach to target *cfap298*, an ODA assembly factor required for motility (Austin-Tse et al., 2013; Jaffe et al., 2016), led to *cfap298* crispants which both developed and retained CTD (Figure 2.8A-C′). In addition, expression of mRNA coding for wild-type Daw1 rescued CTD in *daw1* crispants, demonstrating the specificity of the phenotype induced by *daw1* gRNAs (Figure 2.8D; Figure

2.9C). By contrast, expression of the Daw1^{b1403} variant did not rescue crispants, even partially (Figure 2.8D; Figure 2.9D). Last, we generated an additional mutant line, called *daw1^{b1422}*, in which a large deletion and premature truncation codon occur (Figure 2.10A-C). *daw1^{b1422}* mutants also exhibited CTD, which self-corrected over time (Fig. 2.10D-D′). Together, this suggests that *daw1^{b1403}* indeed represents a strong loss of function scenario. We therefore favor the model that, by enhancing the rate of ODA import, Daw1 controls the timely onset of robust cilia motility during development.

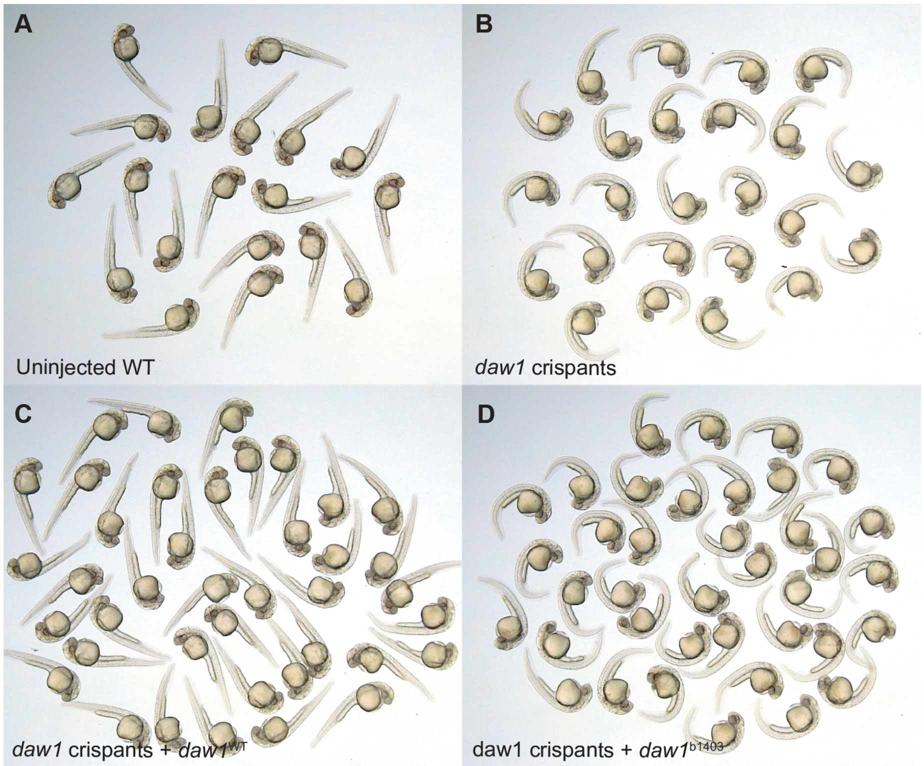

Figure 2.9. *daw1* crispants phenocopy mutants and are rescued by over-expression of wild-type, but not *daw1^{b1403}* mRNA. Lateral views of 28 h.p.f. fish. Uninjected, wild-type fish (A). Crispants generated by injection of 4 sgRNAs targeting *daw1* exhibited CTD (B). Crispants were rescued by co-injected of 20 pg of wild-type *daw1* mRNA (C) but not by *daw1^{b1403}* mRNA (D).

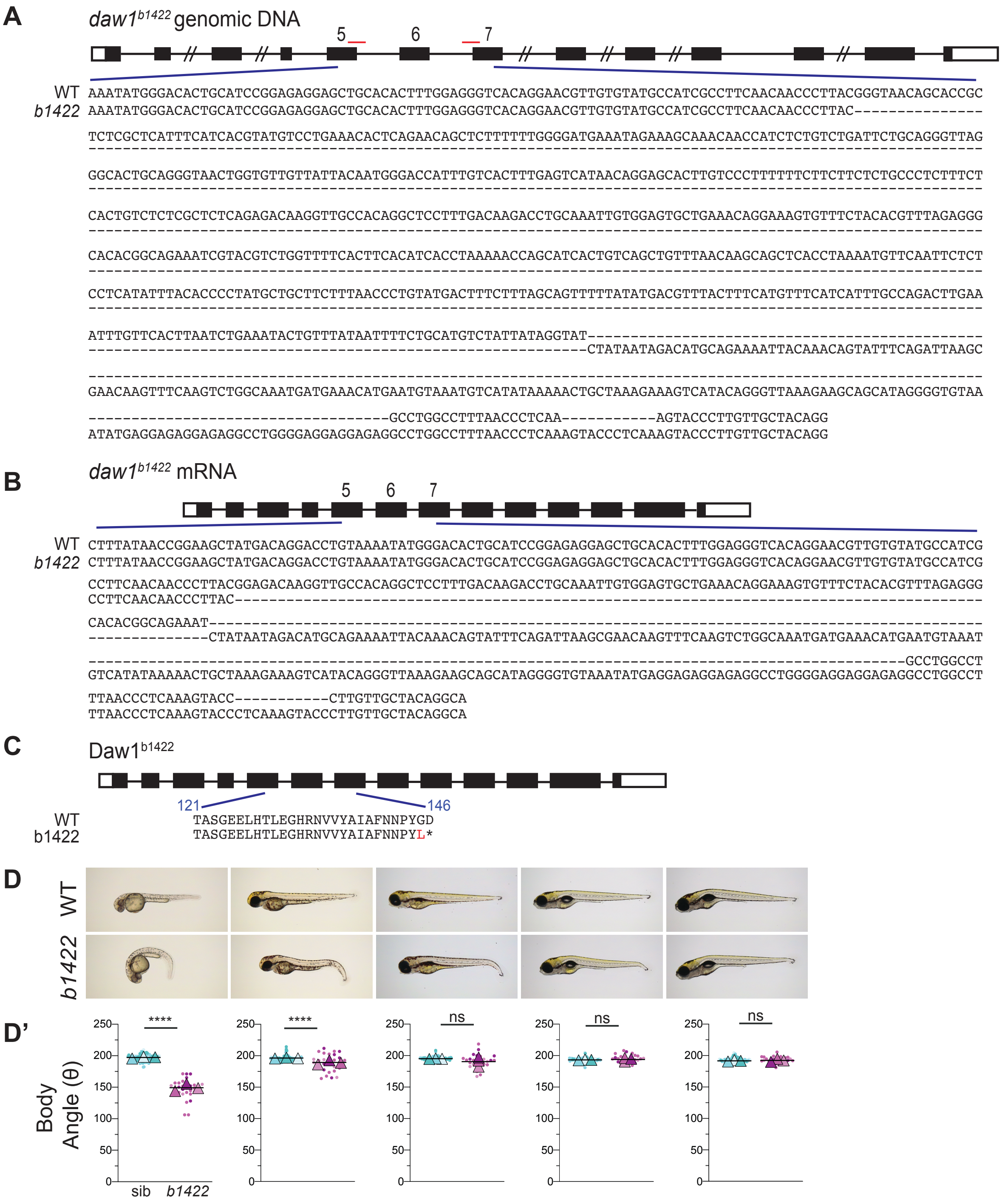

Figure 2.10. *daw1^{b1422}* mutants harbor a large deletion and premature truncation codon and phenocopy *daw1^{b1403}* mutants. (A-C) Two sgRNAs (red) targeted the *daw1* locus. Sequencing of both DNA (A) and cDNA prepared from a mutant mRNA library (B) revealed a large deletion/ inversion leading to a premature truncation of the protein prior to most functional domains (C). (D-D') Lateral views (D) and quantitation of body curvature (D') in *daw1^{b1422}* mutants. Pairwise comparisons used two-way ANOVA adjusted for multiple comparisons. ****$P < 0.0001$, ns – not significant.

Zebrafish embryos are able to recover from CTD upon return of cilia motility up to 3 days post fertilization.

The self-correction of CTD in *daw1* loss of function demonstrated the remarkable ability of zebrafish larvae to remodel their shape to achieve the species typical anatomy. To test whether this self-correction was caused by the late onset of cilia motility, we used a temperature-sensitive *cfap298*^{tm304} mutant line (Jaffe et al., 2016). At restrictive temperatures, *cfap298*^{tm304} mutants exhibited reduced CC cilia motility (Figure 2.11A; Movie 14) and ventral curves (Figure 2.12A,A′); at permissive temperatures, cilia were motile and embryos underwent straightening (Figure 12; Movie 14; Jaffe et al., 2016). We performed restrictive-to-permissive temperature shifts to initially inhibit cilia motility but then later activate it (Figure 2.11D). Downshifting at 24 hpf led to robust cilia beating by 52 hpf (Figure 2.11B,C; Movies 15,16); the majority of larvae corrected CTD (Figure 2.11B,C,E; Figure 13). By contrast, larvae maintained at restrictive temperatures showed no recovery of motility and retained CTD (Figure 2.11B,E; Movie 16). As a side note, a small proportion of mutants straightened at restrictive temperatures. This was partly dependent on whether or not mutants inherited wild-type *cfap298* gene product from their mothers (Figure 2.12B). Overall, in both *daw1*^{b1403} and downshifted *cfap298*^{tm304} mutants, larvae responded by remodeling their abnormal shape to achieve the wild-type anatomy despite missing the developmental window during which axial straightening normally occurs.

To determine whether the ability to self-correct CTD was maintained as larvae aged, we performed temperature shifts at progressive times (Figure 2.11D). Downshifting at 1 dpf resulted in axial straightening in 89.5 ± 18.3% of larvae by 24 h post-shift and 99.1 ± 1.6% by 48 h post-shift. Downshifting at 2 and 3 dpf led to progressively less efficient straightening (Figure 2.11D;

Fig. 2.13), though the majority of mutants (80.0 ± 17.8%) downshifted even at 3 dpf still attained axial straightness by 4 days post-shift. Downshifting at 4 and 5 dpf led to inefficient straightening, with larvae largely being unable to attain a linear axis by the termination of the experiment at 7 dpf (Figure 2.11D; Figure 2.13).

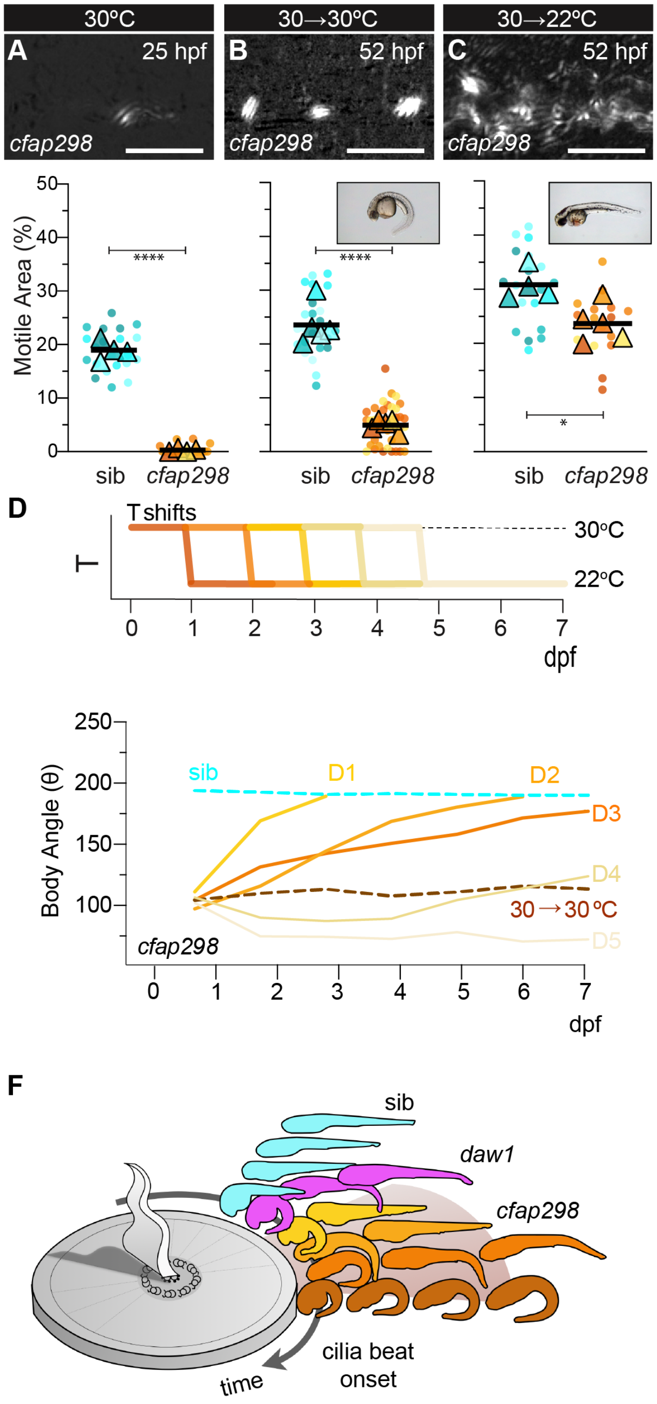

Figure 2.11. Self-correction of curves can occur throughout developmental stages. (A-C) Top: TICS of CC cilia motility of 25 hpf *cfap298^{tm304}* mutants raised at 30°C (A), then 52 hpf after maintaining 30°C (B) or downshifting to 22°C at 24 hpf (C). Bottom: SuperPlots of motility data. Insets: axis straightening occurred in downshifted embryos but not those maintained at 30°C. (D) Schematic of temperature (T) shifts. Embryos were raised at 30°C until either 1, 2, 3, 4 or 5 dpf, then downshifted to 22°C, inducing cilia motility. Body angles were assessed until 7 dpf. (E) Body angles across 1-7 dpf after temperature downshifts on days 1-5 (D1-D5). (F) Summary showing zebrafish larvae self-correct curves after robust CC cilia motility onsets. Distance around the sundial represents later times of motility onset in distinct conditions. ****$P<0.0001$, *$P<0.05$ (two-tailed unpaired t-tests). Scale bars: 5 µm (A-C).

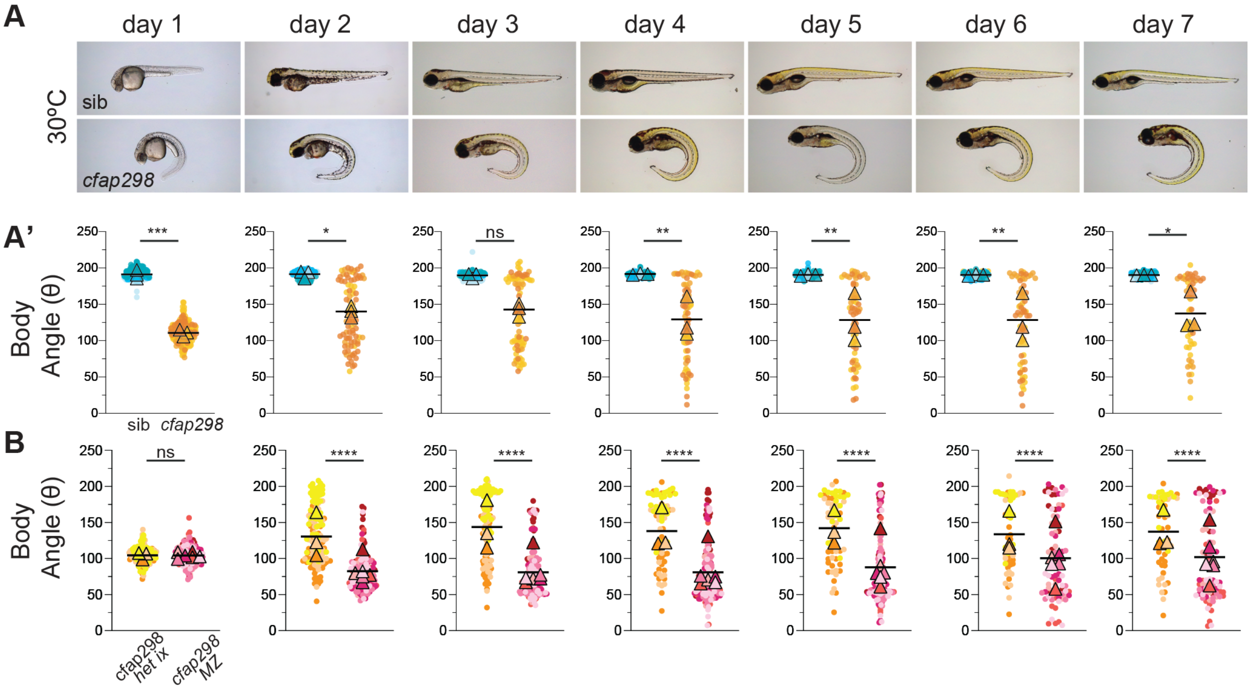

Figure 2.12. Body axis curvature in *cfap298^{tm304}* mutants is temperature dependent. (A-A') Lateral views (A) and quantitation of body curvature (A’) in *cfap298^{tm304}* sibling or homozygous fish over the course of 7 days of development, while housed at restrictive temperatures. (B) Body angle quantitation comparing zygotic and maternal-zygotic *cfap298^{tm304}* mutants. The latter undergoes lower levels of straightening, suggesting a small role for maternally-derived *cfap298* gene product. ****$P < 0.0001$, ***$P < 0.001$, *$P < 0.05$, ns – not significant.

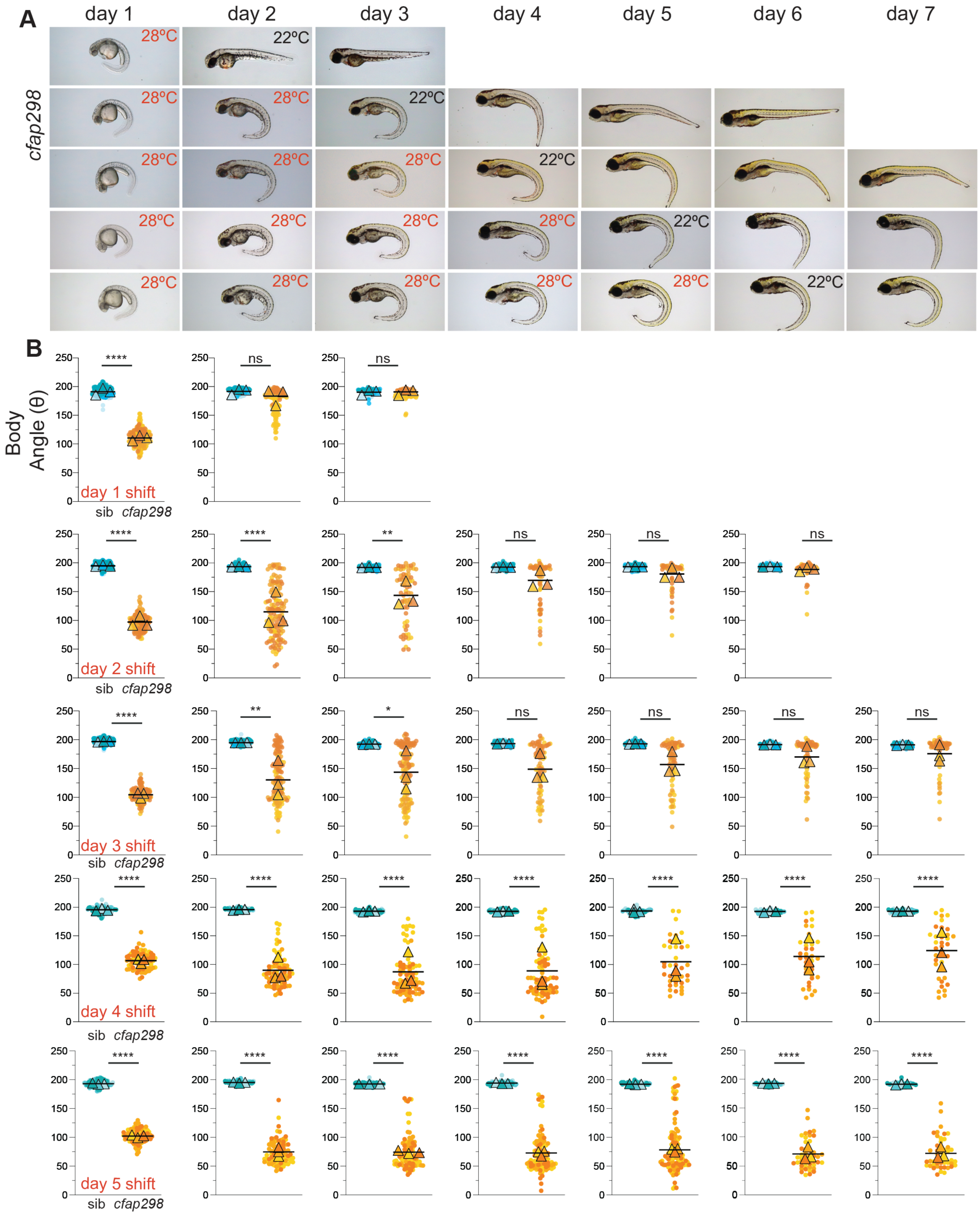

Figure 2.13 Body axis recovery in *cfap298*^{tm304} mutants after temperature shifts. (A-B) Lateral views (A) and quantitation of body curvature (B) in *cfap298*^{tm304} sibling or homozygous fish over the course of 7 days of development, with temperature shifts indicated. ****$P < 0.0001$, ***$P < 0.001$, *$P < 0.05$, ns – not significant.

This demonstrates the ability of early zebrafish larvae to remodel their shape to a 'target morphology' despite diverse starting conditions. During 1-3 dpf, larvae are not normally curved, yet, once cilia motility initiates, curved larvae resolve anatomical abnormalities to generate the wild-type form (Figure 2.11F). This underscores the importance of viewing development as a flexible process that can respond to perturbations, rather than some programmed unfolding of genetically predetermined events. 'Goal state' models in which the organism is viewed as trying to achieve an anatomical set point, can be useful for understanding such phenotypes (Levin, 2021). Zebrafish axial straightening represents a tractable system to delve deeper into the multi-scale processes which sense the current anatomical state and implement changes that move the state towards the target set point.

Phenotypes seen in daw1^{b1403} zebrafish mutants model symptoms seen in patients with mutations in DAW1.

The major motile ciliopathy is primary ciliary dyskinesia (PCD) which afflicts 1 in 10,000 people and is characterized by *situs* abnormalities, reduced mucus clearance leading to airway infections and infertility (Wallmeier et al., 2020). Our collaborators Emma Baple and Andrew Crosby identified patients from two families with laterality defects, mild chronic respiratory symptoms, but no impaired fertility. These patients, along with individuals with congenital heart defects described in Jin et. al. (Jin et al., 2017), were homozygous for mutations in DAW1. Two out of five variants observed contained early stop codons (Trp119* and Leu66*), while three were single nucleotide polymorphisms (SNPs): Asn143Asp, Trp372Cys, and Ser364Thr (Figure 2.14A, Leslie et. al., 2022). To assess the effect of these SNPs, variant mRNA was injected into *daw1*^{b1403} zebrafish embryos at the 1-cell stage, after which cardiac looping laterality was assessed.

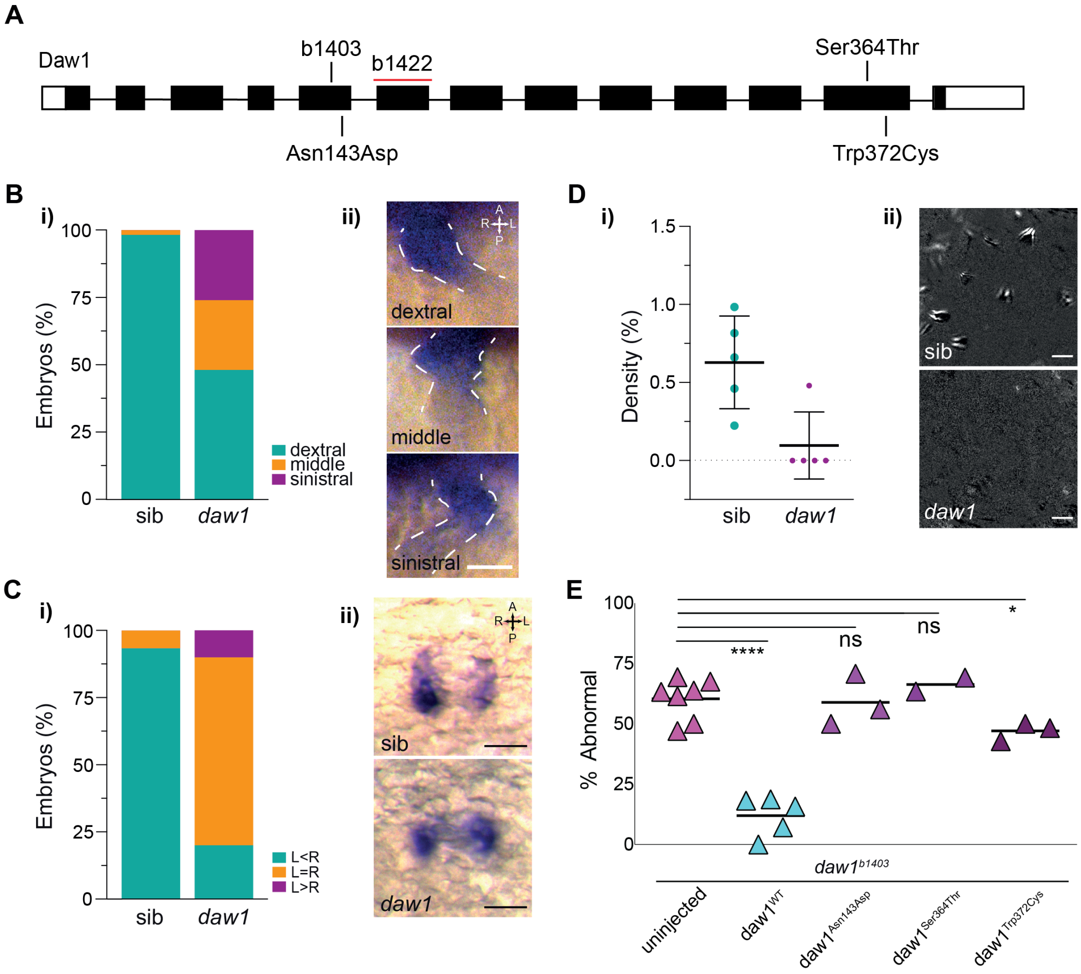

Figure 2.14. In vivo modeling of *DAW1* variants using zebrafish mutants. (A) Schematic showing *DAW1* intron–exon genomic organization, indicating the positions of DAW1 variants as well as relative positions of the zebrafish *daw1* alleles used in this study. (B) Quantitation of cardiac looping phenotypes with representative images in *daw1*^{b1403} mutants ($n = 54$) and sibling controls ($n = 118$). Scale bar: 50 µm. (C) Quantitation of dand5 expression with representative images in *daw1*^{b1403} mutants ($n = 30$) and sibling controls ($n = 30$). Scale bars: 50 µm. (Di) Quantitation of the area occupied by motile cilia in KV at the 10-somite stage. Each data point represents a distinct embryo. (Dii) Representative temporal image correlation spectroscopy images of KV cilia motility where white/gray pixels show regions of periodic motion. Scale bars: 5 µm. (E) Dot plot showing the percentage of *daw1*^{b1403} mutants embryos exhibiting abnormal cardiac looping laterality after injections with mRNA encoding either wild-type or variant Daw1. *$P < .05$; ****$P < .001$; ns, not significant; unpaired t test was applied.

daw1^{b1403} mutants exhibit abnormal cardiac looping at 2 dpf (Figure 2.14B), indicative of L-R patterning. The majority of control embryos showed dextral looping, but *daw1*^{b1403} mutant clutches contained embryos showing sinistral and middle looping as well (Figure 2.14B). Additionally, *daw1*^{b1403} mutants exhibited bilaterally equal *dand5* expression around KV (Figure 2.14C). This structure is equivalent to the mammalian ventral node, and is responsible for creating L-R asymmetry (Essner et al., 2005). Accordingly, a majority control embryos exhibit asymmetric expression of *dand5* around the KV, with higher expression on the right side than the left (Figure 2.14C). *daw1*^{b1403} mutants instead showed bilaterally equal *dand5* expression (Figure 2.14C). To directly assess cilia motility as the cause of this aberrant *dand5* expression, we directly imaged cilia in the KV of *daw1*^{b1403} mutant embryos and controls, observing that motility in *daw1*^{b1403} mutants was almost entirely absent (Figure 2.14D).

Injection of mRNA encoding wild-type Daw1 led to robust rescue of L-R patterning in *daw1*^{b1403} mutants (Figure 14E). By contrast, mRNA containing the Asn143Asp or Ser364Thr human variants failed to rescue mutants (Figure 14E). Expression of Trp372Cys resulted in a partial but minor rescue (Figure 14E). Cilia in the KV were also imaged to directly assess the effect of the human variants on motility. Injection of wild-type *daw1* mRNA robustly rescued cilia motility in *daw1*^{b1403} mutants (Movie 17), but injection of *daw1*^{Asn143Asp} mRNA and *daw1*^{Ser364Thr} mRNA failed to do so (Movie 18 and 19). *daw1*^{Trp372Cys} mRNA partially restored motility, resulting in slower beating (Movie 20), in agreement with the low level rescue of L-R patterning (Figure 14E). Overall, these data showed that all three missense mutations found in patients are loss-of-function, with Asn143Asp and Ser364Thr behaving as nulls and Trp372Cys behaving as a hypomorph. This validates that these variants are likely to be causative in the symptoms exhibited by the patients.

Our model for Daw1 function, in which embryonic cilia that function rapidly are significantly disrupted but cilia at later stages, which function over longer time spans, are not, fits with this unusual combination of symptoms seen in *DAW1* patients. This is likely because ciliated epithelial cells of the respiratory and ovarian tracts comprise, together, hundreds of thousands of cilia which are relatively long-lived, with ciliated cells exhibiting gradual turnover. A potential short-term delay in motility due to slower ODA import after new cilia form within a single region of these ciliated tracts is therefore unlikely to have a substantial impact on overall cilia function at the level of the entire organ, and so would not be expected to cause severe disease. By contrast, the motile cilia in the embryonic node that are crucial for L-R patterning form, function and then regress on the timescale of hours (Little & Norris, 2021), and so rapid onset of motility is essential. In agreement, a *Daw1* mouse mutant exhibited severe L-R patterning defects but relatively minor lung cilia motility abnormalities (Solomon et al., 2017), although mucociliary clearance was still defective in these mutants, suggestive of reduced quality of cilia beating.

Discussion

Daw1, also known as ODA16, has long been known to play a key role in the formation of motile cilia, bridging the gap between ODA's and IFT46 (Dai et al., 2018; Hou & Witman, 2017; Taschner et al., 2017). It was most closely studied in the ciliated alga *Chlamydomonas*, in which loss caused defective cilia motility (Ahmed et al., 2008). This function was later found to be conserved in zebrafish, in which morphants exhibited phenotypes characteristic of other cilia motility mutants such as body axis defects, impaired otolith formation, and aberrant organ laterality (Gao et al., 2010). However, how the loss of Daw1 might affect a developing multicellular organism in the long term remained an unanswered question. *Chlamydomonas* is unicellular, while the limitations of morphlino technology preclude its use to study late stages of development. To fill this gap in knowledge, we used zebrafish to generate a *daw1* germline mutant to study its requirement and role in cilia motility across life stages.

daw1^{b1403} homozygous mutants exhibited scoliosis as adults at a rate of about 20%, far below the expected percentage for cilia motility mutants (close to 100%) (Grimes et al., 2016). However, early phenotypes were much less ambiguous, with complete randomization of heart jogging, indicative of a fully penetrant laterality defect, and 100% of embryos failing to straighten the body axis (Figure 2.1). However, unlike any other cilia motility mutant currently known, *daw1^{b1403}* mutants gradually straightened in a delayed fashion over the following five days post fertilization. High speed imaging within the central canal showed that while at 1 dpf, very few cilia were motile, by between 2 and 3 dpf levels of cilia motility in homozygous mutants were nearly indistinguishable from wild type (Figure 2.5). Generation of mosaic crispants, mRNA rescue (Figure 2.8), and generation of an early stop codon allele (*daw1^{b1422},* Figure 2.10) all indicated that this was not due to a hypomorphic allele in *daw1^{b1403}*, but rather a unique function of Daw1 as a regulator of the timely onset of cilia motility.

This novel result was able to explain the symptoms seen in patients harboring homozygous mutations in *DAW1*. These patients displayed only a subset of symptoms commonly seen in other iterations of PCD, most notably heterotaxy and *situs inversus*, with much less significant lower respiratory symptoms and no evidence of decreased fertility (Leslie et al., 2022). These symptoms, indicative of a defect in cilia motility only early in development, are consistent with phenotypes documented in our $daw1^{b1403}$ zebrafish mutants. To firmly determine the genetic cause of these patients' symptoms, we cloned three point mutations found in human *DAW1*, Asn143Asp, Trp372Cys, and Ser364Thr, and performed over-expression experiments in the background of known loss-of-function allele $daw1^{b1403}$. Over-expression of $daw1^{Asn143Asp}$ mRNA and $daw1^{Ser364Thr}$ mRNA showed an inability to rescue aberrant heart looping laterality or cilia motility in KV, while $daw1^{Trp372Cys}$ mRNA only showed limited rescue ability (Figure 2.14). These experiments demonstrated mutations in *DAW1* were most likely the cause of these patients' symptoms.

Testing human variants in an *in vivo* animal model remains the gold standard in establishing the causal factor among candidate variants in human genetic disorders of uncertain origin (Yamamoto et al., 2024; Baldridge et al, 2021). Rare genetic diseases of unknown cause remain a significant issue in human health (Wang et al., 2022). The difficulty in identifying the genetic underpinnings of disorders can lead to difficulties in determining the best course of treatment as well as frustration among patients who often live for years without a diagnosis. This work on *DAW1* is a prime example of the ways in which basic science studies can advance our understanding of human genetic disorders, as well as firmly connect said disorders to their causative genes.

In a wider context, this study was able to identify *DAW1* as a gene that causes a ciliopathy specific to early development, unique among other motile ciliopathies that commonly have systemic, but occasionally tissue-specific effects (Waters & Beales, 2011). While *DAW1* had previously been implicated in laterality defects, specifically related to congenital heart malformations (Jin et al., 2017), this work has connected this downstream effect to the root cause, the unique function of *DAW1* as a key regulator in the timing of cilia motility.

Furthermore, both the natural response of cilia motility in the absence of Daw1 and experiments with the temperature-sensitive mutant *cfap298*^{tm304} demonstrate the remarkable ability of the zebrafish larva to survey body shape and correct abnormalities. This ability implies the existence of a straight body axis as a 'target morphology.' In wild-type circumstances, the body axis straightens within the first day of development, and its broad shape was previously assumed to be set at this point. Indeed, in most cilia motility mutants that develop ventral curves, that curvature often grows worse over time, with tails sometimes looping around more than 360 degrees (Brand et al., 1996). However, *daw1*^{b1403} mutants and temperature shift experiments with *cfap298*^{tm304} mutants demonstrated that the shape of the body axis is responsive to signals generated by fluid flow up to three days post fertilization, to the extent that most embryos are able to fully recover a straight body axis.

This ability is evolutionarily advantageous for obvious reasons, allowing the organism to adjust for environmental or even naturally occurring genetic disturbances. For up to three days post fertilization, the shape of the zebrafish body axis remains plastic. Like neuroplasticity, in which neural networks are able to reshape themselves in response to trauma or injury (Demarin et al., 2014), the body axis retains a sort of morphogenetic plasticity during a key window in early development, when failure to form the correct shape would be catastrophic (Brand et al., 1996).

Bridge to Chapter III

This chapter describes the role of *daw1* in a complex, vertebrate system as a key regulator of cilia motility onset, explaining an unusual variety of motile ciliopathay found in patients with laterality defects. Additionally, we show that the body axis is responsive to a motile cilia-based signal for three days post-fertilization and retains the ability to straighten in a delayed fashion, although this process grows progressively less effient over developmental time. However, these findings further beg the question of factors downstream of cilia motility in this pathway. In Chapter III, we further investigate two of these factors— the Reissner fiber (RF) and urotensin peptides.

CHAPTER III: THE REISSNER FIBER IS REQUIRED FOR EARLY AXIS STRAIGHTENING, WHILE UROTENSIN II-RELATED PEPTIDES ARE REQUIRED FOR LONG-TERM MAINTENANCE OF THE SPINE

Elements published in *eLife* December 2022

Elizabeth A. Bearce, Zoe H. Irons, Johnathan R. O'Hara-Smith, Colin J. Kuhns, Sophie I. Fisher, William E. Crow, Daniel T. Grimes*

Institute of Molecular Biology, Department of Biology, University of Oregon, Eugene, OR
97403, USA.

*Correspondence (dtgrimes@uoregon.edu)

Introduction

Motile cilia-generated cerebrospinal fluid (CSF) flow is essential for maintaining body and spine morphology (Grimes et al., 2016). Mutants with defective motile cilia fail to undergo axial straightening during embryogenesis and so develope a misshapen early embryonic body axis called ‘curly tail down’ (CTD; Brand et al., 1996). If rescued during this early stage, mutants go on to develop three-dimensional spinal curves that recapitulate some features of idiopathic scoliosis (IS), including adolescent-stage onset in the absence of vertebral patterning defects (Grimes et al., 2016; Marie-Hardy et al., 2021; Wang et al., 2022). Precisely how motile cilia and CSF flow maintain spine morphology during growth is not understood. Specifically, any potential signaling factors stimulated or propagated by motile cilia and CSF flow in the central canal have remained largely mysterious.

However, it is known that cilia motility is essential during early larval stages for the assembly of the Reissner fiber (RF), an extracellular thread-like structure composed predominantly of the large glycoprotein SCOspondin (encoded by *sspo*) which sits in the CSF in brain ventricles and the central canal (Cantaut-Belarif et al., 2018; Rodríguez et al., 1998). Cilia motility is essential for the formation of RF while the RF itself is requried for axial morphogenesis: zebrafish *sspo* mutants exhibit CTD as embryos while hypomorphic mutants which can survive beyond embryonic stages also manifested spinal curves (Cantaut-Belarif et al., 2018; Lu et al., 2020; Rose et al., 2020; Troutwine et al., 2020). Here, we find further evidence for the requirement of SCOspondin and RF by generating and analyzing a new *sspo* mutant, while also combining endogenously labeled SCOspondin (Troutwine et al., 2020) into mutant backgrounds to examine the RF live in the context of no cilia motility (*cfap298*^{tm304}) and delayed cilia motility (*daw1*^{b1403}).

The Urotensin II-related peptides (URPs), Urp1 and Urp2, may also function downstream of motile cilia in the central canal. Urp1 and Urp2 are 10-amino acid cyclic peptides previously linked to heart disease and mental illness (Sugo et al., 2003; Konno et al., 2013; Nobata et al., 2011; Parmentier et al., 2011; Quan et al., 2021; Tostivint et al., 2006; Vaudry et al., 2010). In zebrafish, Urp1 and Urp2 are expressed in CSF-contacting neurons (CSF-cNs), flow sensory neurons in the central canal, and their expression is increased by motile cilia function and the RF (Cantaut-Belarif et al., 2020; Lu et al., 2020; Quan et al., 2015; Zhang et al., 2018). Morpholino knockdown of Urp1/Urp2 resulted in embryonic CTD phenotypes while addition of Urp1/Urp2 peptides can rescue the CTD of cilia motility- and RF-deficient mutants (Lu et al., 2020; Zhang et al., 2018). This suggested that Urp1 and Urp2 act downstream of cilia motility to promote early axial straightening (Grimes, 2019a; Lu et al., 2020; Zhang et al., 2018).

Here, we set out to address whether Urp1 and Urp2 function in maintaining body and spine morphology during growth and adulthood. By generating zebrafish mutants lacking Urp1 and Urp2 peptides, we found, in contrast to previous studies, that they are not essential during embryogenesis. Nevertheless, Urp1 and Urp2 do play largely redundant roles in adult spine morphology. Loss of Urp1 and Urp2 together led to the onset of spinal curves during adolescent stages and, by adulthood, resulted in planar curves in the caudal region of the spine that occurred without vertebral patterning defects or significant structural malformations. A similar phenotype was present upon mutation of the urotensin receptor (UT) gene, *uts2r3*, suggesting that Urp1 and Urp2 signal via Uts2r3 to maintain spine morphology. Overall, this demonstrates that Urp1 and Urp2 peptides control the morphology of the zebrafish spine and contrasts previous findings using morphants that suggested a more significant role in early embryogenesis (Zhang et al., 2018). We suggest that urotensin-deficient zebrafish model human spinal deformities and will be important tools for deciphering how the spine is maintained and how this process goes wrong in disease.

Results

sspo mutants exhibit curly tail down, and the Reissner fiber fails to assemble in the absence of cilia motility

To confirm that the RF is required for axial straightening, I generated a loss-of-function mutation in the coding sequence for the protein SCOspondin, called *sspo*^{b1446}, which contains an early stop codon in exon 5 (Figure 3.1A,B). *sspo*^{b1446} mutants failed to straighten, exhibiting CTD phenotypes that were indistinguishable from the cilia motility mutant *cfap298*^{tm304} (Figure

3.1C). This coheres with a model in which motile cilia promote the formation of the RF and that the RF then somehow results in axial straightening.

To assess whether motile cilia promote RF formation, we acquired the *sspo-GFP* line from Troutwine et. al. (Troutwine et al., 2020), in which SCOspondin, and therefore the RF, is endogenously labeled with GFP. By combining this with our previously described *cfap298*^{tm304} mutant line, we were able to image SCOspondin in the central canal in the absence of cilia motility and fluid flow. Compared to control embryos, in which SCOspondin generated a clear RF within the central canal, SCOspondin in *cfap298*^{tm304} mutants appeared diffuse throughout the lumen, failing to form a definitive fiber (Figure 3.1D).

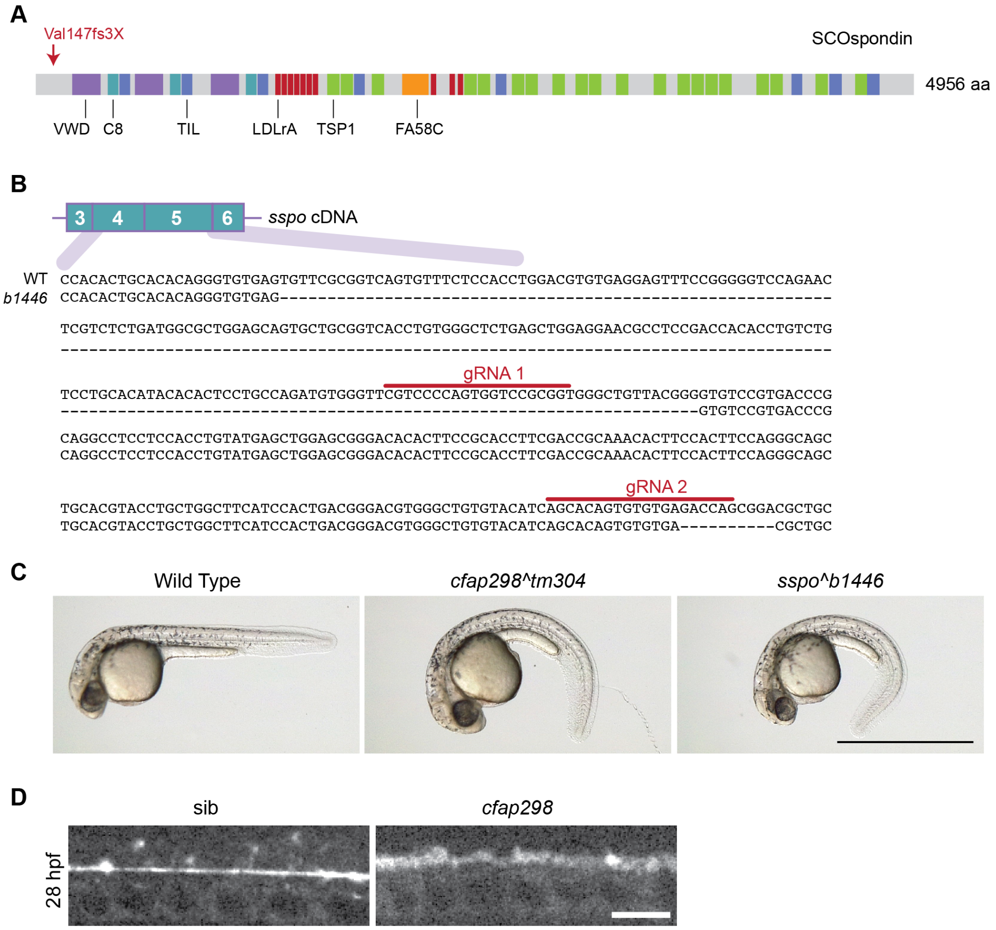
A
Val147fs3X
SCOspondin
4956 aa
VWD
C8
TIL
LDLrA
TSP1
FA58C
B
3
4
5
6
sspo cDNA
WT
b1446
CCACACTGCACACAGGGTGTGAGTGTTCGCGGTCAGTGTTTCTCCACCTGGACGTGTGAGGAGTTTCCGGGGGTCCAGAAC
CCACACTGCACACAGGGTGTGAG--
TCGTCTCTGATGGCGCTGGAGCAGTGCTGCGGTCACCTGTGGGCTCTGAGCTGGAGGAACGCCTCCGACCACACCTGTCTG
----
gRNA 1
TCCTGCACATACACACTCCTGCCAGATGTGGGTTCGTCCCCAGTGGTCCGCGGTGGGCTGTTACGGGGTGTCCGTGACCCG
---GTGTCCGTGACCCG
CAGGCCTCCTCCACCTGTATGAGCTGGAGCGGGACACACTTCCGCACCTTCGACCGCAAACACTTCCACTTCCAGGGCAGC
CAGGCCTCCTCCACCTGTATGAGCTGGAGCGGGACACACTTCCGCACCTTCGACCGCAAACACTTCCACTTCCAGGGCAGC
gRNA 2
TGCACGTACCTGCTGGCTTCATCCACTGACGGGACGTGGGCTGTGTACATCAGCACAGTGTGTGAGACCAGCGGACGCTGC
TGCACGTACCTGCTGGCTTCATCCACTGACGGGACGTGGGCTGTGTACATCAGCACAGTGTGTGA----------CGCTGC
C
Wild Type
cfap298^tm304
sspo^b1446
D
sib
cfap298
28 hpf

Figure 3.1. *sspo^{b1446}* mutants display CTD due to their inability to form a Reissner fiber. (A) Schematic of zebrafish SCOspondin protein showing domain architecture based on Troutwine et al., 2020. VWD – von Willebrand factor type D domain; C8 – C8 domain; TIL – trypsin inhibitor like cysteine rich domain; LDLrA – low-density lipoprotein receptor class A domain; TSP1 – thrombospondin type 1 domain; FA58C – coagulation factor 5/8 C-terminal domain. In *sspob^{1446}* mutants, a genomic deletion results in a frame shift mutation at Valine 147 resulting in an early premature truncation codon. (B) The *sspob^{1446}* mutants line harbors a large deletion and a downstream small deletion which disrupt exons 4 and 5 causing the early truncation of Sspo. (C) *sspob^{1446}* mutants develop CTD at 28 hpf, like the cilia motility mutant *cfap298^{tm304}*. Scale bar: 1mm (D) Grayscale maximal intensity projection of Sspo-GFP localization in the central canal in 28 hpf embryos. Scale bar: 10µM

To test whether delayed onset of cilia motility could induce this fiber to form in a delayed fashion, we combined *sspo-GFP* with the previously described *daw1^{b1403}* mutant. We then imaged both cilia motility and *sspo-GFP* at five points along the body axis as the fiber was formed (Figure 3.2A,D). The FreQ Fourier transformation pipeline (Jeong et al., 2022) was used to analyze cilia motility and calculate beat frequency. At 25 hpf, wild type embryos exhibited cilia motility at all points imaged along the body axis; the weakest beating being at the most caudal region of the CC. Accordingly, a clearly defined RF could be seen at all points except the most caudal (Figure 3.2B). As previously described, at 25hpf *daw1^{b1403}* mutants showed reduced beating at all points along the central canal (Figure 3.2C). In correspondence with this weaker motility, *daw1^{b1403}* mutants had a less clear, "fuzzier," RF that often failed to form beyond the midpoint of the body axis (Figure 3.2C). This supports the model that early in development, cilia motility is weaker in the caudal region as compared to the rostral region, and weaker motility corresponds to a failure of the RF to form. Later in development at 43 hpf, cilia motility in wild type embryos strengthened in all regions measured, corresponding to a complete RF that stretched to the most caudal region (Figure 3.2E). In accordance with the characteristic phenotype of *daw1^{b1403}* mutants described in Chapter III and Bearce et. al. (Bearce, Irons, Craig, et al., 2022), the delayed onset of cilia motility corresponded to the delayed formation of the RF, in a rostral-to-caudal direction (Figure 3.2F). These results cohere with the notion that cilia motility is essential for RF formation and that the RF is then essential for axial straightening. Importantly, the RF can form in a delayed fashion, explaining the late-onset axial straightening we observed upon mutation of *daw1*.

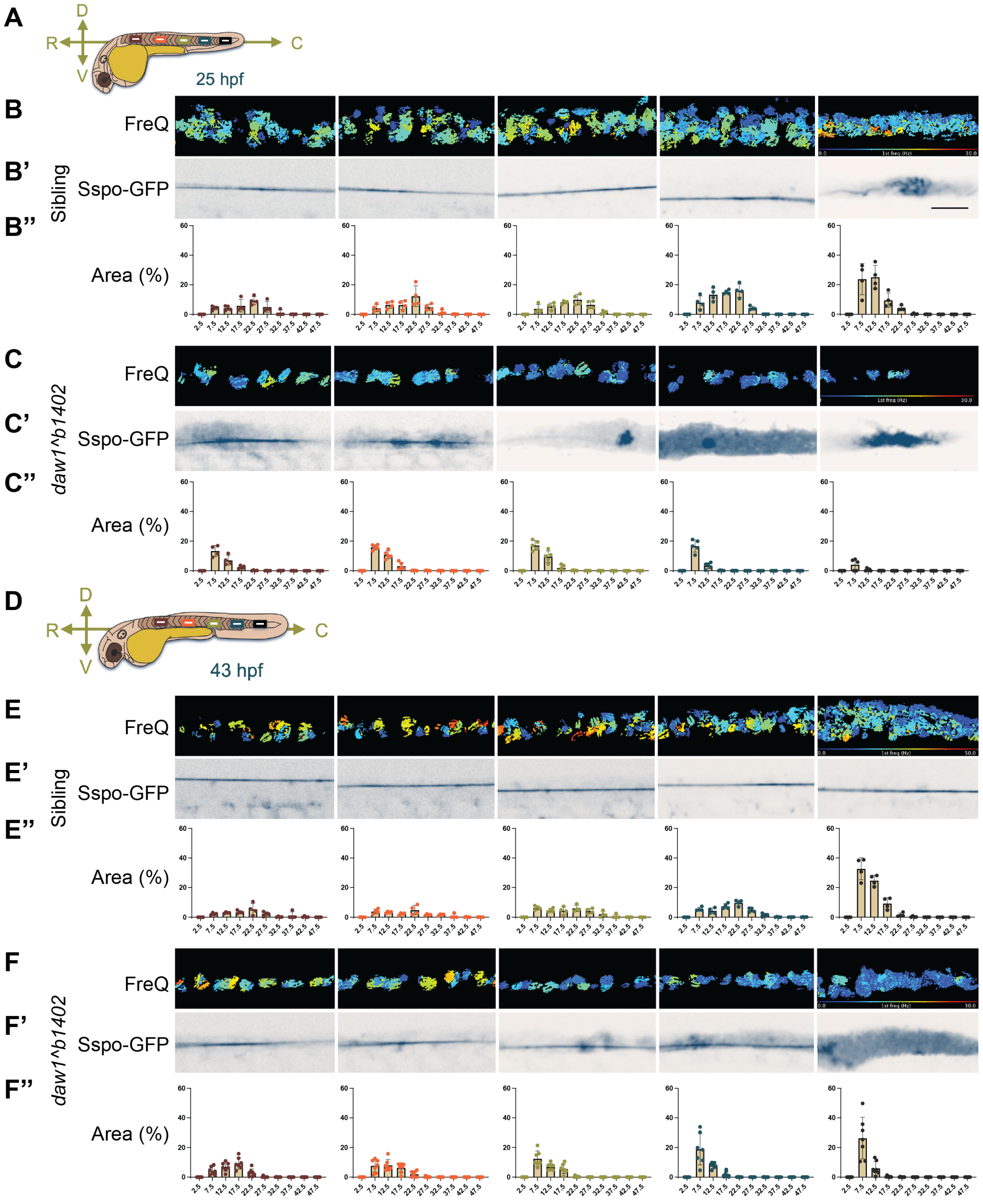

Figure 3.2. The Reissner fiber assembles in a delayed fashion in $daw1^{b1403}$ mutants. (A) Central canal imaging was performed in 25 hpf embryos from five regions along the R-C axis spaced five somites apart. (B) Cilia beat frequency visualizations from FreQ analysis of DIC live imaging (250Hz frame rate, 2.5sec duration) (Jeong et al., 2022). (B') Live confocal imaging of Sspo-gfp and (B'') histogram quantitation of cilia beat frequencies (Hz) in $daw1^{b1403}$ siblings at 25 hpf. (C) FreQ, (C') Sspo-GFP, and (C'') quantitation of cilia beat frequency (Hz) in $daw1^{b1403}$ mutants at 25 hpf. (D) Central canal imaging was performed in 43 hpf embryos in five regions along the R-C axis spaced five somites apart. (E) FreQ TICS (Jeong et al., 2022), (E') Sspo-GFP, and (E'') quantitation of cilia beat frequency (Hz) in $daw1^{b1403}$ siblings at 43 hpf. (F) FreQ TICS (Jeong et al., 2022), (F') Sspo-GFP, and (F'') quantitation of cilia beat frequency (Hz) in $daw1^{b1403}$ mutants at 43 hpf. Scale bar: 10µm

Urp1 and Urp2 peptides are dispensable for embryonic axial straightening

To determine whether Urp1 and Urp2 are required for spine morphology, we used CRISPR/Cas9 to generate zebrafish mutant lines. Urp1 and Urp2 are encoded by 5-exon genes with the final exon coding for the 10-amino acid peptides that are released by cleavage from the pro-domain (Figure 3.3A-D). We used pairs of guide RNAs to induce deletions across the genetic region coding for the peptides (Figure 3.3C; Figure 3.4A-B). We refer to the resulting mutant lines as $urp1^{\Delta P}$ and $urp2^{\Delta P}$ because they lack the peptide coding sequence. In addition, mRNA quantitation revealed downregulation of *urp1* and *urp2* in their respective mutant backgrounds, indicating transcript decay (Figure 3.4E).

We first assessed $urp1^{\Delta P}$ and $urp2^{\Delta P}$ mutants for embryonic phenotypes. A previous morpholino-based knockdown study concluded that Urp1 and Urp2 are required for axial straightening, the process by which the ventrally curved zebrafish embryo straightens as the trunk elongates and detaches from the yolk (Figure 3.3E). Urp1/Urp2 morphants failed to undergo straightening and therefore displayed CTD (Zhang et al., 2018). Surprisingly, both $urp1^{\Delta P}$ and $urp2^{\Delta P}$ mutants underwent normal axial straightening and did not exhibit CTD (Figure 3.3Gi). By contrast, we observed CTD in both $cfap298^{tm304}$ mutants that lack cilia motility in the central canal (Bearce, Irons, Craig, et al., 2022) and *sspo*^{b1446} mutants, as expected (Figure 3.3Gi; Figure 3.1). Notably, *cfap298*^{tm304} and *sspo*^{b1446} mutants maintained *urp1* and *urp2* expression in CSF-cNs, central canal neurons marked by *pkd2l1* expression (Figure 3.3F). However, *urp1* and *urp2* transcripts were quantitatively reduced in *cfap298*^{tm304} and *sspo*^{b1446} mutants (Figure 3.3H). We reasoned that the absence of CTD in *urp1*$^{\Delta P}$ and *urp2*$^{\Delta P}$ mutants might reflect redundancy, since Urp1 and Urp2 peptides are highly similar, with identical hexacyclic regions (Figure 3.3A-B,D). Alternatively, maternally derived *urp1* and/or *urp2* transcripts may function to prevent phenotypes from manifesting. However, maternal zygotic *urp1*$^{\Delta P}$;*urp2*$^{\Delta P}$ double mutants also exhibited linear body axes (Figure 3.3Gi), ruling out redundant or maternal gene product function. This demonstrates that Urp1 and Urp2 peptide-null mutants undergo axial straightening.

To confirm this finding, we performed additional Urp1 and Urp2 loss-of-function experiments. By injecting four guide RNAs (gRNAs) along with Cas9 into wild-type embryos at the one-cell stage, we generated mosaic mutants, called crispants, that were then assessed for body shape phenotypes (Figure 3.3I). In positive control experiments, *cfap298* and *sspo* crispants exhibited robust CTD, phenocopying germline *cfap298*^{tm304} and *sspo*^{b1446} mutants (Figure 3.3Gii). Quantitation of body curvature revealed that crispant generation was highly efficient, with CTD penetrance being close to 100% (Figure 3.3J). By contrast, *urp1* and *urp2* single and double crispants exhibited straight body axes that were not different to uninjected embryos or embryos injected with Cas9 only (Figure 3.3Gii,J). Using T7 endonuclease assays, we confirmed that high levels of insertion-deletion mutations were generated at gRNA sites in crispants (Figure 3.4C-D). We used the AB genetic background for the majority of our work, but we also generated and phenotyped *urp1;urp2* double crispants on WIK and TU backgrounds to test for potential background effects. Normal axial straightening upon mutation of *urp1* and *urp2* was also observed on these backgrounds (Figure 3.4F). Overall, crispant results confirmed germline mutant findings. We conclude that Urp1 and Urp2 peptides are dispensable for axial straightening in embryonic zebrafish.

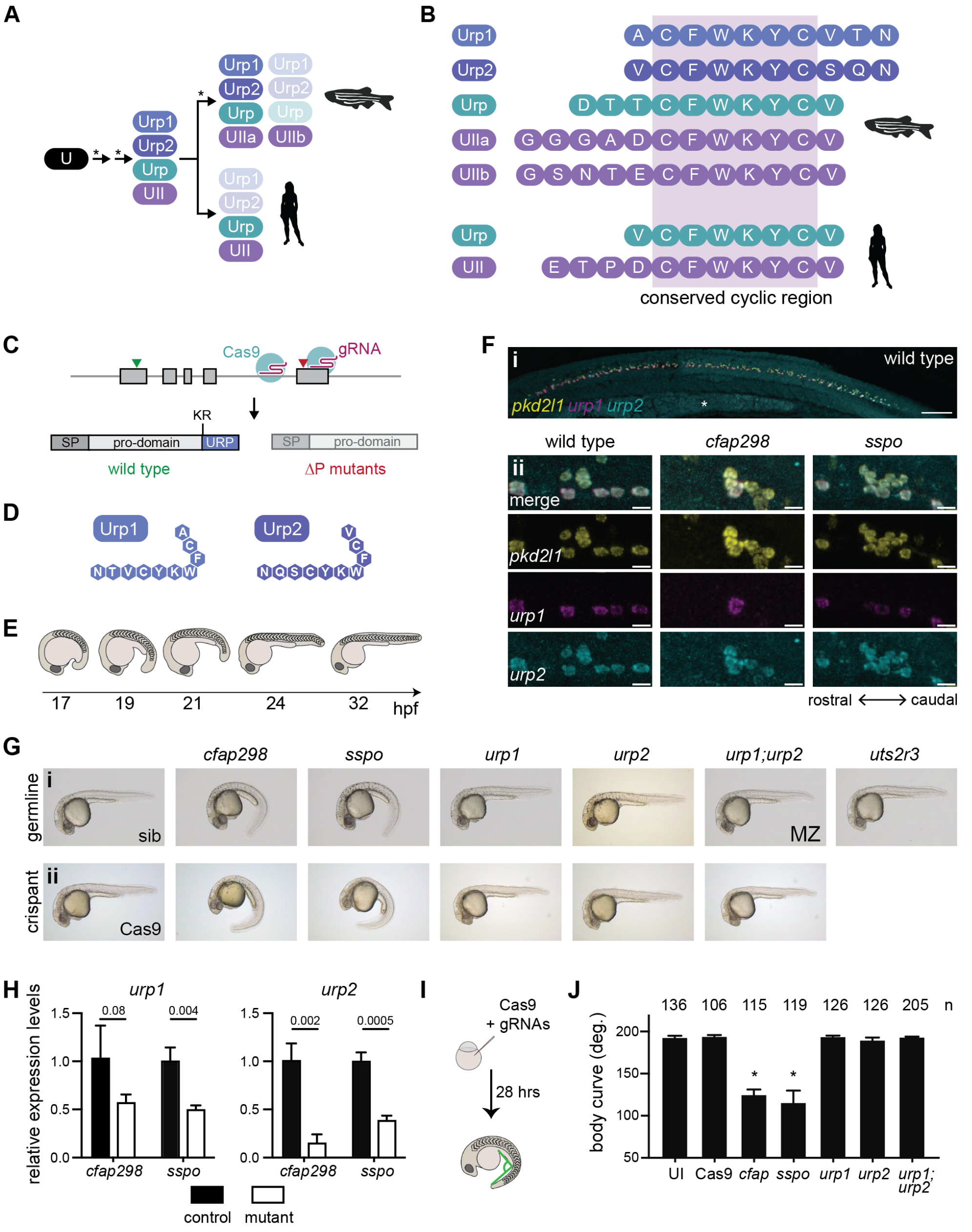
A
U
Urp1
Urp2
Urp
UII
Urp1 Urp1
Urp2 Urp2
Urp Urp
UIIa UIIb
Urp1
Urp2
Urp
UII
B
Urp1 A C F W K Y C V T N
Urp2 V C F W K Y C S Q N
Urp D T T C F W K Y C V
UIIa G G G A D C F W K Y C V
UIIb G S N T E C F W K Y C V
Urp V C F W K Y C V
UII E T P D C F W K Y C V
conserved cyclic region
C
Cas9
gRNA
KR
SP pro-domain URP
SP pro-domain
wild type
ΔP mutants
D
Urp1
A C F N T V C Y K W
Urp2
V C F N Q S C Y K W
E
17 19 21 24 32 hpf
F
i
wild type
pkd2l1 urp1 urp2
wild type cfap298 sspo
ii
merge
pkd2l1
urp1
urp2
rostral ⟷ caudal
G
cfap298 sspo urp1 urp2 urp1;urp2 uts2r3
germline i
sib
MZ
crispant ii
Cas9
H
urp1
urp2
relative expression levels
1.5 1.0 0.5 0.0
0.08 0.004
0.002 0.0005
cfap298 sspo
control mutant
I
Cas9 + gRNAs
28 hrs
J
136 106 115 119 126 126 205 n
body curve (deg.)
200 150 100 50
UI Cas9 cfap sspo urp1 urp2 urp1; urp2

Figure 3.3 Urp1 and Urp2 are dispensable for axial straightening. (A) Successive rounds of genome duplications (*) and divergence converted an ancient urotensin protein (U) into the urotensin II (UII) and urotensin II-related (URP) proteins, some of which have subsequently been lost. (B) The UII and URP proteins in zebrafish and human are 8–12 amino acid peptides with a fully conserved hexacyclic region of sequence CFWKYC. (C) *urp1* and *urp2* are 5-exon genes (gray boxes). The final exon codes for the 10-amino acid peptides produced after cleavage from the prodomain at a dibasic site (KR). Pairs of gRNAs were used to induce deletions of Urp1 and Urp2 peptide coding sequences, resulting in *urp1*$^{\Delta P}$ and *urp2*$^{\Delta P}$ mutants, respectively. SP – signal peptide. (D) Urp1 and Urp2 peptide sequences with identical hexacyclic regions. (E) Zebrafish posterior axial straightening, the morphogenetic process which straightens the embryonic body. (F) Fluorescence in situ hybridization based on hybridization chain reaction analysis of *pkd2l1*, *urp1,* and *urp2* expression in the central canal at 28 hpf. *pkd2l1* expression marks CSF-cNs. *urp1* expression is restricted to ventral CSF-cNs while *urp2* is expressed in all CSF-cNs. Both *urp1* and *urp2* are expressed in *cfap298*^{tm304} and *sspo*^{b1446} mutants, though comparison of expression between samples was non-quantitative. (i) Shows the zebrafish trunk with the yolk stalk labeled (*). (ii) Shows zoomed regions taken at the rostro-caudal level at the end of the yolk stalk. Scale bars: 150 µm (i), 10 µm (ii). (G) Lateral views of 28–30 hpf germline mutants (i) and crispants (ii). The *urp1*$^{\Delta P}$*;urp2*$^{\Delta P}$ double mutants are maternal zygotic (MZ) mutants. Sibling (sib) and Cas9-only injected embryos served as controls. All embryos were incubated at 28°C, which is a restrictive temperature for *cfap298*^{tm304}. (H) Quantitative reverse transcriptase PCR (qRT-PCR) analysis of *urp1* and *urp2* mRNA expression levels in *cfap298*^{tm304} and *sspo*^{b1446} mutants at 28 hpf. n>3 biologically independent samples. Bars represent mean ± s.e.m. Two-tailed student's *t* test used to calculate p-values. (I) Schematic of crispant generation and body curve analysis. (J) Quantitation of crispant body curves where bars represent mean ± s.d. for at least three independent clutches and injection mixes. The total number of embryos analyzed is given. *p<0.0001, student's *t* test applied. UI – uninjected.

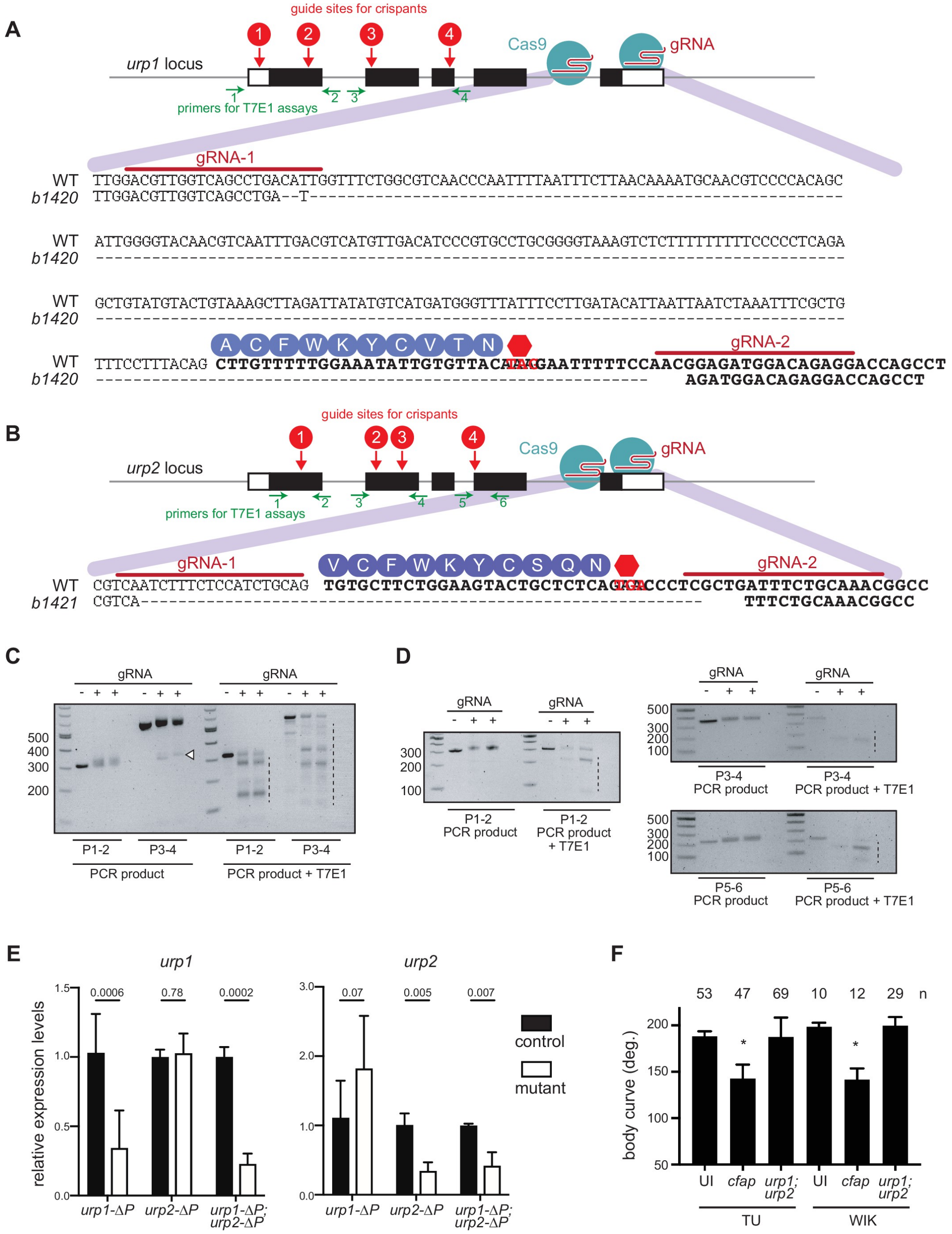

Figure 3.4. Generation of *urp1*$^{\Delta P}$ and *urp2*$^{\Delta P}$ mutants. (A–B) Pairs of guide RNAs (gRNAs) were used to delete genomic regions coding for the Urp1 and Urp2 peptides. The *urp1*^{b1420} (*urp1*$^{\Delta P}$) allele encodes a 279 bp deletion and 1 base pair insertion that removes a portion of intron 4–5 and the coding part of exon 5 including the entire region coding for the Urp1 peptide. The *urp2*^{b1421} (*urp2*$^{\Delta P}$) allele encodes a 61 base pair deletion which removes the region coding for the Urp2 peptide. Red arrows show the location of gRNA sites (1–4) used to generate crispants. Green arrows show the location of PCR primers used to amplify regions around gRNA sites. (C–D) T7E1 assays show significant mutagenesis at *urp1* (C) and *urp2* (D) loci in crispant

embryos. Embryos were injected with Cas9 only (−) or Cas9 plus gRNAs 1–4 (+) then, at 1 dpf, DNA was extracted and regions amplified using the indicated primer pairs. PCR product from crispant embryos showed wider bands, indicating insertion-deletion (indel) mutations, as well as deletion bands (white arrow head), indicating large deletions between two gRNA sites. After PCR, product was purified and subjected to digestion with T7E1, which cleaves heteroduplex DNA. Little or no cleavage was observed in Cas9 only injected embryos, but significant digestion was found in Cas9 + gRNA injected embryos (dashed lines), indicating that indels had been created. Small amounts of T7E1 digestion products in Cas9 only embryos were likely due to the presence of single nucleotide polymorphisms between chromosomes. (E) Quantitative reverse transcriptase PCR (qRT-PCR) analysis of *urp1* and *urp2* mRNA expression levels in *urp1*$^{\Delta P}$ and *urp2*$^{\Delta P}$ single and double mutants at 28 hpf. n>3 biologically independent samples. Bars represent mean ± s.e.m. Two-tailed student's *t* test was used to calculate p-values. (F) Quantitation of crispant body curves where bars represent mean ± s.d. for at least three independent clutches and injection mixes. The total number of embryos analyzed is given. *p<0.001, student's *t* test applied. UI – uninjected. *cfap* – *cfap298*.

Urp1 and Urp2 function semi-redundantly to maintain spine morphology

Next, we determined the impact of Urp1 and Urp2 loss on adult spine morphology. Outwardly, *urp1*$^{\Delta P}$ mutant adults at 3 months post fertilization (mpf) appeared normal whereas *urp2*$^{\Delta P}$ mutants exhibited minor body dysmorphologies and kinked tails (n=72 for *urp1*$^{\Delta P}$ mutants and n=92 for *urp1*$^{\Delta P}$ mutants, Figure 3.5A). To assess spine morphology directly, we imaged bone by X-ray microcomputed tomography (μCT). Three-dimensional reconstitutions of μCT data from 3 mpf fish showed that *urp1*$^{\Delta P}$ mutants indeed exhibited overtly normal skeletal morphology (n=7) while *urp2*$^{\Delta P}$ mutants showed slight sagittal curves (n=4; Figure 3.6A). By contrast to these absent or mild deformities in single mutants, *urp1*$^{\Delta P}$;*urp2*$^{\Delta P}$ double mutants exhibited prominent curves, with significant dorsal-ventral Cobb angles, a measure of deviation from straightness, especially in the caudal region of the spine (Figure 3.7B,D-F; Figure 3.5A; Figure 3.6A). These data indicate that Urp1 and Urp2 are essential for adult spine morphology, and that they function in a semi-redundant fashion in this context.

To assess the long-term maintenance of spine morphology in Urp1- and Urp2-deficient conditions, we aged *urp1*$^{\Delta P}$ and *urp2*$^{\Delta P}$ single mutants to 12 mpf then performed µCT. At this later time point, *urp1*$^{\Delta P}$ and *urp2*$^{\Delta P}$ mutants exhibited mild kyphosis-like curves, though *urp2*$^{\Delta P}$ mutants were more severe (Figure 3.6B). These degenerative phenotypes demonstrate that Urp1 and Urp2 are essential for maintenance of spine morphology throughout adulthood and aging, and suggest that Urp2 plays a larger role than Urp1.

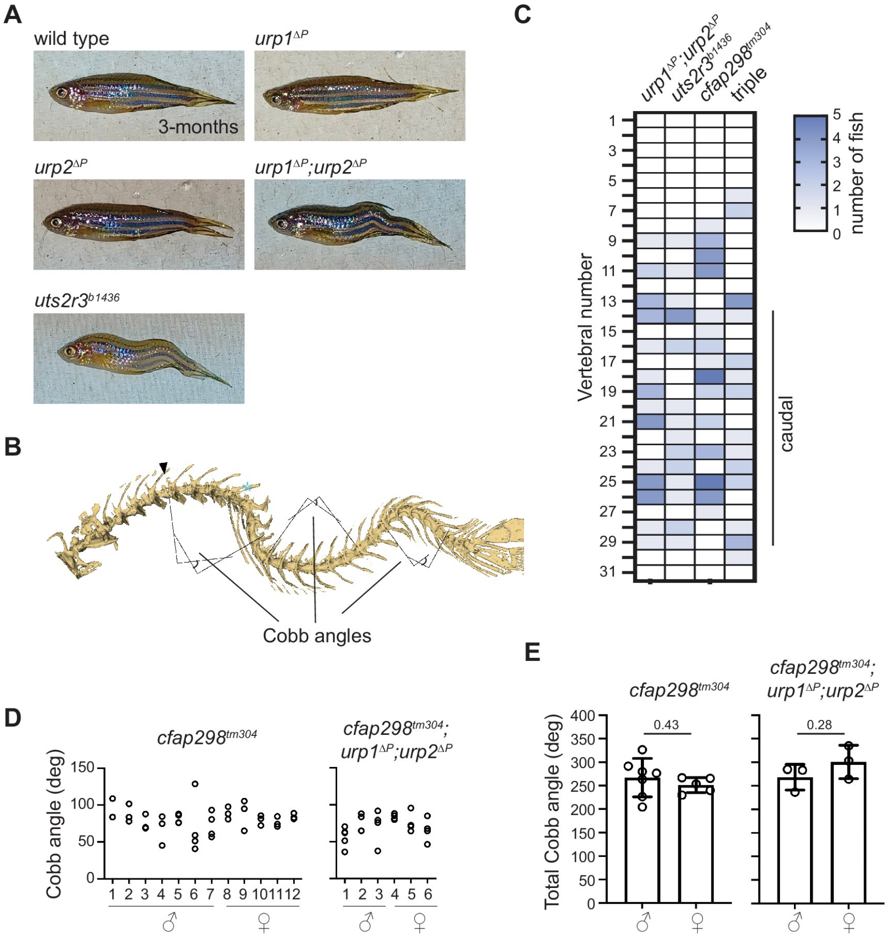

Figure 3.5. Phenotyping spinal curves. (A) Lateral views of adult zebrafish. (B) Cobb angles were measured from lateral views of microcomputed tomography reconstitutions. Right angles are assigned parallel to the rostral and caudal face of the first and last displaced vertebra, respectively, and the external angle is taken at their intersection. The angle was assigned to its most displaced apex vertebra (cyan asterisk) in heat map representations. Note that displaced

vertebrae do not always demonstrate an easily identifiable wedge in intervertebral space, as is typical in human data. In these cases, the first or last vertebrae of the curve is designated as 'least parallel' to the local orientation of the spine. (C) The position of curve apex is plotted for *cfap298^{tm304}* mutants and *cfap298^{tm304};urp1$^{\Delta P}$;urp2$^{\Delta P}$* triple mutants (triple) alongside *urp1$^{\Delta P}$;urp2$^{\Delta P}$* and *uts2r3^{b1436}* mutants for comparison. See also Figure 3.7F. (D) Cobb angle measurements for individual fish in the sagittal plane for *cfap298^{tm304}* and *cfap298^{tm304};urp1$^{\Delta P}$;urp2$^{\Delta P}$* mutants. Circles represent angles for individual curves. (E) Total Cobb angles with each circle representing an individual fish. The mean ± s.d. is shown. p-Values are given from two-tailed unpaired student's *t* tests.

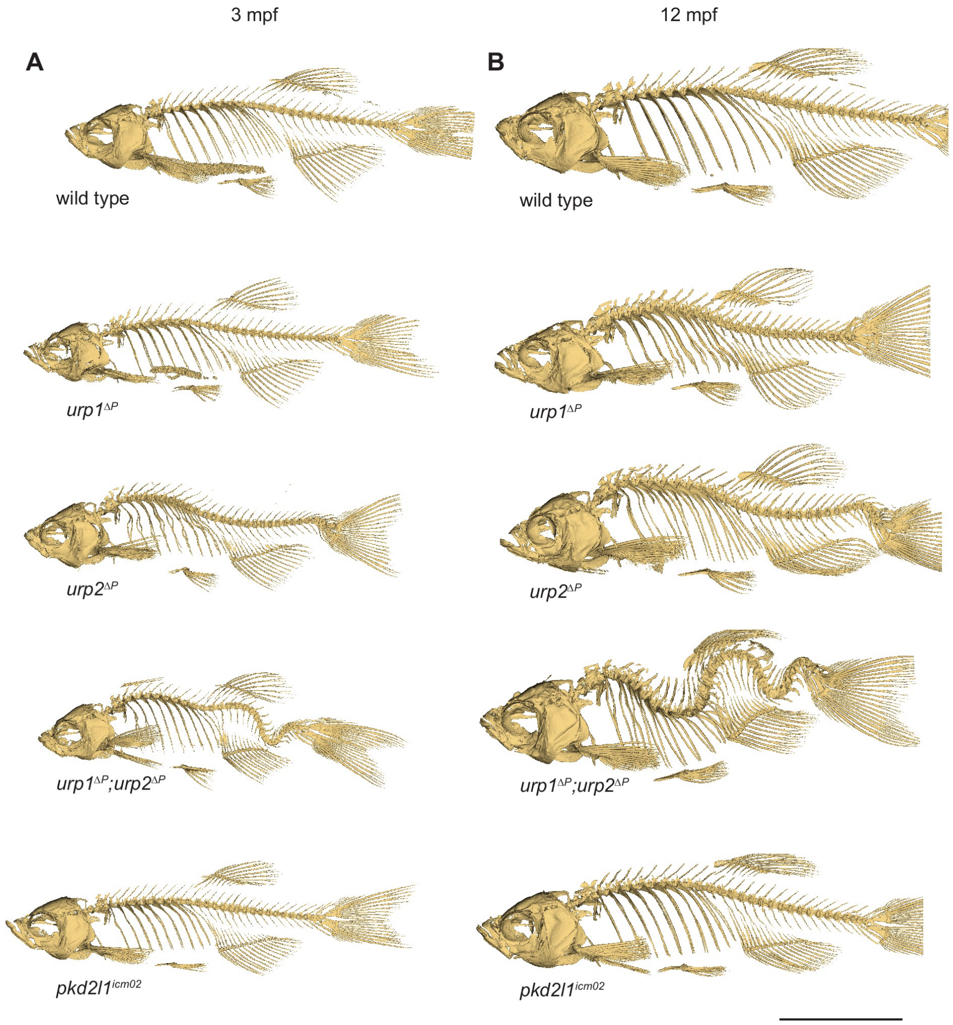

Figure 3.6. Spinal curves in *urp1$^{\Delta P}$*, *urp2$^{\Delta P}$*, *urp1$^{\Delta P}$;urp2$^{\Delta P}$*, and *pkd2l1^{icm02}* mutants degenerate with age. (A–B) Lateral views of microcomputed tomography reconstituted skeletons at 3 mpf (A) and 12 mpf (B) show curves worsen with age. All fish shown are female. Scale bar: 10 mm.

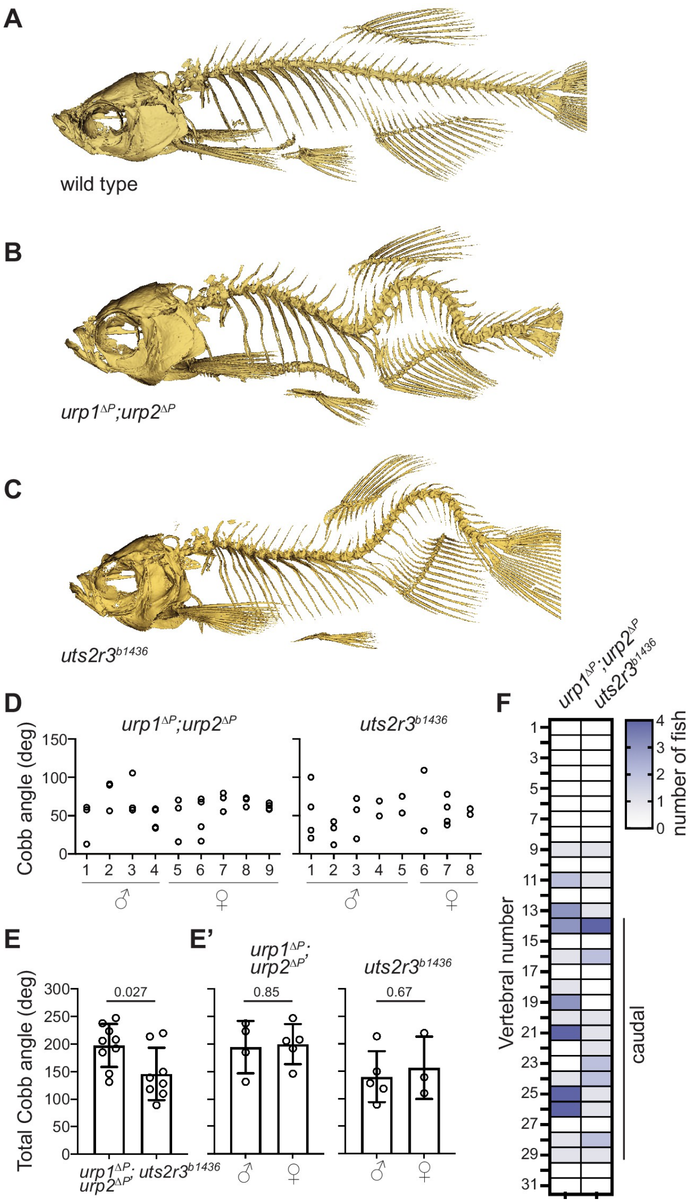

Figure 3.7. Urp1 and Urp2 are required for proper adult spine morphology. (A–C) Lateral views of microcomputed tomography reconstitutions of wild-type (A), *urp1*$^{\Delta P}$*;urp2*$^{\Delta P}$ (B) and *uts2r3*^{b1436} (C) mutants at 3 mpf. (D) Cobb angle measurements for individual fish in the sagittal plane for *urp1*$^{\Delta P}$*;urp2*$^{\Delta P}$ and *uts2r3*^{b1436} mutants. Circles represent angles for individual curves. (E-E') Total Cobb angles with each circle representing an individual fish. The mean ± s.d. is shown. (G') is the data from G parsed for sex. p-Values are given from two-tailed unpaired student's *t* tests. (F) The position of curve apex is plotted and shows that most curves are in caudal vertebrae. n=9 and 8 for *urp1*$^{\Delta P}$*;urp2*$^{\Delta P}$ and *uts2r3*^{b1436} mutants, respectively.

Urp1 and Urp2 signal through the Uts2r3 receptor to control spine morphology

Urp1 and Urp2 peptides engage G-protein-coupled receptors (Ames et al., 1999; Chatenet et al., 2004; Elshourbagy et al., 2002; Labarrère et al., 2003; Liu et al., 1999; Nothacker et al., 1999). While a single urotensin II receptor (UT) gene is found in humans and has recently been linked to abnormal spinal curvature (Dai et al., 2021), the zebrafish genome encodes five such receptors. One of those, Uts2r3, was previously implicated in spine morphology (Zhang et al., 2018). To systematically compare the effects of Uts2r3 receptor mutation with loss of Urp1 and Urp2, we generated a *uts2r3* mutant line harboring a 178-amino acid deletion after the third amino acid, significantly disrupting the protein (Figure 3.8). Like *urp1*$^{\Delta P}$;*urp2*$^{\Delta P}$ double mutants, these *uts2r3*^{b1436} mutants underwent normal axial straightening as embryos (Figure 3.3Gi) and went on to exhibit spinal curves as adults (Figure 3.7C;Figure 3.5A). Cobb angle measurements showed that *uts2r3*^{b1436} mutants and *urp1*$^{\Delta P}$;*urp2*$^{\Delta P}$ mutants were similar, though curves in *urp1*$^{\Delta P}$;*urp2*$^{\Delta P}$ mutants were slightly more severe (Figure 3.7D-E). Like *urp1*$^{\Delta P}$;*urp2*$^{\Delta P}$ mutants, *uts2r3*^{b1436} mutants showed mostly caudally located curves, especially in the most rostral of the caudal vertebrae (Figure 3.7F). Thus, although we cannot rule out minor roles for other UT receptors, these data suggest that Urp1 and Urp2 control spine morphology largely by signaling through Uts2r3.

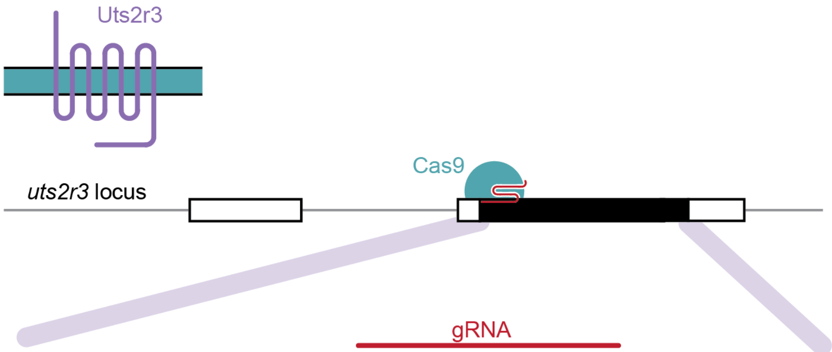

```
ATGGATATACCTGGTTCTACTTCCCTCTTCTCTTCCCCTTCACCTTCATACACCTTTCCT
TTTTTCACTAACCTTTCCTTTCCCTCATCATCACCCTCTCTCTCCCCATCCCCAAGTGTA
GCTTCCACTGCTCTCTTCTGCTTTTTCCTATCCCTCCTTTCTCTGTTGGGTATTCTGGGC
AACTTGTACACCCTAGTACTTCTCCTTCGCCGCCGCAGAATGTCAAGAAGGCGGCATACT
GCTCCTATGTGTTGTTACAGTCTGTCCTGCCTCGGTTCTTCCTCCCCTTCTTTCTCTCCC
TCTTTTTCTCCATCTTCCTCTCCCACATCTTCCTCCTCCTCTTCCTCTCTTCACCTGCAG
GTTCTGAGTCTGGCTTTAGCAGATTTGGTGTACCTGTCCACTGCCCCTTTCATTGTGTAT
GACAGTCTGGCATCTGACTGGGCATTTGGCGAACTTGGCTGTCGACTCCTACTCAGTCTG
GACTTGTTAACAATGCACGCAAGCATCTTTACCCTCACCGCTATGAGTCTGGATCGGTAT
CGAGCTGTGGCCGATCCATTGGCAACCACATCCACACCATCCTCTGGACTTTTAAGAGTC
GCTTTGGCCTGGGGCTTTGCCATCGCTCTCAGTTTGCCCATGATGATTACTTTGCACCTT
GAAGATGGAGAGAACCATGAAGGAAAGTTGTGTGTTCCTGCCTGGGATGAGCAGAGTTCG
AAAGCCTACCTCAGTATCCTCTTCTGCACCAGTATCCTAGGCCCAGGACTGGCAATTGGA
GCTTTGTATGCAGCTTTGGGGAGACTGTACTGGGTATCTCAAACTCAACCAGCTTGGGCT
GGAGGGGGTAACGCCTACCCACCCCGTGCACCTCGCCCAAAAGTTCTGCTCCTTATCCTG
GGTATTGTGCTGACATTCTGGGCTTGTTTCCTTCCATTTTGGATCTGGCAGCTTCTACCG
TTGTACCAGCCTGAGGTTCTTCGTGTGGTGCCGGTTGGGACACAGGTGACCATAAATCGC
ATCCTCACAGGATTGACTTATGGAAACTCATGTGTGAATCCGTTCTTCTACACACTCCTG
ACAGGCAAGCGCAGAAGGACCAGCAGAAAGACAATAAGCGCAGCTGCGCCACTTTGCCAA
AAGGGCAGCTCTGAGCAATAA

MDIPGSTSLFSSPSPSYTFPFFTNLSFPSSSPSLSPSPSVASTALFCFFLSLLSLLGILG
NLYTLVLLLRRRRMSRRRHTAPMCCYSLSCLGSSSPSFSPSFSPSSSPTSSSSSSSLHLQ
VLSLALADLVYLSTAPFIVYDSLASDWAFGELGCRLLLSLDLLTMHASIFTLTAMSLDRY
RAVADPLATTSTPSSGLLRVALAWGFAIALSLPMMITLHLEDGENHEGKLCVPAWDEQSS
KAYLSILFCTSILGPGLAIGALYAALGRLYWVSQTQPAWAGGGNAYPPRAPRPKVLLLIL
GIVLTFWACFLPFWIWQLLPLYQPEVLRVVPVGTQVTINRILTGLTYGNSCVNPFFYTLL
TGKRRRTSRKTISAAAPLCQKGSSEQ
```

Figure 3.8. Generation of *uts2r3*^{b1436} mutants. The *uts2r3*^{b1436} allele was generated with a single-guide RNA which induced a deletion of 534 base pairs, resulting in an in-frame 178 amino acid deletion that removes around half the protein including transmembrane regions.

Discussion

Previously, SCOspondin had been shown to act downstream of cilia motility; immunofluorescence on fixed samples was used to demonstrate its assembly into the RF as a process occuring downstream of cilia motility (Cantaut-Belarif et al., 2018). Here, we were able to visualize this process live in wild-type and genetically perturbed embryos. First, *sspo-GFP* in the *cfap298*^{tm304} mutant background shows the failure of the RF to assemble in a system lacking cilia motility, and *sspo-GFP* in the *daw1*^{b1403} mutant background shows its formation upon delayed cilia motility initiation. These experiments also demonstrate potential physical interactions between cilia motility and the RF, as in some cases motile cilia appear to be brushing against the RF as it forms. Although SCOspondin is generally thought to be secreted from the subcommissural organ (Rodríguez et al., 1998), more recent evidence suggests that earlier in development, it is also secreted from the floor plate (Cantaut-Belarif et al., 2018; Troutwine et al., 2020). The precise mechanism for the ways in which cilia motility and fluid flow contribute to the formation of the fiber remains unclear, but some images in this study suggest that motile cilia themselves may release SCOspondin monomers, or physically guide free-floating monomers to the developing fiber.

It is also unknown whether the Reissner fiber must always be anchored at the rostral end of the central canal and form in the rostral-to-caudal direction, or if cilia motility were stronger at the caudal end it would form in the opposite direction. Mosaic mutants generated through CRSIPR or transplants to generate chimeras lacking motile cilia only in the rostral region could be used to further investigate this. Those same mutants could also be used to determine the extent to which cilia motility in some locations along the axis can make up for a lack of motility in others.

Urp1 and Urp2 peptides were first identified as playing a potential role in axis development by Zhang et. al. based on RNA sequencing of the cilia motility mutant *zmynd10* (Zhang et al., 2018). These peptides stood out as potentially responsive to fluid flows as urotensin II is a known vasoconstrictor in humans (Ross et al., 2010). Subsequent experiments using morpholinos to test the effects of urotensin peptides on developing zebrafish embryos seemed to suggest Urp1 and Urp2 were indeed a strong candidate factors downstream of cilia motility involved in straightening the body axis, as a significant proportion of morphants developed CTD (Zhang et al., 2018). However, this technique precluded investigations of adolescent and adult zebrafish, and left open the possibility of off-target morpholino-associated effects (Eisen & Smith, 2008).

We generated the *urp1*$^{\Delta P}$;*urp2*$^{\Delta P}$ double mutants to 1) confirm what the morphants had hinted, that Urp1 and Urp2 are needed for axial straightening and, 2) to test for roles beyond embryonic stages, something not possible with morpholinos. We used targeted mutagenesis to delete the coding sequence for both peptides, which could then be combined to create double mutants unable to produce either Urp1 or Urp2. When this technique produced doubly mutant embryos that were able to straighten as normal, it raised the question of why genetic mutants and morphants exhibited distinct phenotypes. Could genetic compensation be somehow "masking" the true phenotype in mutants (Rossi et al., 2015; Sztal & Stainier, 2020; El-Brolosy et. al., 2019)? In this mechanism, degraded strands of mRNA from mutated genes causes genes with similar sequences to be unregulated and perform the function of the mutated gene (El-Brolosy et al., 2019). However, RNA sequencing of the *urp1*$^{\Delta P}$;*urp2*$^{\Delta P}$ double mutants failed to reveal any clear candidate compensatory genes; no other Urotensin peptides were upregulated (Samuel Bertrand, personal communication).

Therefore, we interpret our results as showing that in fact Urp1 and Urp2 are dispensable for early axial straightening, and may reveal a pitfall of drawing conclusions based solely on morphant data. When using morpholinos, it is recommended to compare morphant phenotypes to existing mutants, use at least two different morpholinos per target gene (one of which targets a splice site), rescue with a co-injection of the target mRNA, and the use of a control morpholino not targeting the gene of interest (Eisen & Smith, 2008). While Zhang et. al. used multiple morpholino sequences to target Urp1 and Urp2, including splice site morpholinos, rescue experiments were not performed, nor was a control morpholino of any kind injected. Morpholino injection is also known to cause off-target effects in embryos (such as hydrocephalus or delayed development) that can confound analysis of true mutant phenotypes (Eisen & Smith, 2008; Stainier et al., 2017). The advent of CRISPR-Cas9 and the ability to genetically modify zebrafish in highly specific ways has recently allowed for the parsing of these mutant phenotypes from background and off-target effects (Stainier et al., 2017).

The lack of an axial straightening phenotype in our *urp1*$^{\Delta P}$;*urp2*$^{\Delta P}$ double mutants allowed homozygotes to be raised to adulthood. This revealed the previously unknown role of urotensins in long-term maintenance of spinal morphology, findings which were independently corroborated by Gaillard et. al (Gaillard et al., 2023). The development of scoliosis in these mutants mirrored that of adolescent idiopathic scoliosis in humans (Rolton et al., 2014; Shakil et al, 2014) becoming apparent during the adolescent rapid growth phase, without the presence of major deformities in the vertebrae (Bearce, Irons, O'Hara-Smith, et al., 2022). These curves are distinct from those seen in other cilia motility mutants, which occur in both the lateral and dorsal-ventral directions (Grimes et al., 2016). *urp1*$^{\Delta P}$;*urp2*$^{\Delta P}$ double mutants develop scoliosis only in the dorsal-ventral direction (Bearce, Irons, O'Hara-Smith, et al., 2022). These results suggest that urotensin peptides are specifically responsible for maintaining spinal linearity on the dorsal-ventral axis, while another mechanism, likely tied to cilia motility and the RF, is responsible for maintaining linearity in the lateral direction.

The urotensin receptor, *uts2r3*, is expressed in the dorsal muscle (Zhang et al., 2018), indicating this tissue may play a significant role in the development of scoliosis seen in *urp1*$^{\Delta P}$;*urp2*$^{\Delta P}$ double mutants. While urotensin peptides' precise path from their secretion by CSF-cNs in the central canal to their target receptor in the muscle is still unknown, our research supports a muscle-based mechanism as *uts2r3*^{b1436} mutants develop scoliosis very similar to that of the *urp1*$^{\Delta P}$;*urp2*$^{\Delta P}$ double mutants. In patients with adolescent idiopathic scoliosis, Dai et. al. found that urotensin receptors *UTS2, UTS2R*, and *UTS2D* were expressed at elevated levels in muscle tissue biopsied from the convex side of scoliotic spinal curves, when compared to tissue biopsied from the concave side. Additionally, some types of scoliosis are the secondary result of known muscular abnormalities, such as Duchenne Muscular Dystrophy (Archer et al., 2017; Janicki et al., 2007). Both these factors further support a muscle-based mechanism, perhaps one in which urotensins and their receptor act to enhance the development or integrity of the musculature surrounding the spine, such that in the absence of this mechanism the spine lacks the necessary support to remain straight during growth phases and as the individuals grow older.

Bridge to Chapter IV

This chapter investigates two factors downstream of cilia motility during the axial straightening process. First, live imaging of endogenously labeled SCOspondin in the central canal showed its failure to assemble in the absence of cilia motility, and its ability to assemble in the context of delayed cilia motility onset. Second, we investigated urotensin peptides Urp1 and Urp2, expressed in CSF-cNs and previously known to be downregulated in the absence of cilia motility. After generating doubly mutant embryos lacking the peptide coding sequence ($urp1^{\Delta P}$;$urp2^{\Delta P}$), we find that these peptides are dispensable for axial straightening, but upon raising these larvae to adulthood, Urp1 and Urp2 do play a role in long term spinal maintenance. In chapter IV, we investigate whether these peptides play a role in the *curly tail up* (CTU) phenotype, otherwise known as axial over-straightening, as well as other factors that may play a role in this phenotype that appears to act counter to CTD.

CHAPTER IV: PKD2 ACTS INDEPENDENTLY OF MOTILE CILIA AND FLUID FLOW TO PREVENT AXIS OVER-STRAIGHTENING

Introduction

In Chapter III, we described urotensins and their role in body axis straightening. Zhang et. al. had shown that the responsible genes, *urp1* and *urp2* were expressed in CSF-cN's (cerebrospinal fluid-contacting neurons) downstream of cilia motility, and proposed that they played a role in early body axis straightening (Zhang et al., 2018). This hypothesis was supported by morphants that developed the curved body axis, CTD, but contradicted by our *urp1*$^{\Delta P}$;*urp2*$^{\Delta P}$ double mutants, which exhibited normal axial straightening. Nevertheless, one result from the Zhang et al. study has remained compelling: when a high concentration of Urp1 peptide was injected into the central canal of zebrafish embryos, the excess peptide caused the body axis to curve dorsally (Zhang et al., 2018). This phenotype is reminiscent of one seen in other zebrafish mutants and is called curly tail up (CTU).

CTU occurs in zebrafish lacking the gene *pkd2* (Bisgrove et al., 2005; Sun et al., 2004; Schottenfeld et al., 2007). It encodes the zebrafish ortholog of the human gene *PKD2*, one of two genes responsible for causing the vast majority of autosomal dominant polycystic disease in humans (the other being *PKD1)* (Bycroft et al., 1999; Boucher & Sandford, 2004; Sharif-Naeini et al., 2009; Douguet et al., 2019). PKD2 contains six transmembrane domains and serves as a non-selective Ca^{2+} channel that physically interacts with PKD1, a membrane protein with a large extracellular domain (Su et al., 2018). In complex with PKD1 and localized to primary, or sensory, cilia, Pkd2 may act as part of a flow sensor by regulating changes in cytosolic Ca^{2+} (Koulen et al., 2002; Nauli et al., 2003; Nauli & Zhou, 2004; Sharif-Naeini et al., 2009). This function is especially well-established in the context of left-right patterning (Yoshiba et al., 2012; Grimes, Keynton, et al., 2016; Grimes & Burdine, 2017; Hamada, 2020; Djenoune et al., 2023). As such, *Pkd2* mutant mice display kidney malformations and laterality-associated cardiac defects (Wu et al., 2000).

The mechanism underlying laterality defects can be traced back to the breaking of left-right symmetry through fluid flow within the left-right organizer (Grimes, 2019b), as described in previous chapters. This pathway is dependent on Ca^{2+} signaling, with Pkd2 acting in sensory cilia to facilitate mechanosensation (Nauli et al., 2003; Nauli & Zhou, 2004; Yoshiba et al., 2012; Djenoune et al., 2023). In Kuppfer's vesicle (KV), the zebrafish left-right organizer, Pkd2 functions in complex with Pkd1l1, an ortholog of Pkd1 expressed specifically in KV (personal communication, Gabriel Luna-Arvizu). Zebrafish lacking Pkd1l1 exhibit left-right patterning defects as a result of a failure to activate the Nodal signaling cascade (Field et al., 2011; personal communication, Gabriel Luna-Arvizu).As such, zebrafish embryos lacking Pkd2 also develop left-right patterning defects (Bisgrove et al., 2005; Schottenfeld et al., 2007).

However, in many ways their most striking phenotype is the one for which these mutants were originally named, curly tail up. Seemingly the opposite phenotype to curly tail down, we hypothesized this over-straightening phenotype could be based in the same cilia-motility and fluid flow-based body axis straightening pathway investigated in previous chapters. Interspersed among the ependymal cells that line the central canal are specialized neurons called cerebrospinal fluid-contacting neurons (CSF-cNs) (Djenoune et al., 2014). Also known as KA cells in zebrafish (Dale et al., 1987), these GABAergic neurons extend microvilli into cerebrospinal fluid (CSF). These cells express *pkd2l1,* another calcium ion channel in the polycystin family known in this context to be required for the mechanoception of cerebrospinal fluid flow. Mutants lacking Pkd2l1 do not develop CTU, but may develop subtle spinal curvatures in adulthood (Sternberg et al., 2018; Chapter III). These factors all implicate a sensory role for CSF-cNs, but their exact function remains poorly understood (Djenoune et al., 2014; Orts-Del'Immagine et al., 2014).

Given then, Zhang et. al.'s result in which an excess of Urp1 peptide in the central canal induces CTU, we propose a model in which *pkd2* modulates the expression or secretion of Urotensin-like peptides in response to a flow signal induced by cerebrospinal fluid flow in the central canal. Loss of *pkd2* therefore leads to derepression of Urp1 and Urp2, causing over-activation of the body axis straightening pathway.

Results

Zebrafish embryos develop curly tail up in the absence of Pkd2 or Pkd1 and Pkd1b

To examine the effects of loss of Pkd2, we used CRISPR-Cas9 to generate three loss of function mutants, referred to as *pkd2*^{b1402}*, pkd2*^{b1419}, and *pkd2*^{b1437} (Figure 4.1A-D). All contain frameshift mutations that produce early stop codons, most likely resulting in mRNA degradation or a truncated protein. *pkd2*^{b1402} contains a 7 bp mutation in exon 1, *pkd2*^{b1419} a 5 bp deletion in exon 10, and *pkd2*^{b1437} a 2 bp deletion in exon 13 (Figure 4.1B-D). All three mutants exhibited the same body axis defect, CTU, seen in morphants (Figure 4.1E). Since *pkd2*^{b1402} contained the earliest stop codon, it was used for all further experiments.

In other contexts, such as in the left-right organizer, Pkd2 acts in complex with Pkd1l1 to sense fluid flow signals transmitted by motile cilia and fluid flow (personal communication, Gabriel Luna-Arvizu). Accordingly, *pkd2* mutants and *pkd2* morphants exhibit randomized heart jogging, indicative of left-right patterning defects (Schottenfeld et al., 2007; Field et al., 2011; Figure 4.2D). However, while *pkd2* is expressed broadly throughout the embryo (England et al., 2017), *pkd1l1* is expressed only in the left-right organizer (Gabriel Luna-Arvizu, personal communication) and is therefore unlikely to act in a body axis straightening pathway. Supporting this, embryos lacking *pkd1l1* do not develop CTU (Gabriel Luna-Arvizu, personal communication). However, *pkd1* and *pkd1b*, both paralogs of *pkd1l1*, are expressed in tissues along the body axis, including the notochord, which may be relevant for axial straightening (Mangos et al., 2010). This led me to hypothesize that Pkd1 and Pkd1b might partner with Pkd2 in the context of axial straightening.

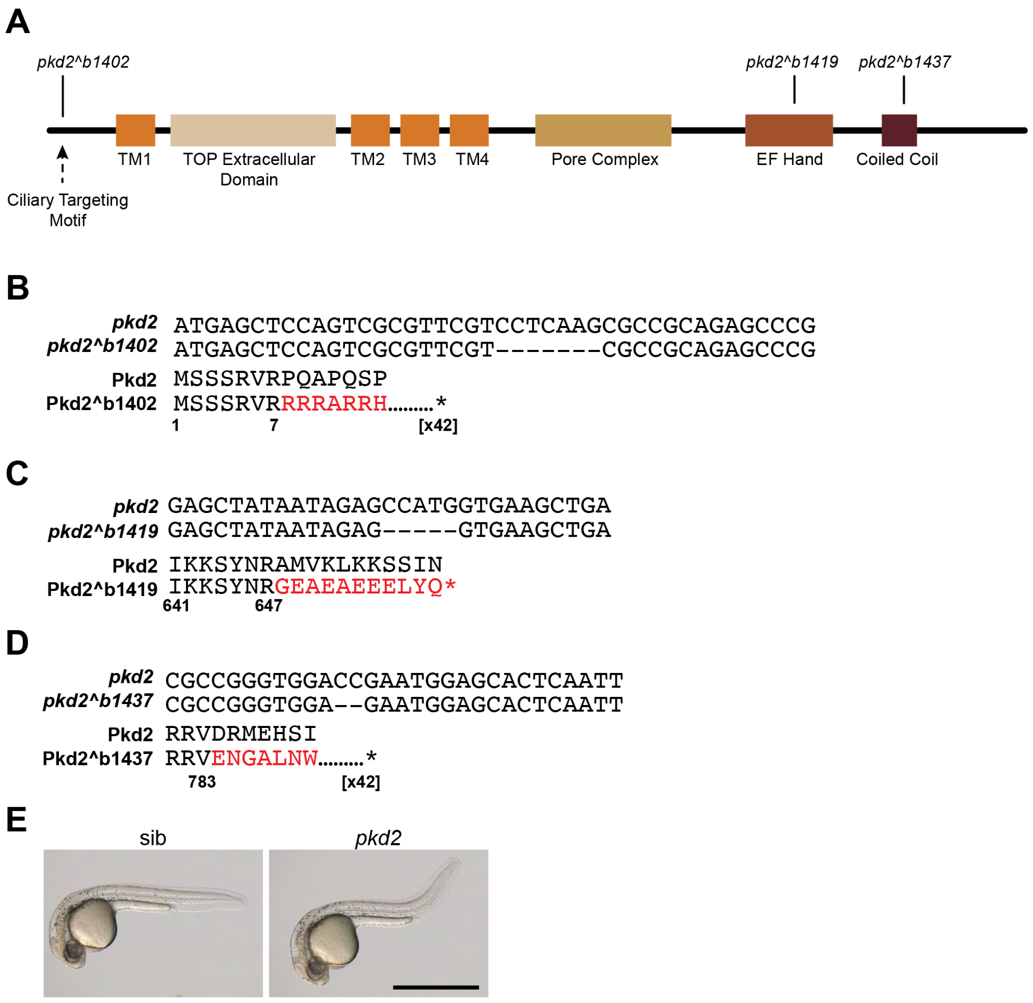
A
pkd2^b1402
pkd2^b1419
pkd2^b1437
TM1
TOP Extracellular Domain
TM2
TM3
TM4
Pore Complex
EF Hand
Coiled Coil
Ciliary Targeting Motif
B
pkd2 ATGAGCTCCAGTCGCGTTCGTCCTCAAGCGCCGCAGAGCCCG
pkd2^b1402 ATGAGCTCCAGTCGCGTTCGT-------CGCCGCAGAGCCCG
Pkd2 MSSSRVRPQAPQSP
Pkd2^b1402 MSSSRVRRRRARRH.........*
1
7
[x42]
C
pkd2 GAGCTATAATAGAGCCATGGTGAAGCTGA
pkd2^b1419 GAGCTATAATAGAG-----GTGAAGCTGA
Pkd2 IKKSYNRAMVKLKKSSIN
Pkd2^b1419 IKKSYNRGEAEAEEELYQ*
641
647
D
pkd2 CGCCGGGTGGACCGAATGGAGCACTCAATT
pkd2^b1437 CGCCGGGTGGA--GAATGGAGCACTCAATT
Pkd2 RRVDRMEHSI
Pkd2^b1437 RRVENGALNW.........*
783
[x42]
E
sib
pkd2

Figure 4.1. Zebrafish embryos lacking *pkd2* develop curly tail up by 28 hpf. (A) Domain architecture of Pkd2 and location of three alleles generated: b1402 near the ciliary targeting motif, b1419 in the EF hand, and b1437 in the coiled coil. (B) *pkd2*^{b1402} contains a 7 bp deletion, resulting in a frameshift after residue 7, leading in an early stop codon after 42 nonsense residues. (C) *pkd2*^{b1419} contains a 5 bp deletion, resulting in a frameshift mutation after residue 647 and an early stop codon after 11 nonsense residues. (D) *pkd2*^{b1437} contains a 2 bp deletion and frameshift mutation after residue 783, resulting in an early stop codon after 42 nonsense residues.(E) All mutants lacking *pkd2* develop CTU by 28 hpf. Scale bar: 1 mm

To test this, we generated mutant lines with early stop codons in *pkd1* and *pkd1b* (called *pkd1*^{b1428} and *pkd1b*^{b1442}, Figure 4.2A-B), then bred the two lines together to create doubly homozygous mutants. *pkd1*^{b1428} mutants exhibited craniofacial defects and developed severe edemas by 5 dpf, while *pkd1b*^{b1442} mutants displayed no apparent gross morphological defects (Figure 4.2C), and were homozygous viable and fertile (not shown). Doubly homozygous mutants, referred to as *pkd1*^{b1428}*;pkd1b*^{b1442}, developed CTU by 28 hpf (Figure 4.2C). Unlike *pkd1l1* mutants, neither the double nor the single *pkd1* mutants exhibited abnormal heart jogging (Figure 4.2D), demonstrating their effects as independent of the left-right patterning pathway.

To compare the development of CTU in *pkd2*^{b1402} and *pkd1*^{b1428}*;pkd1b*^{b1442} mutants, we live imaged zebrafish embryos during their first 48 hours of development (Movie 21**)**. Embryos were injected with α-bungarotoxin mRNA at the one-cell stage, causing complete motor paralysis but allowing for normal development (Swinburne et al., 2015). Embryos were mounted around 12 hpf, then imaged every 10 minutes for 48 hours in a temperature-controlled room. Body angles were quantified every hour starting at 22 hpf, as described previously (Figure 4.2E). In *pkd2*^{b1402} mutant embryos, this revealed a departure from the normal straightening process at 28 hpf, at which time the embryo body axis continued to move dorsally even after imaging was completed (Figure 4.2E, Movie 21). In *pkd1*^{b1428}*;pkd1b*^{b1442} mutant embryos, quantification revealed a departure from the normal straightening process even earlier, around 25hpf, at which point straightening appears to accelerate (Figure 4.2E, Movie 21). These results demonstrate that *pkd1*^{b1428}*;pkd1b*^{b1442} double mutants closely, though not exactly, phenocopy *pkd2*^{b1402} mutants, supporting the possibility that Pkd1-Pkd2 and Pkd1b-Pkd2 complexes might be functional units involved in axial straightening.

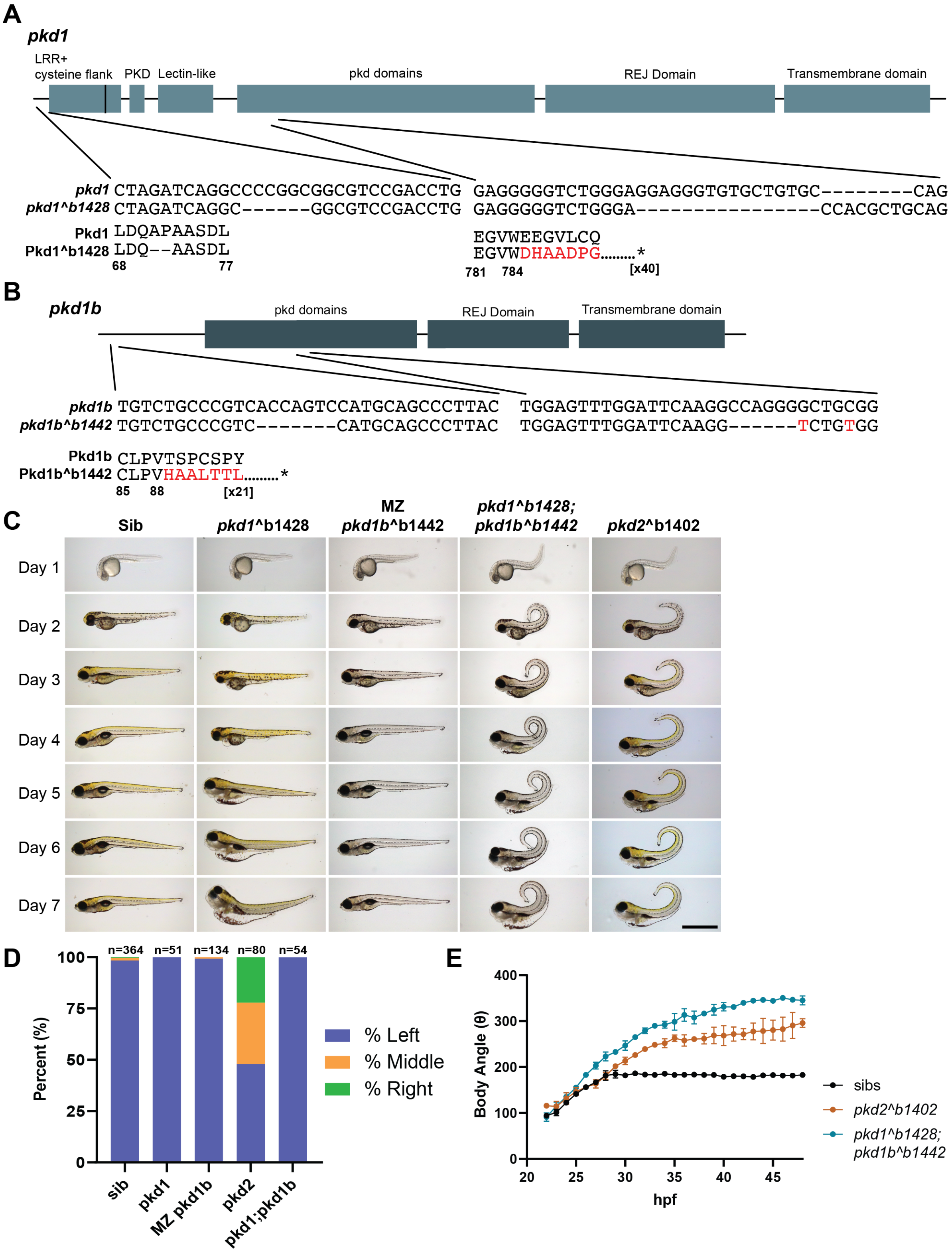

Figure 4.2. ***pkd1*^{b1428}*;pkd1b*^{b1442} mutants develop CTU without left-right patterning defects.** (A) Domain architecture of Pkd1. The b1428 allele contains two separate deletions ultimately resulting in a frameshift after residue 784 and an early stop codon after 40 nonsense residues. (B)

Domain architecture of Pkd1b. The b1442 allele contains two separate deletions, the first one resulting in an early stop codon after residue 88 and 21 nonsense residues. (C) Development of *pkd2*^{b1402}, *pkd1*^{b1428}, and *pkd1b*^{b1442} single mutants alongside *pkd1*^{b1428}*;pkd1b*^{b1442} double mutants over 5 days post fertilization. Only *pkd2*^{b1402} and *pkd1*^{b1428}*;pkd1b*^{b1442} double mutants develop CTU, although *pkd1*^{b1428} single mutants develop severe edemas by 5 dpf. Scale bar: 1 mm (D) Heart jogging quantified across multiple clutches of *pkd2*^{b1402}, *pkd1*^{b1428}, and *pkd1b*^{b1442} single mutants alongside *pkd1*^{b1428}*;pkd1b*^{b1442} double mutants. Only *pkd2*^{b1402} clutches display randomized heart laterality. (E) Average body angle (n=2) of *pkd2*^{b1402} mutants and *pkd1*^{b1428}*;pkd1b*^{b1442} double mutants over the first 48 hpf, measured every hour.

Curly tail up occurs independently of Urp1 and Urp2

Previous work showed that Urp1, expressed downstream of cilia motility in the central canal, caused CTU when injected at high concentrations directly into the canal (Zhang et al., 2018). We therefore hypothesized that loss of repression of *urp1* and *urp2* could be responsible for CTU in *pkd2* and *pkd1;pkd1b* mutants. However, bulk RNA sequencing of *pkd2* mutants revealed expression of *urp1* and *urp2* were not significantly changed (Sophia Frantz, personal communication). Because this does not rule out post-translational upregulation, we also used the previously described *urp1*$^{\Delta P}$;*urp2*$^{\Delta P}$ double mutants to determine whether genetically removing Urp1 and Urp2 would prevent CTU in *pkd2* mutants. For this experiment, we injected a high concentration of 4 multiplexed guides against *pkd2* along with Cas9 enzyme into embryo yolks at the single-cell stage. This generated *pkd2* crispants, which closely phenocopied mutants, producing CTU in close to 100% of cases. Control embryos *urp1*$^{\Delta P}$;*urp2*$^{\Delta P}$ double heterozygotes injected with *pkd2* gRNAs, developed CTU, phenocopying the mutant phenotype. Similarly, doubly *urp1*$^{\Delta P}$;*urp2*$^{\Delta P}$ homozygous embryos in which *pkd2* was targeted also developed CTU, demonstrating that CTU can occur in the absence of urotensin peptides (Figure 4.3A).

Pkd2 functions downstream of cilia motility or in a parallel pathway

To genetically directly test whether *pkd2* acts downstream of cilia motility in body axis straightening, we used epistasis tests between mutants lacking genes in the cilia motility/fluid flow body axis straightening pathway and *pkd2*. For rapid analysis of several mutant combinations, we used crispants (i.e. embryos injected with guide RNAs and Cas9) (Wu et al., 2018) after confirming that crispants for *pkd2*, *cfap298*, and *sspo* all phenocopied germline mutants (Figure 4.3B). Embryos injected with guides against *pkd2* and *cfap298*, or *pkd2* and *sspo* still developed CTU overall, although the more anterior part of the body curled down slightly around the yolk, creating an intermediate phenotype between CTU and CTD (Figure 4.3B). To further confirm this result using germline mutants, we also generated mutants doubly homozygous for *pkd2*^{b1402} and either *cfap298*^{tm304} or *sspo*^{b1446}. *cfap298*^{tm304} mutants lack cilia motility and therefore fluid flow in the central canal (Jaffe et al., 2016) and *sspo*^{b1446} mutants lack the main component of the RF, which forms directly downstream of cilia motility as described in Chapters II and III. To evaluate mutant phenotypes, we performed dihybrid crosses of adult fish doubly heterozygous for each gene, and then sorted phenotypes among large clutches to determine the presence of a 9:3:3:1 ratio; the intermediate phenotype appeared at the lowest rate. Based on the presence of the phenotype at this ratio, with 1/16 developing the intermediate phenotype seen in the double crispants, it is likely that these embryos were doubly homozygous for *pkd2*^{b1402} and either *cfap298*^{tm304} or *sspo*^{b1446} (Figure 4.3C-D).

These results taken together showed that CTU can occur in the absence of cilia motility or the RF. This coheres with a model in which Pkd2 functions downstream (or in a parallel pathway) compared with the cilia-RF pathway. In agreement, we imaged cilia and *sspo-GFP* in the central canal at 28 hpf and found that cilia motility and the RF were both unaffected in *pkd2*^{b1402} mutants (Movies 22 and 23**)**. Overall, this suggests that *pkd2* is likely to act in a body axis straightening pathway independently of cilia motility.

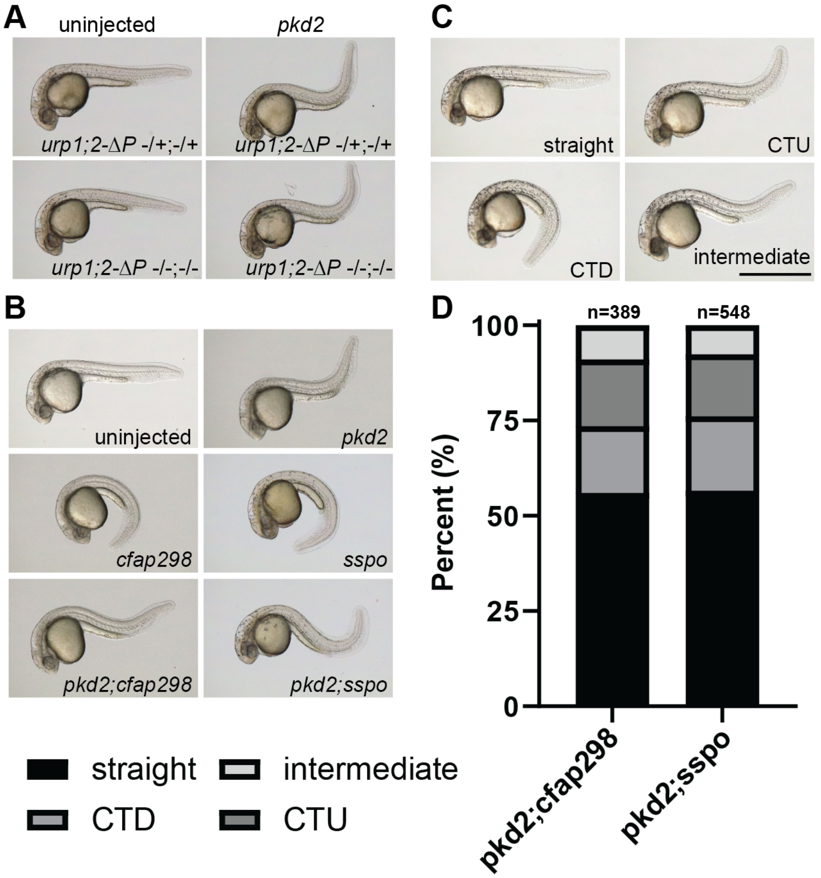

Figure 4.3. ***pkd2*** **mutants develop CTU in the absence of cilia motility and the Reissner fiber.** (A) *urp1*$^{\Delta P}$*;urp2*$^{\Delta P}$ mutants injected with Cas9 enzyme and gRNAs against *pkd2* develop CTU, suggesting Urotensin-like peptides are not upstream of CTU. (B) Embryos double injected with Cas9 and gRNAs against *pkd2, cfap298,* and *sspo*, as well as *pkd2* with *cfap298* or *sspo.* Doubly injected embryos develop an intermediate phenotype: CTU, with a slight downward curvature at the anterior portion of the body axis. (C) 4 phenotypes seen in dihybrid crosses between fish doubly heterozygous for *pkd2*^{b1402} and *cfap298*^{tm304} or *sspo*^{b1446} (scale bar: 1 mm). These were counted across two clutches per cross (D), appearing in a 9:3:3:1 ratio.

Investigating a notochord-specific role of Pkd2 in axial straightening

Previous work showed that *pkd2* morphants had increased collagen deposition around the notochord (Mangos et al., 2010; Le Corre et al., 2014). Since we ruled out a role for Pkd2 in the cilia-RF-Urp pathway, we next considered that Pkd2 might exert its influence on axial straightening through a notochord-dependent pathway. To test the possibility that collagen could be a component of the CTU phenotype, we repeated the crispant experiment targeting *pkd2* and, this time, the notochord-specific collagen *col2a1a*. While *pkd2* crispants developed CTU, *pkd2;col2a1a* double crispants did not develop CTU when assessed at 1 dpf, indicating that CTU cannot occur in the absence of this notochord-specific collagen (Figure 4.4A). Instead, *col2a1a* and *pkd2;col2a1a* crispants exhibited a weak curly tail down phenotype (Figure 4.4A). This lends support to our hypothesis that *pkd2* prevents axis over-straightening through a cilia-independent mechanism based in the notochord.

To test this hypothesis directly, and define the potential role of notochord-specific Pkd2 in axial straightening, we generated transgenic lines to knock out *pkd2* specifically in notochord cells. Transgenics expressed Cas9-GFP behind the *rcn3* promoter, which is in turn expressed in the inner vacuolated and outer sheath cells of the notochord (Ellis et al., 2013) i.e. a pan-notochord genetic promoter. We also engineered our transgenic construct to express two guide RNAs targeting *pkd2* under ubiquitous U6 promoters. These two guide RNAs corresponded those used in the crispant injections, and so have been previously validated. This transgenic construct (Figure 4.4B) was injected along with *transposase* mRNA into fertilized zebrafish embryos at the one-cell stage. At every generation, individuals were screened for expression of the transgenic marker in the heart (*cmlc*:GFP) as well as Cas9-GFP expression in the notochord.

After establishing transgenic lines to at least the F_2 stage, we assessed for potential phenotypes. Individual embryos expressing Cas9-GFP in the notochord did not develop CTU (Figure 4.4C-D). To check that mutations were made in *pkd2* in these transgenic lines, we performed T7 Endonuclease assays on F_2 embryos expressing GFP in the notochord, compared to GFP- individuals from the same cross. These assays showed that while no mutations were made at the site targeted by guide RNA 1, multiple insertion mutations were made at the second target site, which are likely to be deleterious (Figure 4.4E-F). While these results call into question the requirement of *pkd2* in the notochord for a straight body axis, we cannot rule out that mutagenesis was simply insufficient to reveal such a potential role. As such, we consider these findings preliminary and, so far, it is challenging to make a final conclusion about whether Pkd2 functions in the notochord during axial straightening or not.

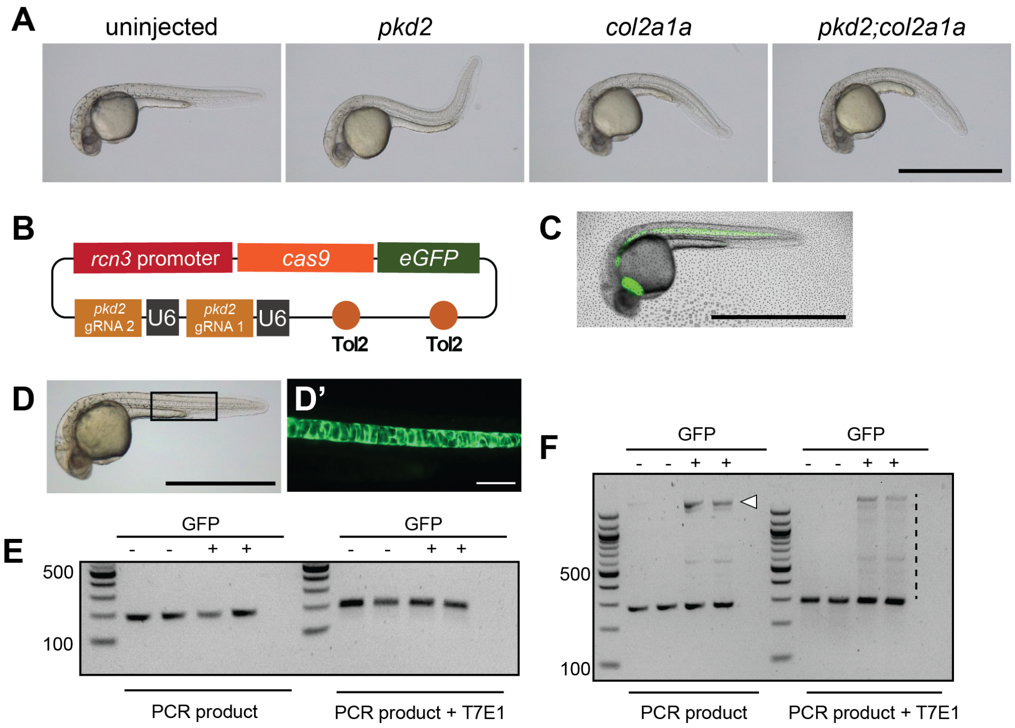
A
uninjected
pkd2
col2a1a
pkd2;col2a1a
B
rcn3 promoter
cas9
eGFP
pkd2 gRNA 2
U6
pkd2 gRNA 1
U6
Tol2
Tol2
C
D
D'
E
GFP
- - + +
GFP
- - + +
500
100
PCR product
PCR product + T7E1
F
GFP
- - + +
GFP
- - + +
500
100
PCR product
PCR product + T7E1

Figure 4.4. *pkd2* is not necessary in the notochord to prevent CTU. (A) Crispants doubly injected with gRNAs against *pkd2* and *col9a2* do not develop CTU at 28 hpf. Scale bar: 1mm (B)

Construct injected into embryos at the single-cell stage to mutate *pkd2* specifically in the notochord by expressing Cas9 behind the *rcn3* promoter (Ellis et al., 2013). (C) Cas9-GFP can be seen in F_2 individuals. Scale bar: 1mm (D) Transgenic embryos do not develop CTU (scale bar: 1 mm), despite the presence of Cas9-GFP in the notochord (D', scale bar: 100µM). (E-F) T7E1 assays show no mutagenesis at the first site targeted, but significant insertions at the second (white arrow head). (F) Significant digestion of PCR product was found in GFP-positive embryos digested with T7 endonuclease (dashed line).

Assessing the role of the Pkd2 ciliary localization motif in development

The trafficking of Pkd2 to the primary cilium is thought to play a crucial role in its function (Walker et al., 2019). In cilia, Pkd2 is proposed to function as a force-responsive cation channel. Indeed, one proposed mechanism for ADPKD in humans involves the failure of PKD1 or PKD2 to properly traffic to the ciliary membrane. Therefore, we hypothesized that the highly conserved cilia localization motif (CLM), characterized by the residues RVXP, located near the N-terminus of the gene product and previously identified through mutation scanning and overexpression in cell lines (Geng et al., 2005; Bae et al., 2006; Knobel et al., 2008), would also crucial for the trafficking of zebrafish Pkd2 to cilia. By mutating the CLM, we aimed to test the role of ciliary-localized Pkd2 in developmental phenotypes, in contrast to Pkd2's other main site of function, the endoplasmic reticulum membrane.

To test this, we generated two lines with mutations near the CLM, *pkd2*^{b1472} and *pkd2*^{b1473} (Figure 4.5A-B). However, in both cases, embryos developed normally (Figure 4.5C), meaning these alleles did not significantly impact the CLM, or the localization of Pkd2 to cilia is not necessary for the prevention of CTU. For this experiment, we were relying on guide RNAs very close to the CLM causing a disruption but, unfortunately, mutations that were isolated disrupted amino acid sequences just downstream of the minimally defined CLM. Future experiments should use homologous recombination techniques to generate mutants with precise changes the the CLM, in order to test its necessity in developmental events.

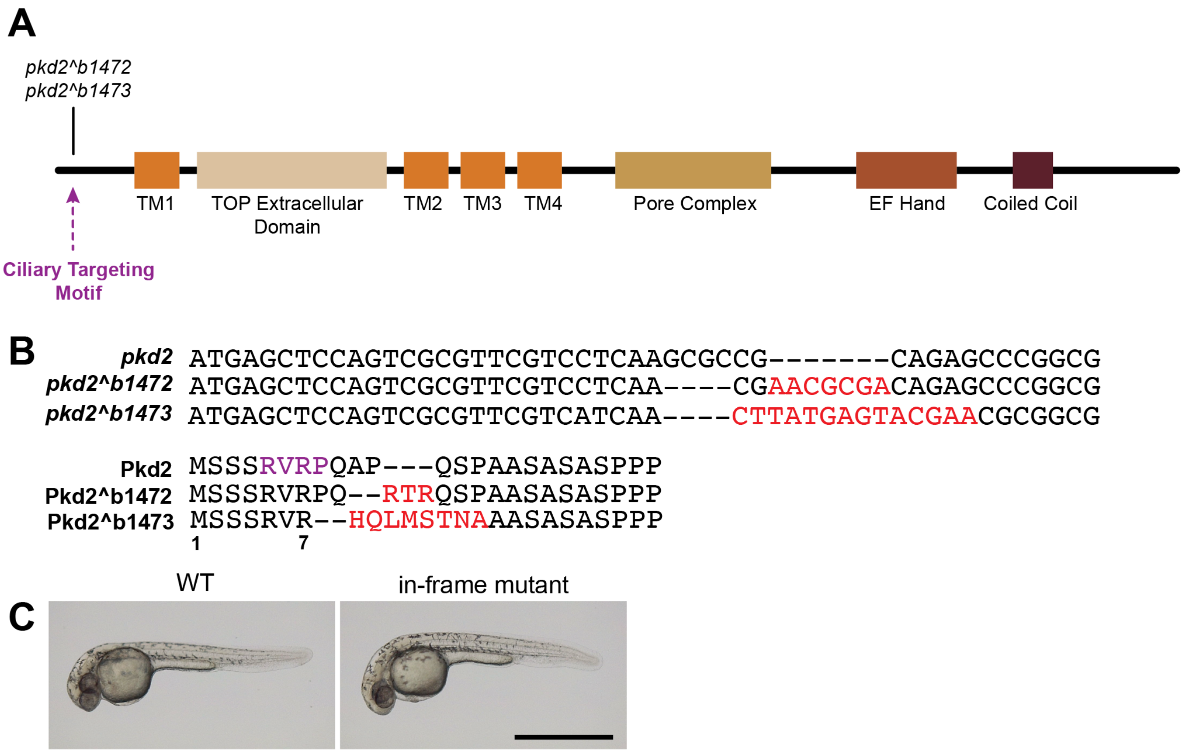
A
pkd2^b1472
pkd2^b1473
TM1
TOP Extracellular Domain
TM2
TM3
TM4
Pore Complex
EF Hand
Coiled Coil
Ciliary Targeting Motif
B
pkd2 ATGAGCTCCAGTCGCGTTCGTCCTCAAGCGCCG-------CAGAGCCCGGCG
pkd2^b1472 ATGAGCTCCAGTCGCGTTCGTCCTCAA----CGAACGCGACAGAGCCCGGCG
pkd2^b1473 ATGAGCTCCAGTCGCGTTCGTCATCAA----CTTATGAGTACGAACGCGGCG
Pkd2 MSSSRVRPQAP---QSPAASASASPPP
Pkd2^b1472 MSSSRVRPQ--RTRQSPAASASASPPP
Pkd2^b1473 MSSSRVR--HQLMSTNAAASASASPPP
1
7
C
WT
in-frame mutant

Figure 4.5. Mutations in *pkd2* near the ciliary targeting motif do not cause CTU. (A) Domain architecture of Pkd2 and location of two in-frame alleles in the vicinity of the ciliary targeting motif. (B) *pkd2* mutant alleles b1472 and b1473 contain small indel mutations that result in in-frame deletions just after the ciliary targeting motif. (C) Neither $pkd2^{b1472}$ nor $pkd2^{b1473}$ develop CTU (Scale bar: 1mm).

Discussion

Because CTU appears upon initial observation to be the “opposite” phenotype of CTD, it is reasonable to hypothesize that it might caused by over-activation of the same pathway, known to be dependent on cilia motility, fluid flow, the RF and Urotensin peptides (Grimes, 2019a;

Cantaut-Belarif et al., 2018; Zhang et al., 2018; Bearce, Irons, Craig et al., 2022; Bearce, Irons, O'Hara-Smith et al., 2022). The involvement of Pkd2 in this pathway was supported by evidence that it acts as a flow sensor in other contexts, such as in cell culture, in the left-right organizer in complex with Pkd1l1 (Koulen et al., 2002; Nauli et al., 2003; Nauli & Zhou, 2004; Sharif-Naeini et al., 2009; Schottenfeld et al., 2007; Gabriel Luna-Arvizu, personal communication), and potentially in the kidney in complex with Pkd1. Additionally, urotensin peptides, known to be expressed downstream of cilia motility (Zhang et al., 2018; Bearce, Irons, O'Hara-Smith et al., 2022), cause CTU when injected into the central canal at high concentrations, supporting that their overactivation might be a cause of CTU. However, the epistasis tests done here eliminating *pkd2* in combinations with cilia motility (*cfap298*), the Reissner fiber (*sspo*), and urotensin peptides (*urp1;urp2*), all demonstrated that *pkd2* is likely to act in a pathway independent of the cilia-RF-Urotensin pathway. Mutants lacking *pkd2* and components of the axial straightening pathway developed intermediate phenotypes; such mixing of phenotypes in an epistasis test is usually indicative of the involvement of distinct pathways. This novel result opens up many new avenues of investigation with respect to *pdk2*, particularly in regards to what other tissues could be involved in counteracting the cilia motility pathway that straightens the body axis.

Expression of Pkd2's proposed binding partners, Pkd1 and Pkd1b, in the notochord and surrounding tissues (Mangos et al., 2010) would suggest that the notochord, also the structural center of the body axis, as a tissue for Pkd2's mechanism of action. To test this, we generated a transgenic zebrafish line designed to mutate *pkd2* in notochord cells specifically (Ablain et al., 2015). However these embryos did not develop CTU, despite evidence of mutations made at a targeted locus. These preliminary results contradict the hypothesis that *pkd2* acts in the notochord to prevent the development of CTU, but do not completely rule out the possibility. For example, it is possible that the level of Cas9 expression in the F_2 individuals evaluated was too low to generate enough mutations to produce a phenotype. In addition, sequencing of GFP-positive cells would be able to definitively show the extent which these mutations may have affected the Pkd2 protein. However, it also remains possible that the initial results indicate correctly that *pkd2* is not essential in the notochord for correct body axis straightening.

If this is the case, other tissues would be implicated. These include tissues implicated by the expression of *pkd1* and *pkd1b* such as the floor plate and neural tube (Mangos et al., 2010). Our results here also call into question Pkd2's requirement in cilia themselves. In-frame deletion mutants $pkd2^{b1472}$ and $pkd2^{b1473}$ do not develop CTU. Whether Pkd2 also retains its function with respect to left-right patterning could be further evaluated in future studies, by analyzing these mutants for left-right patterning defects. Although it is possible that the $pkd2^{b1472}$ and $pkd2^{b1473}$ alleles do not sufficiently affect the CLM to cause aberrant trafficking, if Pkd2's role in body axis straightening is indeed independent of cilia entirely, that further opens up the possibility of the involvement of other tissues not normally thought to be associated with cilia (motile or sensory) or cilia-dependent processes. Pkd2 is most well-known as a calcium channel (Koulen et al., 2002; Nauli et al., 2003; Nauli & Zhou, 2004; Sharif-Naeini et al., 2009), and as such has the potential to act in numerous signaling pathways (Clapham, 1995; Kass & Orrenius, 1999; Puri, 2020).

CHAPTER V: CONCLUDING REMARKS

The establishment of the zebrafish body axis is a deceptively complex system that can inform our understanding of cilia motility and fluid flow signaling pathways, left-right patterning, and the development of adolescent idiopathic scoliosis (Grimes, 2019a). In this work, I investigated multiple aspects of this process: the role of timing of onset of cilia motility (Chapter II), factors potentially downstream of fluid flow signaling (Chapter III), and mechanisms that may prevent axis over-straightening (Chapter IV). I first showed that *daw1* regulates timing of cilia motility onset, and that the zebrafish body axis can straighten in a delayed fashion for three days post fertilization before the overall shape becomes set. Next, I demonstrated that the Reissner fiber is assembled downstream of cilia motility, even when motility is delayed, and is assembled in a rostral-caudal direction. However, Urotensin-like peptides, while expressed downstream of cilia motility (Zhang et al., 2018), are not required for axis straightening. Instead, they play a role in the maintenance of spinal straightness during later growth stages. Third, I showed that *pkd2* plays a role in preventing axis over-straightening through a cilia motility- and fluid flow-independent pathway.

Zebrafish embryos homozygous for the *daw1*^{b1403} mutant allele straighten in a delayed fashion. We found that this is most likely a result of delayed onset of cilia motility, and our investigation suggests that *daw1* is responsible for timely activation of motility (Bearce, Irons, Craig, et al., 2022). This means that while *daw1*^{b1403} mutants initially develop curly tail down (CTD), a severe and oftentimes lethal deformity (Brand et al., 1996), they are able to remodel their body axes in response to the delayed cue, hours after the straightening process would normally have occurred. This way, most embryos are able to achieve straight body axes by 5 dpf.

Using the temperature sensitive mutant *cfap298*^{tm304}, we were able to further show that in fact the zebrafish body axis is able to remodel itself and recover from CTD as late as three days post fertilization with enough time for embryos to become viable and grow into adults (Bearce, Irons, Craig, et al., 2022). This demonstrates a remarkable ability of the body axis to both receive and respond to a delayed signal, and speaks to flexibility within the timing of this developmental pathway as well as ability of the embryo to recover from adverse conditions. These results also helped explain the unusual combination of symptoms experienced by patients with *DAWI* mutations (Leslie et al., 2022). Like zebrafish, in humans *DAW1* appears most critical for cilia motility at very early stages of development, but less critical for cilia motility at later stages.

Our investigation into *daw1* and cilia motility in the central canal prompted us to examine factors that could be downstream of this flow-based signaling pathway. By combining *daw1*^{b1403} zebrafish with those expressing Sspo-GFP, in which the SCOspondin protein is endogenously labeled with a fluorophore (Troutwine et al., 2020), we were able to show that delayed motility in *daw1*^{b1403} mutants also results in delayed formation of the Reissner fiber, previously known to play a role in axial straightening (Cantaut-Belarif et al., 2018).

To test another factor downstream of cilia motility, we examined the urotensin-like peptides Urp1 and Urp2, generating a double mutant lacking coding sequences for both peptides, called *urp1*$^{\Delta P}$*;urp2*$^{\Delta P}$. Surprisingly, these mutants were able to straighten normally, contrasting previously published morphant data (Zhang et al., 2018). These differential effects seen between techniques reveal the pitfalls of drawing conclusions using morpholinos without proper controls (Eisen & Smith, 2008; Stainier et al., 2017). However, because *urp1*$^{\Delta P}$*;urp2*$^{\Delta P}$ mutants did not develop CTD, we were able to examine the role of Urp1 and Urp2 in adult fish, finding that they are in fact required for maintaining spinal straightness. *urp1*$^{\Delta P}$;*urp2*$^{\Delta P}$ mutants developed spinal curves only in the dorsal-ventral direction, unique to those of the cilia motility mutant *cfap298*^{tm304} (Grimes et al., 2016; Bearce, Irons, O'Hara-Smith, 2022). This suggests that a cilia motility- and Reissner fiber-based mechanism might be responsible for maintaining linearity in the lateral direction, while Urotensin-like peptides are responsible for maintaining linearity in the dorsal-ventral direction.

Similarly, the mechanism to prevent axis over-straightening during early development may not be cilia motility-dependent. Curly tail up (CTU) was first identified by Brand et. al. in 1996 (Brand et al., 1996), and later revealed to be caused by loss of the gene *pkd2* (Schottenfeld et al., 2007), which also plays a role in proper left-right patterning. In humans, *PKD2* is one of two main genes (the other bing *PKD1*) known to cause autosomal dominant polycystic kidney disease (Bycroft, 1999). The zebrafish genome contains two orthologs of *PKD1*, *pkd1* and *pkd1b*. In morphants, knockdown of these in the same embryo has been shown to cause CTU like that seen in *pkd2* mutants (Schottenfeld et al., 2007; Mangos et al., 2010). For this study, I generated zebrafish embryos lacking *pkd1* and *pkd1b*, which phenocopied the morphant, developing CTU by 28 dpf. Because Pkd2 was known to act in complex with Pkd1l1 downstream of flow to effect left-right patterning (Field et al., 2011), I hypothesized that Pkd2 could similarly be acting downstream of flow in the central canal in complex with Pkd1 and Pkd1b. To test this, I used two different methods to generate mutants lacking both *pkd2* and either *cfap298* or *sspo*. First, I used CRISPR/Cas9 to generate mosaic crispants with guide RNA's targeting both *pkd2* and *cfap298* or *sspo*. Then, I used dihybrid crosses of mutant fish doubly heterozygous for *pkd2*^{b1402} and *cfap298*^{tm304} or *pkd2*^{b1402} and *sspo*^{b1446}, then examined clutches for a phenotype that appeared in

1/16 of embryos. Both types of double mutants still developed CTU, although with a slight curl down in the initial part of the body axis. This suggests that *pkd2* is in fact acting in a separate, cilia-independent pathway to straighten the body axis, although cilia motility may still be essential for uncurling the most anterior portion of the body axis from around the yolk. Because the notochord is the structural center of the body axis (Bagnat & Gray, 2020), I hypothesized that *pkd2*, *pkd1*, and *pkd1b*, may be acting in this tissue to counteract the force generated during body axis straightening. To test this, I generated transgenic zebrafish embryos that would express Cas9-GFP specifically in the notochord cells as well as two universally expressed guide RNA sequences targeting *pkd2*. Despite evidence of mutations, these embryos did not develop CTU, suggesting *pkd2* is not required in the notochord to counteract body axis straightening. However, these results open up exciting new questions for the field, as *pkd2*, *pkd1*, and *pkd1b* are expressed in a wide variety of tissues throughout development (Mangos et al., 2010), and the notochord is far from the only tissue at play in the straightening process. Additionally, these results highlight the complexity of spinal development and the straightening process, which necessarily involves nearly every type of tissue in the body, from connective tissue, to nerves, muscle and bone.

APPENDIX A: MATERIALS AND METHODS

Zebrafish

Zebrafish (Danio rerio) of the AB, TU, and WIK strains were used. Embryos from natural matings were incubated at 28°C unless otherwise stated. Zebrafish mutant lines used are listed in Table 1. Experiments were undertaken in accordance with research guidelines of the International Association for Assessment and Accreditation of Laboratory Animal Care and approved by the University of Oregon Institutional Animal Care and Use Committee.

Mutant generation

Cas9 mRNA was generated by in vitro RNA synthesis using pCS2-nCas9n (Addgene #47929; Jao et al., 2013) as a template. All mutagenesis oligo were designed using CRISPRscan (Moreno-Mateos et al., 2015)and obtained from Integrated DNA Technologies (IDT). Full gRNA templates were assembled by annealing and extension with bottom strand oligo 1 (Table 2) using Taq Polymerase (New England Biolabs, M0273) and cycling parameters of 95°C (3 min), 95°C (30 s), 45°C (30 s), 72°C (30 s), 72°C (10 min) with 30 cycles of the central three steps. gRNA templates were purified with a DNA Clean & Concentrator Kit (Zymo Research, D4013) then subjected to in vitro RNA synthesis using a MEGAshortscript T7 Transcription Kit (Thermo Fisher Scientific, AM1354). Synthesized gRNAs were treated with 2 U of TURBO DNase (Thermo Fisher Scientific, AM2238) for 15 min at 37°C, purified using an RNA Clean & Concentrator Kit (Zymo Research, R1013) then aliquoted and stored at −80°C. For mutagenesis, 150 pg of gRNA and 100 pg of Cas9 mRNA were injected into the yolk at the one-cell stage. Injected embryos were screened for indels at the target site by PCR. Injected embryos were raised and outcrossed to establish F_1 families from which individuals were outcrossed to generate F_2 families with defined mutations determined by Sanger sequencing (GeneWiz)

For *daw1*^{b1403}, the gRNA oligo targeted exon 5 of *daw1* (Table 2), and injectees were screened using *daw1*^{b1403} sequencing primer 1 and *daw1*^{b1403} sequencing primer 2 (Table 2) followed by restriction digestion with HpyAV (New England Biolabs, R0621). The mutation isolated in *daw1*^{b1403} consists of a six base pair deletion. Mutants were routinely genotyped by identification of curly tail down (CTD) at 1 dpf and by Sanger sequencing (GeneWiz). *urp1*^{b1420} and *urp2*^{b1421} mutants were injected with mutagenesis oligos targeting either side of the cyclic peptide coding sequences and screened for large deletions. The *urp1*^{b1420} allele consists of a 279 bp deletion and 1 bp insertion that were genotyped by PCR amplification with *urp1* sequencing primers (Table 2), which generate a 460 bp band from wild-type DNA and a 184 bp band from mutant DNA. *urp2*^{b1421} mutants harbor a 61 bp deletion and were genotyped by PCR amplification with *urp2* sequencing primers primers (Table 2) followed by gel electrophoresis to distinguish the 283 bp wild-type band and the 226 bp mutant band. *uts2r3*^{b1436} mutants contain a 534 bp deletion and were also genotyped by PCR, using *uts2r3* sequencing primers (Table 2), in which wild-type sequence led to an 832 bp band and mutant sequence a 298 bp band. The *pkd2*^{b1402} allele consists of a 7 bp deletion resulting in an early stop codon. Mutants were genotyped by PCR amplification using primers in Table 2 followed by restriction digestion with HaeII (New England Biolabs, R0107). Protection by the mutant sequence resulted in a 228 bp band, while wild type DNA could be visualized by a band around 120 bp. This assay was also used to genotype the in-frame insertion alleles *pkd2*^{b1472} and *pkd2*^{b1473}, which were generated using the same guide RNA used to generate *pkd2*^{b1402}.

Two additional *pkd2* alleles containing early stop codons were generated, although not widely used for experiments. These were *pkd2*^{b1419} and *pkd2*^{b1437}. These contain, respectively, 5 bp and 2 bp deletions respectively. They were genotyped using primers found in Table 2 and digestion with NcoI (*pkd2*^{b1419}, NEB R0193) and AvaII (*pkd2*^{b1437}, NEB R0153). Protected (mutant) bands were 237 bp and 399 bp respectively, with NcoI digestion producing wild type bands of sizes 105 bp and 167 bp, and AvaII digestion generating two bands of around 200 bp.

The *pkd1*^{b1428} allele was generated using two mutagenesis oligos listed in Table 2, creating 6 bp and 16 bp deletions respectively. Mutants were regularly screened by amplifying the site targeted by mutagenesis oligo 1, followed by restriction digestion with BseRI (NEB R0581). The protected mutant band was 484 bp, while the wild type amplicon was digested into two bands of 184 bp and 300 bp. The *pkd1b*^{b1442} allele was also generated using two mutagenesis oligos (Table 2), creating 7 bp and 11 bp deletions respectively. Mutants were regularly screened by amplifying the site targeted by mutagenesis oligo 2, followed by digestion with BstNI (NEB R0168). This assay resulted in wild type digested bands each around 200 bp, and a protected mutant band of 409 bp.

The nature of the *sspo*^{b1446} mutation was determined by whole genome sequencing. DNA was extracted from mutant embryos using a phenol/chloroform procedure. Libraries were prepared using the FS DNA Library Prep Kit for Illumina sequencing (NEB, E7805). DNA was digested into 150 bp fragments, and paired-end sequencing was performed using a NovaSeq 6000 Sequencing System. Trimmomatic (version 0.36; ILLUMNIACLIP: TruSeq3-PE-2.fa:2:30:10:1:true LEADING:3 TRAILING:3 SLIDINGWINDOW:5:20 MINLEN:42 AVGQUAL:30) was used to remove Illumina adaptor sequences from paired-end reads. Illumina short-read sequences were then aligned to the GRCz11 reference sequence of chromosome 24 using BWA-MEM (version 0.7.01). SAMtools (version 1.8) was used to sort and index reads. Aligned reads in BAM format were analyzed in IGV (version 2.13.1) (Robinson et al., 2011). Mutants were routinely genotyped by PCR amplification with *sspo* sequencing primers (Table 2), followed by BsaI-HFv2 (NEB, R2733) restriction digestion to produce 300 bp and 99 bp bands from wild-type DNA and a protected 399 bp band from mutant DNA.

daw1^{b1422} mutants were isolated from clutches injected with four gRNAs (as in the 'CRISPR/Cas9 mosaic mutagenesis' section). Mutants were analyzed after outcrossing to at least the F3 generation. All four CRISPR sites were sequenced to identify mutations. The mutation occurred between gRNAs 2 and 3, with the 1 and 4 gRNAs not inducing mutations in this line. *daw1*^{b1422} mutants were genotyped by PCR using *daw1*^{b1422} sequencing primers 1 and 2 listed in Table 2, leading to a 735 bp band in wild type and an ~400 bp band in mutants.

The double mutant lines *urp1*^{b1420}*;urp2*^{b1421}, *pkd1*^{b1428}*;pkd1b*^{b1442}, *pkd2*^{b1402}*;sspo*^{b1446}, *pkd2*^{b1402}*;cfap298*^{tm304}, *pkd2*^{b1402}*;sspo-GFP*, and *daw1*^{b1403}*;sspo-GFP* were generated by crossing together F$_2$ individuals either heterozygous (*pkd1*^{b1428}, *pkd2*^{b1402}, *sspo*^{b1446}, *cfap298*^{tm304}) or homozygous (*urp1*^{b1420}, *urp2*^{b1421}, *pkd1b*^{b1442}) for the desired single mutation. *urp1*^{b1420}*;urp2*^{b1421} and *daw1*^{b1403}*;sspo-GFP* were maintained as doubly homozygous adults, *pkd1*^{b1428}*;pkd1b*^{b1442} and *pkd2*^{b1402}*;sspo-GFP* adults were maintained as het/homs, and *pkd2*^{b1402}*;sspo*^{b1446}, *pkd2*^{b1402}*;cfap298*^{tm304} were maintained as doubly heterozygous adults. The triple mutant *urp1*^{b1420}*;urp2*^{b1421}*;pkd2* was generated using mosaic mutagenesis of *pkd2* as described below performed in a *urp1*^{b1420}*;urp2*^{b1421} mutant background.

CRISPR/Cas9 mosaic mutagenesis

The four gRNA oligos used for *daw1, cfap298*, *sspo*, *urp1*, *urp2,* and *pkd2* which contained gRNA target sites and adapter sequences, were chosen from a look-up table (Wu et al., 2018), and listed here in Table 3. gRNAs were synthesized from oligos in multiplex. First, oligos were pooled (10 µM) then annealed and extended with 10µM of bottom strand oligo 2 (Table 3) using Phusion HF PCR Mastermix (New England Biolabs, M0531) and Phusion High-Fidelity DNA Polymerase (New England Biolabs, M0530) in a 50 µl reaction using cycling parameters of 98°C (2min), 50°C (10min), 72°C (10min). Assembled oligos were purified using a DNA Clean & Concentrator kit (Zymo Research, D4013) then subjected to in vitro RNA synthesis using a HiScribe T7 High Yield RNA Synthesis kit (New England Biolabs, E2040). Synthesized RNA solution was treated with 2 U of TURBO DNase (Thermo Fisher Scientific, AM2238) for 15 min at 37°C then purified using an RNA Clean & Concentrator kit (Zymo Research, R1013). Synthesized gRNAs were aliquoted and stored at −80°C. For mutagenesis, 1000 pg of gRNA mix alongside 1600 pg/nl Cas9 (Integrated DNA Technologies, 1081058) were injected into the yolk of embryos at the one-cell stage of development. To assess rates of mutagenesis in *urp1* and *urp2* injectees, DNA was extracted from 1 dpf crispants and subjected to T7 endonuclease I assays (NEB, E3321) on amplicons amplified by primers listed in Table 4.

Larval body curve quantitation

Lateral views of zebrafish larvae were captured using a Leica S9i stereomicroscope with an integrated 10-megapixel camera. Body angles, θ, were measured in ImageJ (Schindelin et al., 2012) after double-blinding. For statistical analysis of changes in θ over time, we used the repeated measures two-way analysis of variance (ANOVA) adjusted for multiple comparisons by the two-stage linear step-up procedure of Benhamini, Krieger and Yekutieli.

Calcein staining

Larvae were transferred to water containing 0.2% calcein (Sigma-Aldrich, C0875) for 10 min then briefly rinsed in water 2-3 times for 5 min each. Larvae were then immobilized with 0.005% tricaine, mounted in 0.8% low melt agarose with tricaine dropped on the surface and imaged with a Leica Thunder stereoscope.

Immunofluorescence

Embryos and larvae were euthanized and fixed in 4% paraformaldehyde at 4°C for at least 16 h. If necessary, embryos were manually dechorionated before fixation. Samples were rinsed three times in 100% methanol and then placed in 100% methanol for 2 h before being rehydrated with 5 min rinses in 75% methanol in PBST (1× PBS with 0.1% Tween-20), 50% methanol in PBST, 25% methanol in PBST and PBST. After three more 5 min washes in PBST, samples were blocked in 5% normal sheep serum (NSS) and 1% DMSO in PBST for 2 h at room temperature. Samples were then incubated in primary antibodies anti-γ-tubulin (rabbit polyclonal, 1:600, Sigma- Aldrich, T5192) and anti-acetylated α-tubulin (mouse monoclonal, 1:500, Sigma-Aldrich, T6793) in 1% NSS and 1% DMSO in PBST at 4°C for 16 h, then washed five times for 30 min per wash in 1% NSS, 1% DMSO and 0.1 M NaCl in PBST. Samples were incubated in secondary antibodies goat anti-rabbit conjugated with Alexa Fluor 546 (1:500, Thermo Fisher Scientific, A-11035) and goat anti-mouse conjugated with Alexa Fluor 488 (1:500, Thermo Fisher Scientific, A-11001) and Hoechst (1:1000, Sigma-Aldrich, 94403) at 4°C for 16 h in the dark. Samples were washed five times for 30 min per wash in 1% NSS, 1% DMSO and 0.1 M NaCl in PBST, then dissected to remove head and yolk. Trimmed samples were slide-mounted in a lateral orientation in Aqua-mount mounting medium (Polysciences, 18606) under #1.5 coverslips. Laser scanning confocal imaging was performed on a Zeiss 880 inverted microscope with a 63×, 1.4 NA oil-immersion objective and PMT and GaAsP-PMT detectors. Pinholes were set to 1 airy unit with gain between 200-300 (GaAsP-PMT) and 550-700 (PMT); x/y pixel size was 0.0851964 µm. Images were processed and quantified using ImageJ. Cilia lengths were manually traced using the Freehand Line tool (n=50 per image).

Live imaging of cilia

For central canal and pronephros imaging, 25-52 hpf embryos were manually dechorionated and anesthetized with tricaine. Embryos were laterally mounted in #1.5 coverslip-bottomed Mattek chambers by embedding in tricaine-laced, low-melt 0.5% agarose made in embryo medium. A Nikon Ti2 inverted microscope equipped with a Plan Apo VC 60× WI DIC 1.2 NA objective and pco.edge sCMOS camera was used to capture 512×512 DIC images in time series, at 250 frames per second for 4 s (1000 frames total). Pixel size was 0.11 µm. Images were processed and quantified using ImageJ. Timecourse data was rotated and cropped to isolate the CC. A moving average of 55 frames was subtracted from each frame (Stowers Institute ImageJ Plugins>jay_unruh>Detrend>Subtract Moving Average), and a Gaussian blur of 0.8 was applied to all frames. For manual analysis, line profiles were drawn through motile cilia, and kymographs were generated using KymographBuilder. For Fourier Transform-based analysis, image stacks were converted to 16-bit and processed with a Temporal Image Correlation Spectroscopy (TICS) package (Stowers>jay_unruh>ICS>stack fft TICS jru v1, analysis length=512) or FreQ package (Jeong et al., 2022). The first frame of each TICS series was deleted to account for sCMOS camera noise, and frequencies were measured from regions that overlapped cilia using the multi-measure z-axis profile tool (BAR>Analysis>Time Series>Multi ROI Profiler).

Sperm extraction and imaging

Sperm were extracted from wild-type or homozygous mutant *daw1*^{b1403} males, as described previously (Yamaguchi et al., 2018). Sperm were stored in 1/5 Hank's buffer at 4°C. A drop was applied to a 35 mm imaging chamber with #1.5 untreated coverslips, uncoated to encourage sperm head adherence. A perfusion chamber was created with a second coverslip and vacuum grease, and embryo medium was flushed through to activate sperm motility. Imaging was performed at 1 ms intervals for 750 ms, using a Nikon Ti2 inverted microscope as above.

Constructs and mRNA overexpression

Daw1 cDNA was cloned from a cDNA library generated from RNA collected at 1 dpf using a Direct-Zol RNA kit (Zymo, R2051). mCherry-Daw1 was shuttled into pCS-DEST. Site directed mutagenesis of mCherry-Daw1 constructs was performed with a Q5 Site-Directed Mutagenesis kit (New England Biolabs, E0554S), using primers listed in Table 4. mCherry-Daw1 mRNA was synthesized from plasmid DNA after restriction enzyme digestion with SacII (New England Biolabs, R0175). Linearized plasmids were purified using a DNA Clean & Concentrator kit (Zymo Research, D4013) then used as a template for in vitro mRNA synthesis using an mMessage mMachine SP6 Transcription kit (Thermo Fisher Scientific, AM1340).

mRNA was purified using lithium chloride and stored at −80°C. For overexpression, 20 pg of mRNA was injected into the blastocyst at the one-cell stage of development.

Quantitative reverse transcriptase PCR (qRT-PCR)

RNA was extracted using a Zymo Direct-Zol RNA Miniprep kit (Zymo Research, R2051). cDNA was prepared from 25 ng of RNA using oligoDT primers in a 20 µl reaction using a High Capacity cDNA Reverse Transcription Kit (ThermoFisher, 4368814). qRT-PCR reactions were performed in real time using 5 µl PowerUp SYBR Green Master Mix (ThermoFisher, A25741), 0.8 µl of 10 µM forward and reverse primers (Table 4), 1.4 µl of nuclease-free water, and 2 µl of diluted cDNA. PCR was performed using a QuantStudio Real Time PCR System (Applied Biosystems) with cycling parameters: 50°C (2 min), 95°C (10 min) then 40 cycles of 95°C (15 s), and 60°C (1 min). Each reaction was performed in quadruplicate. Quantitation was relative to rpl13 and used the ΔΔCT relative quantitation method in which fold changes are calculated as 2−ΔΔCT. The efficiency of amplification was verified to be close to 100% with a standard curve of RNA dilutions.

Multiplex fluorescent in situ hybridization chain reaction (in situ HCR)

Embryos were fixed in 4% paraformaldehyde at 4°C overnight, washed with phosphate buffered saline (PBS) then serially dehydrated to 100% methanol, and stored at –20°C. Embryos were rehy- drated, washed with PBS containing 0.1% Tween-20, incubated in hybridization buffer (Molecular Instruments), then incubated in 2 pmol of probes at 37°C overnight in a total volume of 500 µl of hybridization buffer. Embryos were washed in wash buffer (Molecular Instruments), washed twice in 5× SSCT (sodium chloride sodium citrate with 0.1% tween-20), and then incubated in amplification buffer (Molecular Instruments) for 1 hr. RNA hairpins designed to bind either *pkd2l1*, *urp1*, or *urp2* were prepared by heating 10 pmol of each to 95°C for 90 s then snap-cooled in the dark for 30 min. Embryos were then incubated overnight in 500 µl of amplification buffer containing 30 pmol hairpins at room temperature in the dark. Embryos were washed five times in 5× SSCT, stored at 4oC, and then mounted for confocal microscopy. Images were acquired using a Zeiss LSM880 using either a ×20 air or ×40 water objective. Acquisition settings were derived using wild type embryos and then applied to all embryos. Images were exported to IMARIS 9.5.0 (Oxford Instruments). A Gaussian filter of width 0.42 µm (×20) or 0.21 µm (×40), and a rolling ball background subtraction of 10 µm was applied.

X-ray microcomputed tomography

Scans were performed using a vivaCT 80 (Scanco Medical) at 18.5-µm voxel resolution (for 3 mpf and 12 mpf fish) or 10-µm voxel resolution (1 mpf fish). Single volume surface reconstitutions and DICOM files of individual fish were generated using Scanco software, imported into ImageJ and resliced (Images>Stacks>Reslice[/]) into lateral and dorsal views. Maximum intensity projections were generated for quantitation of spinal curves. Alternatively, digital dissections of the spinal column were performed in 3D Slicer (Kikinis et al., 2014) using the Segmentation Editor. A threshold of 3200 was used to mask 1 mm tube (Draw Tube function) around the spine in the axial slice view, beginning between the otic vesicles rostral to the first vertebrae and ending at the split of the tail. The center of the tube was set at the narrowest ‘hollow”’ within the lumen of centra.

Quantitation of lateral spine curvature

Quantitation of lateral spine curvature was performed in ImageJ (Schindelin et al., 2012) by orienting isolated spine images in a dorsal view with heads to the left and with the otic vesicles and first Weberian vertebrae parallel to the x-axis. Landmarks were assigned to the narrowest point of each centrum rostral to caudal; where maximum projection resulted in hidden or overlapping vertebrae, the appropriate number of points was added in closest approximation. The y-value from each landmark was subtracted from the point rostral to it, resulting in a map of local deflections where positive values indicate rightward displacement, and negative values indicate leftward displacement.

Live imaging of SCOspondin-GFP

Embryos (28 hpf) were anesthetized in tricaine until touch response was abol- ished and then embedded in 0.8% low-melt agarose laced with tricaine in inverted imaging chambers (14 mm #1.5 coverslips, VWR cat no. 10810–054). In larvae, care was taken to align the posterior body close to the coverslip to the RF within the working distance of the objective. A Nikon Ti2 inverted microscope equipped with Plan Apo ×40 and ×60 WI DIC (1.2 NA) objectives, a Yokogawa Spinning Disk and pco.edge sCMOS camera were used to capture 512×256 images in time series. Exposure time varied with age (100 ms–300 ms) as Sspo-GFP brightened in intensity over time; exposure, camera settings, and laser power were kept constant between age-matched individuals. Images were cropped, rotated, and intensity-adjusted in ImageJ (Schindelin et al., 2012).

Overnight Timecourse Imaging

As in mRNA overexpression experiments, α-bungarotoxin mRNA (Swinburne et al., 2015) was synthesized from plasmid DNA after restriction enzyme digestion with EcoRV-HF (NEB, R3195), then linearized and purified the same way. It was then used as a template for in vitro mRNA synthesis using an mMessage mMachine T7 Transcription kit (Thermo Fisher Scientific, AM1344). mRNA was purified using lithium chloride and stored at −80°C. For overexpression, 20 pg of mRNA was injected into the blastocyst at the one-cell stage of development. Embryos were then mounted in a mold obtained from Swinburne et. al. and imaged using a Leica S9i stereomicroscope with an integrated 10-megapixel camera for ≥36 hours at a rate of 6 frames per hour with an exposure time of 10ms. Body angles were quantified as described above every hour starting at approximately 22 hpf.

Generation and Imaging of Transgenic Lines

The plasmid for tissue-specific CRISPR knockout were modified from pDestTol2CG2-U6:gRNA (Addgene: 63156) (Ablain et al., 2015). First, the vector was digested with BseRI (NEB R0581) and purified using a DNA Clean & Concentrator kit (Zymo Research, D4013). Then, Gibson Assembly (NEB, E5510) was used to add two gRNA fragments (pkd2 G0 oligo 1 and pkd2 G0 oligo 2 in Table 3) framed by zebrafish U6 promoters and scaffolding sequences (synthesized by Twist Biosciences and amplified using primers in Table 4) to the vector (Adamson et al., 2016). Then, the vector was modified using Gateway Assembly (Petersen & Stowers, 2011). LR Clonase II (ThermoFisher, 11791100) to transpose Cas9-GFP cDNA (Addgene: 63155) behind *rcn3* (Ellis et al., 2013), followed by a poly-A tail (Addgene: 188702). All plasmids were mini-prepped using a GeneJet plasmid mini-prep kit (ThermoFisher, K0502), then verified using nanopore sequencing (Plasmidsaurus). For transgenesis, 25 pg were injected into the cell of wild type zebrafish embryos, then screened at 1 and 5 dpf for *cmlc:GFP*. F_0 adults were screened for GFP expression in the heart by outcrossing to wild type animals, and individuals expressing GFP in the heart and notochord were raised to create the F_1 generation. Experiments were performed on F_2 individuals resulting from outcrossed F_1's. Transgenic lines were imaged using a Leica Thunder stereoscope, Leica S9i stereomicroscope, and Zeiss AxioImager upright wide field microscope. To assess rates of mutagenesis in individuals expressing Cas9-GFP in the notochord, DNA was extracted from 1 dpf F_2 embryos positive and negative for GFP in the notochord and subjected to T7 endonuclease I assays (NEB, E3321) on amplicons amplified by primers listed in Table 4.

APPENDIX B: TABLES

Table 1: Mutant Fish Lines

Line Designation	**Citation**
cfap298^{tm304}	Jaffe et al., 2016
daw1^{b1403}	Bearce, Irons, Craig et al., 2022
daw1^{b1422}	Bearce, Irons, Craig et al., 2022
pkd1^{b1428}	this study
pkd1b^{b1442}	this study
pkd2^{b1402}	this study
pkd2^{b1419}	this study
pkd2^{b1437}	this study
pkd2^{b1472}	this study
pkd2^{b1473}	this study
pkd2l1^{icm02}	Sternberg et al., 2018
sspo-GFP^{ut24}	Troutwine et al., 2020
sspo^{b1446}	Bearce, Irons, O’Hara-Smith et al., 2022
urp1^{b1420}	Bearce, Irons, O’Hara-Smith et al., 2022
urp2^{b1421}	Bearce, Irons, O’Hara-Smith et al., 2022
uts2r3^{b1436}	Bearce, Irons, O’Hara-Smith et al., 2022
TG(rcn3:Cas9-GFP; U6: *pkd2* T1, T2)	this study

Table 2: Oligonucleotides for Mutagenesis

Name	Sequence (all 5’-3’)
bottom strand oligo 1	AAAAGCACCGACTCGGTGCCACTTTTTCAAGTTGATAACGGACTAGCCTTATTTTAACTTGCTATTTCTAGCTCTAAAAC
***daw1*^{b1403} mutagenesis oligo**	taatacgactcactataGGAAGGGTTGTTGAAGGCGAgttttagagctagaa
***daw1*^{b1403} sequencing primer 1**	CCTTCACTTTCCGTCTGTTTGCAG
***daw1*^{b1403} sequencing primer 2**	GGGACAAGTGCTCCTGTTATGACTC
***daw1*^{b1422} sequencing primer 1**	CTCCCCTTCACTTTCCGTCT
***daw1*^{b1422} sequencing primer 2**	GGTGTCCATGCTGCCTGTA
***pkd1*^{b1428} sequencing primer 1**	TTCAGGACCTGCTGGTATCC
***pkd1*^{b1428} sequencing primer 2**	TCTCAACTTTGTTGCGTTGC
***pkd1*^{b1428} mutagenesis oligo 1**	taatacgactcactataGGGGAGGGGGTCTGGGAGGAgttttagagctagaa
***pkd1*^{b1428} mutagenesis oligo 2**	taatacgactcactataGGGACTAGATCAGGCCCCGGgttttagagctagaa
***pkd1b*^{b1442} sequencing primer 1**	TAACAGCTCTGACGGACGTG
***pkd1b*^{b1442} sequencing primer 2**	ACTAATCCGAGTGCGTTGGA
***pkd1b*^{b1442} mutagenesis oligo 1**	taatacgactcactataGGGCTGCATGGACTGGTGACgttttagagctagaa
***pkd1b*^{b1442} mutagenesis oligo 2**	taatacgactcactataGGGTTTGGATTCAAGGCCAGgttttagagctagaa
***pkd2*^{b1402,b1472,b1473} sequencing primer 1**	CGCATTTTCGCATTAAGACA
***pkd2*^{b1402,b1472,b1473} sequencing primer 2**	GGAGAGGAGGGGGTCTCAT
***pkd2*^{b1402,b1472,b1473} mutagenesis oligo**	taatacgactcactataGGCAAGCGCCGCAGAGCCCGGCgttttagagctagaa
***pkd2*^{b1419} sequencing primer 1**	TGGCCATCATCAATGACACT
***pkd2*^{b1419} sequencing primer 2**	GGGTTAAATCAGTTTCATCCAA

Name	**Sequence (all 5’-3’)**
pkd2^{b1419} **mutagenesis oligo**	taatacgactcactataGGAGAGCTATAATAGAGCCAgttttagagctagaa
pkd2^{b1437} **sequencing primer 1**	GCCAAGACGACTCAGAGGAG
pkd2^{b1437} **sequencing primer 2**	AAAGTAGCGATGCGGCTTTA
pkd2^{b1437} **mutagenesis oligo**	taatacgactcactataGGTGCGCCGGGTGGACCGAAgttttagagctagaa
sspo^{b1446} **mutagenesis oligo 1**	taatacgactcactataGGTCCCCAGTGGTCCGCGGTgttttagagctagaa
sspo^{b144} **mutagenesis oligo 2**	taatacgactcactataGGCAC AGTGTGTGAGACCAGgttttagagctagaa
sspo^{b1446} **sequencing primer 1**	CGCAAACACTTCCACTTCCA
sspo^{b1446} **sequencing primer 2**	TTGAAGCCAGATGTAAAGGATGAGTGT
urp1^{b1420} **mutagenesis oligo 1**	taatacgactcactataGGCGTTGGTCAGCCTGACATgttttagagctagaa
urp1^{b1420} **mutagenesis oligo 2**	taatacgactcactataGGGTCCTCTGTCCATCTCCGgttttagagctagaa
urp1^{b1420} **sequencing primer 1**	GCACCCAAAATCCAACGACT
urp1^{b1420} **sequencing primer 2**	TGTATGGGGAAAACAAAGGCA
urp2^{b1421} **mutagenesis oligo 1**	taatacgactcactataGGCAGATGGAGAAAGATTGAgttttagagctagaa
urp2^{b1421} **mutagenesis oligo 2**	taatacgactcactataGGCGTTTGCAGAAATCAGCGgttttagagctagaa
urp2^{b1421} **sequencing primer 1**	TTGGGGTTGTAACAGGTAGTG
urp2^{b1421} **sequencing primer 2**	AACAAGGAAGACGCTGCAAG
uts2r3^{b1436} **mutagenesis oligo**	taatacgactcactataGGGTGAAGGGGAAGAGAAGAgttttagagctagaa
uts2r3^{b1436} **sequencing primer 1**	ATGGATCCCCTGATGTCCTG
uts2r3^{b1436} **sequencing primer 2**	TCGAACTCTGCTCATCCCAG

Table 3: Oligonucleotides for CRISPR/Cas9 Mosaic Mutagenesis

Name	Sequence (all 5’-3’)
bottom strand oligo 2	AAAAGCACCGACTCGGTGCCACTTTTTCAAGTTGATAACGGACTAGCCTTATTTTAACTTGCTATTTCTAGCTCTAAAAC
***cfap298* G0 oligo 1**	TAATACGACTCACTATAGGTTCTCTTCAACACTACGGGTTTTAGAGCTAGAAATAGC
***cfap298* G0 oligo 2**	TAATACGACTCACTATAGGGCTCCACAATCTGATCATGTTTTAGAGCTAGAAATAGC
***cfap298* G0 oligo 3**	TAATACGACTCACTATAGGCATTCTTATTGGATCATGGTTTTAGAGCTAGAAATAGC-3′
***cfap298* G0 oligo 4**	TAATACGACTCACTATAGGTCTCTGGCAGGTGCGCCCGTTTTAGAGCTAGAAATAGC-3′
***daw1* G0 oligo 1**	TAATACGACTCACTATAGGTCACCTGCTCGACACAGGGTTTTAGAGCTAGAAATAGC
***daw1* G0 oligo 2**	TAATACGACTCACTATAGGGCGGTGCTGTTACCCGTAGTTTTAGAGCTAGAAATAGC
***daw1* G0 oligo 3**	TAATACGACTCACTATAGGGTCTATTATAGGTATGCCGTTTTAGAGCTAGAAATAGC
***daw1* G0 oligo 4**	TAATACGACTCACTATAGGCTGCTTGCGTATAGGTGTGTTTTAGAGCTAGAAATAGC
***pkd2* G0 oligo 1**	TAATACGACTCACTATAGGTGGTGCTCACCATTCCATGTTTTAGAGCTAGAAATAGC
***pkd2* G0 oligo 2**	TAATACGACTCACTATAGGGCTGATTTCTCCCGTGTGGTTTTAGAGCTAGAAATAGC
***pkd2* G0 oligo 3**	TAATACGACTCACTATAGGCACAGCGCCCCCTGTGGCGTTTTAGAGCTAGAAATAGC
***pkd2* G0 oligo 4**	TAATACGACTCACTATAGGGCTCCGCCAAGACCTTAGGTTTTAGAGCTAGAAATAGC
***sspo* G0 oligo 1**	TAATACGACTCACTATAGGTTCGTCCCCAGTGGTCCGGTTTTAGAGCTAGAAATAGC
***sspo* G0 oligo 2**	TAATACGACTCACTATAGGAAACGGCCGTCAGTGTCGGTTTTAGAGCTAGAAATAGC

Name	**Sequence (all 5’-3’)**
***sspo* G0 oligo 3**	TAATACGACTCACTATAGGTGTTGCAACACCAACCGGGTTTTAGAGCTAGAAATAGC
***sspo* G0 oligo 4**	TAATACGACTCACTATAGGAGCCTAGACCTGCTCACGGTTTTAGAGCTAGAAATAGC
***urp1* G0 oligo 1**	TAATACGACTCACTATAGGAAAGTGAAGATCGCGGCCGTTTTAGAGCTAGAAATAGC
***urp1* G0 oligo 2**	TAATACGACTCACTATAGGACACGGCTCTGCCACAACGTTTTAGAGCTAGAAATAGC
***urp1* G0 oligo 3**	TAATACGACTCACTATAGGTTCAGAAGCTGGTAGCAGGTTTTAGAGCTAGAAATAGC
***urp1* G0 oligo 4**	TAATACGACTCACTATAGGGAAAATAAATAACATGGTGTTTTAGAGCTAGAAATAGC
***urp2* G0 oligo 1**	TAATACGACTCACTATAGGTGACTGTCGCTTCAATCGGTTTTAGAGCTAGAAATAGC
***urp2* G0 oligo 2**	TAATACGACTCACTATAGGGACATTTCCTGACGGAGAGTTTTAGAGCTAGAAATAGC
***urp2* G0 oligo 3**	TAATACGACTCACTATAGGTGGACACGAGGAGACCGAGTTTTAGAGCTAGAAATAGC
***urp2* G0 oligo 4**	TAATACGACTCACTATAGGTCACCAGGTAGTGACGGAGTTTTAGAGCTAGAAATAGC

Table 4: Miscellaneous Primers

Name	**Sequence (all 5'-3')**
Daw1^{Asn143Asp}_F for site-directed mutagenesis	CATCGCCTTCgACAACCCTTA
Daw1^{Asn143Asp}_R for site-directed mutagenesis	GCATACACAACGTTCCTG
Daw1^{b1402}_F for site-directed mutagenesis	TTCAACAACCCTTACGGAG
Daw1^{b140}_R for site-directed mutagenesis	GGCATACACAACGTTCCTG
Daw1^{Trp372Cys}_F for site-directed mutagenesis	CTCGTGTGTGtTGTGTGAAGAC
Daw1^{Trp372Cys}_R for site-directed mutagenesis	ACGTTTTGTCCACACTCG
***pkd2*_gRNA1_F for T7E1 assay**	TTCCCTGCTGCTGAATCTGA
***pkd2*_gRNA1_R for T7E1 assay**	CCTCCATGGTTGAAAGGCTC
***pkd2*_gRNA2_F for T7E1 assay**	GGATGAGAGTAGCCTGGGTG
***pkd2*_gRNA2_R for T7E1 assay**	TGCTCTTACAACTGGGATCGA
***pkd2*_fragment1-F for gibson cloning**	agtccctggtatatatagctctccctccagctcttggttcGCGTCTTTTGTTCTGGTCATCAAGG
***pkd2*_fragment1-R for gibson cloning**	ATGACCAGAACAAAAGACGCAAAAAAGCACCGACTCGGTG
***pkd2*_fragment2-F for gibson cloning**	CACCGAGTCGGTGCTTTTTTGCGTCTTTTGTTCTGGTCATCAAGG
***pkd2*_fragment2-R for gibson cloning**	ATGACCAGAACAAAAGACGCAAAAAAGCACCGACTCGGTG
***pkd2*_vector-F for gibson cloning**	CACCGAGTCGGTGCTTTTTTttttttggtaccgt
***pkd2*_vector-R for gibson cloning**	ATGACCAGAACAAAAGACGCatcgatgatgat
***rpl13*_F for qPCR**	TAAGGACGGAGTGAACAACCA
***rpl13*_R for qPCR**	CTTACGTCTGCGGATCTTTCTG
***urp1*_F for qPCR**	ACATTCTGGCTGTGGTTTG
***urp1*_R for qPCR**	GTCCGTCTTCAACCTCTGCTAC

Name	**Sequence (all 5’-3’)**
***urp1*_gRNA1+2_F for T7E1 assay**	GACAGCGCACCCTTAATTGT
***urp1*_gRNA1+2_R for T7E1 assay**	ACATTTAGCCTTAACAAGCACAA
***urp1*_gRNA3+4_F for T7E1 assay**	CAGACAAGGGAACAGAGAGGA
***urp1*_gRNA3+4_R for T7E1 assay**	CCACTGCTTTTAAATCATCCACC
***urp2*_F for qPCR**	AGAGGAAACAGCAATGGACG
***urp2*_R for qPCR**	TGTTGGTTTTGGTTGACG
***urp2*_gRNA1_F for T7E1 assay**	ATCTTAGAGGCGCATTGGTG
***urp2*_gRNA1_R for T7E1 assay**	GCATGAGGCGGTTTGTTTTG
***urp2*_gRNA2+3_F for T7E1 assay**	TGAAGCAACTGAGGAGCAAA
***urp2*_gRNA2+3_R for T7E1 assay**	ACAGTACAGTTCAGCACACCT
***urp2*_gRNA4_F for T7E1 assay**	TGACCTATACATCAAAGCCAAGG
***urp2*_gRNA4_R for T7E1 assay**	CCTGGGCTGATCATACCTCT

APPENDIX C: MOVIE LEGENDS

All movies are included as supplemental files to this dissertation.

Movie 1. Reconstitutions of µCT data of sections of the vertebral column in *daw1*^{b1403} mutant adults and controls. Vertebrae 8–12 were segmented from two whole-animal µCT scans and reconstituted using 3D Viewer (ImageJ).

Movie 2. Central canal cilia at 25 h.p.f. in *daw1*^{b1403} mutants and controls. Images were acquired with a Nikon Ti2 inverted microscope and pco.edge sCMOS camera at 250 frames per second. The movie is replayed at 50 frames per second. Upper panels show DIC with a small Gaussian blur. Lower panels show background subtracted series using a moving average of 55 frames. Scale bar — 5 µm. Left - rostral; top - dorsal.

Movie 3. Central canal cilia at 34 h.p.f. in *daw1*^{b1403} mutants and controls. Images were acquired with a Nikon Ti2 inverted microscope and pco.edge sCMOS camera at 250 frames per second for 4 seconds. The movie is replayed at 50 frames per second. Upper panels show DIC with a small Gaussian blur. Lower panels show background subtracted series using a moving average of 55 frames. Scale bar — 5 µm. Left - rostral; top - dorsal.

Movie 4. Central canal cilia at 43 h.p.f. in *daw1*^{b1403} mutants and controls. Images were acquired with a Nikon Ti2 inverted microscope and pco.edge sCMOS camera at 250 frames per second for 4 seconds. The movie is replayed at 50 frames per second. Upper panels show DIC with a small Gaussian blur. Lower panels show background subtracted series using a moving average of 55 frames. Scale bar — 5 µm. Left - rostral; top - dorsal.

Movie 5. Central canal cilia at 52 h.p.f. in *daw1*^{b1403} mutants and controls. Images were acquired with a Nikon Ti2 inverted microscope and pco.edge sCMOS camera at 250 frames per second for 4 seconds. The movie is replayed at 50 frames per second. Upper panels show DIC with a small Gaussian blur. Lower panels show background subtracted series using a moving average of 55 frames. Scale bar — 5 µm. Left - rostral; top - dorsal.

Movie 6. Pronephric duct cilia at 25 h.p.f. in control embryos. Images were acquired with a Nikon Ti2 inverted microscope and pco.edge sCMOS camera at 250 frames per second for 2 seconds. The movie (400 ms) is replayed at 50 frames per second. Left panels show DIC with a small Gaussian blur from three individual embryos. Right panels show background subtracted series using a moving average of 55 frames. Scale bar — 5 µm. Left - proximal direction; top - dorsal.

Movie 7. Pronephric duct cilia at 25 h.p.f. in *daw1*^{b1403} mutants. Images were acquired with a Nikon Ti2 inverted microscope and pco.edge sCMOS camera at 250 frames per second for 2 seconds. The movie (400 ms) is replayed at 50 frames per second. Left panels show DIC with a small Gaussian blur from three individual embryos. Right panels show background subtracted series using a moving average of 55 frames. Scale bar — 5 µm. Left - proximal direction; top - dorsal.

Movie 8. Pronephric duct cilia at 34 h.p.f. in control embryos. Images were acquired with a Nikon Ti2 inverted microscope and pco.edge sCMOS camera at 250 frames per second for 2 seconds. The movie (400 ms) is replayed at 50 frames per second. Left panels show DIC with a small Gaussian blur from three individual embryos. Right panels show background subtracted series using a moving average of 55 frames. Scale bar — 5 µm. Left - proximal direction; top - dorsal.

Movie 9. Pronephric duct cilia at 34 h.p.f. in *daw1^{b1403}* mutants. Images were acquired with a Nikon Ti2 inverted microscope and pco.edge sCMOS camera at 250 frames per second for 2 seconds. The movie (400 ms) is replayed at 50 frames per second. Left panels show DIC with a small Gaussian blur from three individual embryos. Right panels show background subtracted series using a moving average of 55 frames. Scale bar — 5 µm. Left - proximal direction; top - dorsal.

Movie 10. Sperm flagella extracted from adult male sibling controls. Images were acquired with a Nikon Ti2 inverted microscope and pco.edge sCMOS camera at 1000 frames per second for 1 second. The movie (500 ms) is replayed at 50 frames per second. Panels show data from three sperm preparations. Scale bar — 5 µm.

Movie 11. Sperm flagella extracted from adult male *daw1^{b1403}* mutants. Images were acquired with a Nikon Ti2 inverted microscope and pco.edge sCMOS camera at 1000 frames per second for 1 second. The movie (500 ms) is replayed at 50 frames per second. Panels show data from three sperm preparations. Scale bar — 5 µm.

Move 12. KV cilia in 10 somite staged wild-type control embryos. Images were acquired with a GE DeltaVision Ultra microscope at 500 frames per second for 1 second. The movie is replayed at 25 frames per second. Panels show four individual embryos. Scale bar — 5 µm.

Movie 13. KV cilia in 10 somite staged *daw1^{b1403}* mutants. Images were acquired with a GE DeltaVision Ultra microscope at 500 frames per second for 1 second. The movie is replayed at 25 frames per second. Panels show four individual embryos. Arrow heads show immotile cilia. Scale bar — 5 µm.

Movie 14. Central canal cilia at 25 h.p.f. in *cfap298^{tm304}* mutants and controls raised at 30°C. Images were acquired with a Nikon Ti2 inverted microscope and pco.edge sCMOS camera at 250 frames per second for 4 seconds. The movie is replayed at 50 frames per second. Upper panels show DIC with a small Gaussian blur. Lower panels show background subtracted using a moving average of 55 frames. Scale bar — 5 µm. Left - rostral; top - dorsal.

Movie 15. Central canal cilia at 52 h.p.f. in *cfap298*^{tm304} mutants and controls raised at 30°C until 28 h.p.f. then downshifted to 22°C. Images were acquired with a Nikon Ti2 inverted microscope and pco.edge sCMOS camera at 250 frames per second for 4 seconds. The movie is replayed at 50 frames per second. Upper panels show DIC with a small Gaussian blur. Lower panels show background subtracted using a moving average of 55 frames. Scale bar — 5 µm. Left - rostral; top - dorsal.

Movie 16. Central canal cilia at 52 h.p.f. in *cfap298*^{tm304} mutants and controls raised at 30°C. Images were acquired with a Nikon Ti2 inverted microscope and pco.edge sCMOS camera at 250 frames per second for 4 seconds. The movie is replayed at 50 frames per second. Upper panels show DIC with a small Gaussian blur. Lower panels show background subtracted using a moving average of 55 frames. Scale bar — 5 µm. Left - rostral; top - dorsal.

Movie 17. KV cilia motility in *daw1*^{b1403} mutants injected with *daw1*^{WT} mRNA. Images were acquired with a GE DeltaVision Ultra microscope at 500 frames per second for 1 second. The movie is replayed at 25 frames per second. Panels show individual mutant embryos; cilia motility is rescued. Scale – 5 µm.

Movie 18. KV cilia motility in *daw1*^{b1403} mutants injected with *daw1*^{Asn143Asp} mRNA. Images were acquired with a GE DeltaVision Ultra microscope at 500 frames per second for 1 second. The movie is replayed at 25 frames per second. Panels show individual mutant embryos; cilia motility is not rescued. Arrow heads show immotile cilia. Scale – 5 µm.

Movie 19. KV cilia motility in *daw1*^{b1403} mutants injected with *daw1*^{Ser364Thr} mRNA. Images were acquired with a GE DeltaVision Ultra microscope at 500 frames per second for 1 second. The movie is replayed at 25 frames per second. Panels show individual mutant embryos; cilia motility is not rescued. Arrow heads show immotile cilia. Scale – 5 µm.

Movie 20. KV cilia motility in *daw1*^{b1403} mutants injected with *daw1*^{Trp372Cys} mRNA. Images were acquired with a GE DeltaVision Ultra microscope at 500 frames per second for 1 second. The movie is replayed at 25 frames per second. Panels show individual mutant embryos; cilia motility is partially rescued. Arrow heads indicate cilia with partially restored motility. Scale – 5 µm.

Movie 21. Straightening timecourse of WT, *pkd1*^{b1402}, and *pkd1*^{b1428}*;pkd1b*^{b1442} embryos. Images were acquired with a Leica S9i stereoscope at 6 frames per hour for 48 hours. The movie is replayed at 6 frames per second. Panels show a wild type embryo (top), a *pkd1*^{b1402} mutant embryo (middle), and a *pkd1*^{b1428}*;pkd1b*^{b1442} double mutant embryo (bottom). Scale – 1 mm.

Movie 22. Central canal cilia at 28 h.p.f. in a *pkd2*^{b1402} mutant and sibling. Images were acquired with a Nikon Ti2 inverted microscope and pco.edge sCMOS camera at 250 frames per second for 4 seconds. The movie is replayed at 25 frames per second. Upper panels show DIC with a small Gaussian blur. Lower panels show background subtracted using a moving average of 55 frames. Left panels show a wild type central canal, right panels show one of a *pkd2*^{b1402} mutant. Scale bar — 10 µm. Left - rostral; top - dorsal.

Movie 23. Sspo-GFP in the central canal at 28 h.p.f. in a *pkd2*^{b1402} mutant and sibling. Images were acquired with a Nikon Ti2 inverted microscope and pco.edge sCMOS camera at 2 frames per second for 9 seconds. The movie is replayed at 6 frames per second. The top panel shows a wild type RF, the lower panel shows the RF of a *pkd2*^{b1402} mutant. Scale bar — 10 µm. Left - rostral; top - dorsal.

REFERENCES CITED

Ablain, J., Durand, E. M., Yang, S., Zhou, Y., & Zon, L. I. (2015). A CRISPR/Cas9 vector system for tissue-specific gene disruption in zebrafish. *Dev Cell*, *32*(6), 756-764. https://doi.org/10.1016/j.devcel.2015.01.032

Adamson, B., Norman, T. M., Jost, M., Cho, M. Y., Nunez, J. K., Chen, Y., Villalta, J. E., Gilbert, L. A., Horlbeck, M. A., Hein, M. Y., Pak, R. A., Gray, A. N., Gross, C. A., Dixit, A., Parnas, O., Regev, A., & Weissman, J. S. (2016). A Multiplexed Single-Cell CRISPR Screening Platform Enables Systematic Dissection of the Unfolded Protein Response. *Cell*, *167*(7), 1867-1882 e1821. https://doi.org/10.1016/j.cell.2016.11.048

Ahmed, N. T., Gao, C., Lucker, B. F., Cole, D. G., & Mitchell, D. R. (2008). ODA16 aids axonemal outer row dynein assembly through an interaction with the intraflagellar transport machinery. *The Journal of Cell Biology*, *183*(2), 313-322. https://doi.org/10.1083/jcb.200802025

Ahmed, N. T., & Mitchell, D. R. (2005). ODA16p, a Chlamydomonas Flagellar Protein Needed for Dynein Assembly. *Molecular Biology of the Cell*, *16*(10), 5004-5012. https://doi.org/10.1091/mbc.e05-07-0627

Ames, R. S., Sarau, H. M., Chambers, J. K., Willette, R. N., Aiyar, N. V., Romanic, A. M., Louden, C. S., Foley, J. J., Sauermelch, C. F., Coatney, R. W., Ao, Z., Disa, J., Holmes, S. D., Stadel, J. M., Martin, J. D., Liu, W.-S., Glover, G. I., Wilson, S., McNulty, D. E., . . . Douglas, S. A. (1999). Human urotensin-II is a potent vasoconstrictor and agonist for the orphan receptor GPR14. *Nature*, *401*(6750), 282-286. https://doi.org/10.1038/45809

Archer, J. E., Gardner, A. C., Roper, H. P., Chikermane, A. A., & Tatman, A. J. (2016). Duchenne muscular dystrophy: the management of scoliosis. *J Spine Surg*, *2*(3), 185-194. https://doi.org/10.21037/jss.2016.08.05

Austin-Tse, C., Halbritter, J., Maimoona, Renée, Heon, Hellman, N., Pathak, N., Liu, Y., Jennifer, Ramila, Tritschler, D., Bower, R., O'Toole, E., Porath, J. D., Toby, Chaki, M., Katrina, Kohl, S., Lovric, S., . . . Hildebrandt, F. (2013). Zebrafish Ciliopathy Screen Plus Human Mutational Analysis Identifies C21orf59 and CCDC65 Defects as Causing Primary Ciliary Dyskinesia. *The American Journal of Human Genetics*, *93*(4), 672-686. https://doi.org/10.1016/j.ajhg.2013.08.015

Bae, Y. K., Qin, H., Knobel, K. M., Hu, J., Rosenbaum, J. L., & Barr, M. M. (2006). General and cell-type specific mechanisms target TRPP2/PKD-2 to cilia. *Development*, *133*(19), 3859-3870. https://doi.org/10.1242/dev.02555

Bagnat, M., & Gray, R. S. (2020). Development of a straight vertebrate body axis. *Development*, *147*(21), dev175794. https://doi.org/10.1242/dev.175794

Baker, K., Holtzman, N. G., & Burdine, R. D. (2008). Direct and indirect roles for Nodal signaling in two axis conversions during asymmetric morphogenesis of the zebrafish heart. *Proc Natl Acad Sci U S A*, *105*(37), 13924-13929. https://doi.org/10.1073/pnas.0802159105

Baldridge, D., Wangler, M. F., Bowman, A. N., Yamamoto, S., Undiagnosed Diseases, N., Schedl, T., Pak, S. C., Postlethwait, J. H., Shin, J., Solnica-Krezel, L., Bellen, H. J., & Westerfield, M. (2021). Model organisms contribute to diagnosis and discovery in the undiagnosed diseases network: current state and a future vision. *Orphanet J Rare Dis*, *16*(1), 206. https://doi.org/10.1186/s13023-021-01839-9

Bearce, E. A., & Grimes, D. T. (2021). On being the right shape: Roles for motile cilia and cerebrospinal fluid flow in body and spine morphology. *Semin Cell Dev Biol*, *110*, 104-112. https://doi.org/10.1016/j.semcdb.2020.07.005

Bearce, E. A., Irons, Z. H., Craig, S. B., Kuhns, C. J., Sabazali, C., Farnsworth, D. R., Miller, A. C., & Grimes, D. T. (2022). Daw1 regulates the timely onset of cilia motility during development. *Development*, *149*(12). https://doi.org/10.1242/dev.200017

Bearce, E. A., Irons, Z. H., O'Hara-Smith, J. R., Kuhns, C. J., Fisher, S. I., Crow, W. E., & Grimes, D. T. (2022). Urotensin II-related peptides, Urp1 and Urp2, control zebrafish spine morphology. *Elife*, *11*. https://doi.org/10.7554/eLife.83883

Becker-Heck, A., Zohn, I. E., Okabe, N., Pollock, A., Lenhart, K. B., Sullivan-Brown, J., McSheene, J., Loges, N. T., Olbrich, H., Haeffner, K., Fliegauf, M., Horvath, J., Reinhardt, R., Nielsen, K. G., Marthin, J. K., Baktai, G., Anderson, K. V., Geisler, R., Niswander, L., . . . Burdine, R. D. (2011). The coiled-coil domain containing protein CCDC40 is essential for motile cilia function and left-right axis formation. *Nat Genet*, *43*(1), 79-84. https://doi.org/10.1038/ng.727

Bisgrove, B. W., Snarr, B. S., Emrazian, A., & Yost, H. J. (2005). Polaris and Polycystin-2 in dorsal forerunner cells and Kupffer's vesicle are required for specification of the zebrafish left-right axis. *Dev Biol*, *287*(2), 274-288. https://doi.org/10.1016/j.ydbio.2005.08.047

Boswell, C. W., & Ciruna, B. (2017). Understanding Idiopathic Scoliosis: A New Zebrafish School of Thought. *Trends Genet*, *33*(3), 183-196. https://doi.org/10.1016/j.tig.2017.01.001

Bottier, M., Thomas, K. A., Dutcher, S. K., & Bayly, P. V. (2019). How Does Cilium Length Affect Beating? *Biophys J*, *116*(7), 1292-1304. https://doi.org/10.1016/j.bpj.2019.02.012

Boucher, C., & Sandford, R. (2004). Autosomal dominant polycystic kidney disease (ADPKD, MIM 173900, PKD1 and PKD2 genes, protein products known as polycystin-1 and polycystin-2). *Eur J Hum Genet*, *12*(5), 347-354. https://doi.org/10.1038/sj.ejhg.5201162

Brand, M., Heisenberg, C.-P., Warga, R. M., Pelegri, F., Karlstrom, R. O., Beuchle, D., Picker, A., Jiang, Y.-J., Furutani-Seiki, M., van Eeden, J. M. F., Granato, M., Haffter, P., Hammerschmidt, M., Kane, D. A., Kelsh, R. N., Mullins, M. C., Odenthal, J., & Nusslein-Volhard, C. (1996). Mutations affecting development of the midline and general body shape during zebrafish embryogenesis. *Development*, *123*, 129-142.

Bycroft, M. B., Alex; Clarke, Jane; Hamill, Stefan J.; Sandford, Richard; Thomas, Ruth L.; Chothia, Cyrus. (1999). The structure of a PKD domain from polycystin-1: implications for polycystic kidney disease. *The EMBO Journal*, *18*, 297–305. https://doi.org/https://doi.org/10.1093/emboj/18.2.297

Cantaut-Belarif, Y., Orts Del'Immagine, A., Penru, M., Pezeron, G., Wyart, C., & Bardet, P. L. (2020). Adrenergic activation modulates the signal from the Reissner fiber to cerebrospinal fluid-contacting neurons during development. *Elife*, *9*. https://doi.org/10.7554/eLife.59469

Cantaut-Belarif, Y., Sternberg, J. R., Thouvenin, O., Wyart, C., & Bardet, P. L. (2018). The Reissner Fiber in the Cerebrospinal Fluid Controls Morphogenesis of the Body Axis. *Curr Biol*, *28*(15), 2479-2486 e2474. https://doi.org/10.1016/j.cub.2018.05.079

Chatenet, D., Dubessy, C., Leprince, J., Boularan, C., Carlier, L., Ségalas-Milazzo, I., Guilhaudis, L., Oulyadi, H., Davoust, D., Scalbert, E., Pfeiffer, B., Renard, P., Tonon, M.-C., Lihrmann, I., Pacaud, P., & Vaudry, H. (2004). Structure–activity relationships and structural conformation of a novel urotensin II-related peptide. *Peptides*, *25*(10), 1819-1830. https://doi.org/https://doi.org/10.1016/j.peptides.2004.04.019

Chen, W., Liu, J., Yuan, D., Zuo, Y., Liu, Z., Liu, S., Zhu, Q., Qiu, G., Huang, S., Giampietro, P. F., Zhang, F., Wu, N., & Wu, Z. (2016). Progress and perspective of TBX6 gene in congenital vertebral malformations. *Oncotarget*, *7*(35). https://www.oncotarget.com/article/10619/text/

Clapham, D. E. (1995). Calcium signaling. *Cell*, *80*(2), 259-268. https://doi.org/https://doi.org/10.1016/0092-8674(95)90408-5

Colantonio, J. R., Vermot, J., Wu, D., Langenbacher, A. D., Fraser, S., Chen, J. N., & Hill, K. L. (2009). The dynein regulatory complex is required for ciliary motility and otolith biogenesis in the inner ear. *Nature*, *457*(7226), 205-209. https://doi.org/10.1038/nature07520

Dai, J., Barbieri, F., Mitchell, D. R., & Lechtreck, K. F. (2018). In vivo analysis of outer arm dynein transport reveals cargo-specific intraflagellar transport properties. *Mol Biol Cell*, *29*(21), 2553-2565. https://doi.org/10.1091/mbc.E18-05-0291

Dai, Z., Wang, Y., Wu, Z., Feng, Z., Liu, Z., Qiu, Y., Cheng, J. C., Xu, L., & Zhu, Z. (2021). Novel Mutations in UTS2R are Associated with Adolescent Idiopathic Scoliosis in the Chinese Population. *Spine (Phila Pa 1976)*, *46*(5), E288-E293. https://doi.org/10.1097/BRS.0000000000003786

Dale, N., Roberts, A., Otterson, O. P., & Storm-Mathisen, J. (1987). The morphology and distribution of 'Kolmer-Agduhr cells', a class of cerebrospinal-fluid-contacting neurons revealed in the frog embryo spinal cord by GABA immunocytochemistry. *Proc R Soc Lond*, *232*, 193-203.

Demarin, V., Morovic, S., & Bene, R. (2014). Neuroplasticity. *Periodicum Biologorum*, *116*(2), 209-211.

Desgrange, A., Le Garrec, J. F., & Meilhac, S. M. (2018). Left-right asymmetry in heart development and disease: forming the right loop. *Development*, *145*(22). https://doi.org/10.1242/dev.162776

Djenoune, L., Khabou, H., Joubert, F., Quan, F. B., Nunes Figueiredo, S., Bodineau, L., Del Bene, F., Burckle, C., Tostivint, H., & Wyart, C. (2014). Investigation of spinal cerebrospinal fluid-contacting neurons expressing PKD2L1: evidence for a conserved system from fish to primates. *Front Neuroanat*, *8*, 26. https://doi.org/10.3389/fnana.2014.00026

Djenoune, L., Mahamdeh, M., Truong, T. V., Nguyen, C. T., Fraser, S. E., Brueckner, M., Howard, J., & Yuan, S. (2023). Cilia function as calcium-mediated mechanosensors that instruct left-right asymmetry. *Science*, *379*(6627), 71-78. https://doi.org/doi:10.1126/science.abq7317

Douguet, D., Patel, A., & Honore, E. (2019). Structure and function of polycystins: insights into polycystic kidney disease. *Nat Rev Nephrol*, *15*(7), 412-422. https://doi.org/10.1038/s41581-019-0143-6

Drummond, I. A. (2012). Cilia functions in development. *Curr Opin Cell Biol*, *24*(1), 24-30. https://doi.org/10.1016/j.ceb.2011.12.007

Eisen, J. S., & Smith, J. C. (2008). Controlling morpholino experiments: don't stop making antisense. *Development*, *135*(10), 1735-1743. https://doi.org/10.1242/dev.001115

El-Brolosy, M. A., Kontarakis, Z., Rossi, A., Kuenne, C., Gunther, S., Fukuda, N., Kikhi, K., Boezio, G. L. M., Takacs, C. M., Lai, S. L., Fukuda, R., Gerri, C., Giraldez, A. J., & Stainier, D. Y. R. (2019). Genetic compensation triggered by mutant mRNA degradation. *Nature*, *568*(7751), 193-197. https://doi.org/10.1038/s41586-019-1064-z

Ellis, K., Bagwell, J., & Bagnat, M. (2013). Notochord vacuoles are lysosome-related organelles that function in axis and spine morphogenesis. *J Cell Biol*, *200*(5), 667-679. https://doi.org/10.1083/jcb.201212095

Elshourbagy, N. A., Douglas, S. A., Shabon, U., Harrison, S., Duddy, G., Sechler, J. L., Ao, Z., Maleeff, B. E., Naselsky, D., Disa, J., & Aiyar, N. V. (2002). Molecular and pharmacological characterization of genes encoding urotensin-II peptides and their cognate G-protein-coupled receptors from the mouse and monkey. *Br J Pharmacol*, *136*(1), 9-22. https://doi.org/10.1038/sj.bjp.0704671

England, S. J., Campbell, P. C., Banerjee, S., Swanson, A. J., & Lewis, K. E. (2017). Identification and Expression Analysis of the Complete Family of Zebrafish pkd Genes. *Front Cell Dev Biol*, *5*, 5. https://doi.org/10.3389/fcell.2017.00005

Essner, J. J., Amack, J. D., Nyholm, M. K., Harris, E. B., & Yost, H. J. (2005). Kupffer's vesicle is a ciliated organ of asymmetry in the zebrafish embryo that initiates left-right development of the brain, heart and gut. *Development*, *132*(6), 1247-1260. https://doi.org/10.1242/dev.01663

Farnsworth, D. R., Saunders, L. M., & Miller, A. C. (2020). A single-cell transcriptome atlas for zebrafish development. *Dev Biol*, *459*(2), 100-108. https://doi.org/10.1016/j.ydbio.2019.11.008

Field, S., Riley, K. L., Grimes, D. T., Hilton, H., Simon, M., Powles-Glover, N., Siggers, P., Bogani, D., Greenfield, A., & Norris, D. P. (2011). Pkd1l1 establishes left-right asymmetry and physically interacts with Pkd2. *Development*, *138*(6), 1131-1142. https://doi.org/10.1242/dev.058149

Fowkes, M. E., & Mitchell, D. R. (1998). The Role of Preassembled Cytoplasmic Complexes in Assembly of Flagellar Dynein Subunits. *Molecular Biology of the Cell*, *9*(9), 2337-2347. https://doi.org/10.1091/mbc.9.9.2337

Gaillard, A. L., Mohamad, T., Quan, F. B., de Cian, A., Mosimann, C., Tostivint, H., & Pezeron, G. (2023). Urp1 and Urp2 act redundantly to maintain spine shape in zebrafish larvae. *Dev Biol*, *496*, 36-51. https://doi.org/10.1016/j.ydbio.2023.01.010

Gao, C., Wang, G., Amack, J. D., & Mitchell, D. R. (2010). Oda16/Wdr69 is essential for axonemal dynein assembly and ciliary motility during zebrafish embryogenesis. *Dev Dyn*, *239*(8), 2190-2197. https://doi.org/10.1002/dvdy.22355

Geng, L., Okuhara, D., Yu, Z., Tian, X., Cai, Y., Shibazaki, S., & Somlo, S. (2006). Polycystin-2 traffics to cilia independently of polycystin-1 by using an N-terminal RVxP motif. *J Cell Sci*, *119*(Pt 7), 1383-1395. https://doi.org/10.1242/jcs.02818

Gorman, K. F., & Breden, F. (2009). Idiopathic-type scoliosis is not exclusive to bipedalism. *Med Hypotheses*, *72*(3), 348-352. https://doi.org/10.1016/j.mehy.2008.09.052

Gourronc, F., Ahmad, N., Nedza, N., Eggleston, T., & Rebagliati, M. (2007). Nodal activity around Kupffer's vesicle depends on the T-box transcription factors Notail and Spadetail and on Notch signaling. *Dev Dyn*, *236*(8), 2131-2146. https://doi.org/10.1002/dvdy.21249

Grant, M. G., Patterson, V. L., Grimes, D. T., & Burdine, R. D. (2017). Chapter One - Modeling Syndromic Congenital Heart Defects in Zebrafish. In K. C. Sadler (Ed.), *Current Topics in Developmental Biology* (Vol. 124, pp. 1-40). Academic Press. https://doi.org/https://doi.org/10.1016/bs.ctdb.2016.11.010

Grimes, D. T. (2019a). Developmental Biology: Go with the Flow to Keep the Body Straight. *Curr Biol*, *29*(3), R101-R103. https://doi.org/10.1016/j.cub.2018.12.011

Grimes, D. T. (2019b). Making and breaking symmetry in development, growth and disease. *Development*, *146*(16). https://doi.org/10.1242/dev.170985

Grimes, D. T., Boswell, C. W., Morante, N. F., Henkelman, R. M., Burdine, R. D., & Ciruna, B. (2016). Zebrafish models of idiopathic scoliosis link cerebrospinal fluid flow defects to spine curvature. *Science*, *352*(6291), 1341-1344. https://doi.org/10.1126/science.aaf6419

Grimes, D. T., & Burdine, R. D. (2017). Left-Right Patterning: Breaking Symmetry to Asymmetric Morphogenesis. *Trends Genet*, *33*(9), 616-628. https://doi.org/10.1016/j.tig.2017.06.004

Grimes, D. T., Keynton, J. L., Buenavista, M. T., Jin, X., Patel, S. H., Kyosuke, S., Vibert, J., Williams, D. J., Hamada, H., Hussain, R., Nauli, S. M., & Norris, D. P. (2016). Genetic Analysis Reveals a Hierarchy of Interactions between Polycystin-Encoding Genes and Genes Controlling Cilia Function during Left-Right Determination. *PLoS Genet*, *12*(6), e1006070. https://doi.org/10.1371/journal.pgen.1006070

Haffter, P., Granato, M., Brand, M., Mullins, M. C., Hammerschmidt, M., Kane, D. A., Odenthal, J., van Eeden, J. M. F., Jiang, Y.-J., Heisenberg, C.-P., Kelsh, R. N., Furutani-Seiki, M., Vogelsang, E., Beuchle, D., Schach, U., Fabain, C., & Nusslein-Volhard, C. (1996). The identification of genes with unique and essential functions in the development of the zebrafish, Danio rerio. *Development*, *123*, 1-36.

Haleem, S., & Nnadi, C. (2018). Scoliosis: a review. *Pediatr Child Health*, *28*(5), 209-217.

Hamada, H. (2020). Molecular and cellular basis of left-right asymmetry in vertebrates. *Proc Jpn Acad Ser B Phys Biol Sci*, *96*(7), 273-296. https://doi.org/10.2183/pjab.96.021

Hou, Y., & Witman, G. B. (2017). The N-terminus of IFT46 mediates intraflagellar transport of outer arm dynein and its cargo-adaptor ODA16. *Mol Biol Cell*, *28*(18), 2420-2433. https://doi.org/10.1091/mbc.E17-03-0172

Huh, S., Eun, L. Y., Kim, N. K., Jung, J. W., Choi, J. Y., & Kim, H. S. (2015). Cardiopulmonary function and scoliosis severity in idiopathic scoliosis children. *Korean J Pediatr*, *58*(6), 218-223. https://doi.org/10.3345/kjp.2015.58.6.218

Ishikawa, T., Ueno, H., Omori, T., & Kikuchi, K. (2021). Cilia and centrosomes: Ultrastructural and mechanical perspectives. *Seminars in Cell & Developmental Biology*, *110*, 61-69. https://doi.org/https://doi.org/10.1016/j.semcdb.2020.03.007

Jaffe, K. M., Grimes, D. T., Schottenfeld-Roames, J., Werner, M. E., Ku, T. S., Kim, S. K., Pelliccia, J. L., Morante, N. F., Mitchell, B. J., & Burdine, R. D. (2016). c21orf59/kurly Controls Both Cilia Motility and Polarization. *Cell Rep*, *14*(8), 1841-1849. https://doi.org/10.1016/j.celrep.2016.01.069

Janicki, J. A., & Alman, B. (2007). Scoliosis: Review of diagnosis and treatment. *Pediatr Child Health*, *12*(9), 771-776.

Janssen, M. M., de Wilde, R. F., Kouwenhoven, J. W., & Castelein, R. M. (2011). Experimental animal models in scoliosis research: a review of the literature. *Spine J*, *11*(4), 347-358. https://doi.org/10.1016/j.spinee.2011.03.010

Jao, L. E., Wente, S. R., & Chen, W. (2013). Efficient multiplex biallelic zebrafish genome editing using a CRISPR nuclease system. *Proc Natl Acad Sci U S A*, *110*(34), 13904-13909. https://doi.org/10.1073/pnas.1308335110

Jeong, I., Hansen, J. N., Wachten, D., & Jurisch-Yaksi, N. (2022). Measurement of ciliary beating and fluid flow in the zebrafish adult telencephalon. *STAR Protoc*, *3*(3), 101542. https://doi.org/10.1016/j.xpro.2022.101542

Jin, S. C., Homsy, J., Zaidi, S., Lu, Q., Morton, S., DePalma, S. R., Zeng, X., Qi, H., Chang, W., Sierant, M. C., Hung, W. C., Haider, S., Zhang, J., Knight, J., Bjornson, R. D., Castaldi, C., Tikhonoa, I. R., Bilguvar, K., Mane, S. M., . . . Brueckner, M. (2017). Contribution of rare inherited and de novo variants in 2,871 congenital heart disease probands. *Nat Genet*, *49*(11), 1593-1601. https://doi.org/10.1038/ng.3970

Kass, G. E., & Orrenius, S. (1999). Calcium signaling and cytotoxicity. *Environmental Health Perspectives*, *107*(suppl 1), 25-35. https://doi.org/10.1289/ehp.99107s125

Kathiriya, I. S., & Srivastava, D. (2000). Left-right asymmetry and cardiac looping: implications for cardiac development and congenital heart disease. *Am J Med Genet*, *97*(4), 271-279. https://doi.org/10.1002/1096-8628(200024)97:4<271::aid-ajmg1277>3.0.co;2-o

Kikinis, R., Pieper, S. D., & Vosburgh, K. G. (2014). 3D Slicer: A Platform for Subject-Specific Image Analysis, Visualization, and Clinical Support. In F. A. Jolesz (Ed.), *Intraoperative Imaging and Image-Guided Therapy* (pp. 277-289). Springer New York. https://doi.org/10.1007/978-1-4614-7657-3_19

King, S. M. (2016). Axonemal Dynein Arms. *Cold Spring Harb Perspect Biol*, *8*(11). https://doi.org/10.1101/cshperspect.a028100

Knobel, K. M., Peden, E. M., & Barr, M. M. (2008). Distinct protein domains regulate ciliary targeting and function of C. elegans PKD-2. *Exp Cell Res*, *314*(4), 825-833. https://doi.org/10.1016/j.yexcr.2007.10.017

Konno, N., Fujii, Y., Imae, H., Kaiya, H., Mukuda, T., Miyazato, M., Matsuda, K., & Uchiyama, M. (2013). Urotensin II receptor (UTR) exists in hyaline chondrocytes: A study of peripheral distribution of UTR in the African clawed frog, Xenopus laevis. *General and Comparative Endocrinology*, *185*, 44-56. https://doi.org/https://doi.org/10.1016/j.ygcen.2013.01.015

Koulen, P., Cai, Y., Geng, L., Maeda, Y., Nishimura, S., Witzgall, R., Ehrlich, B. E., & Somlo, S. (2002). Polycystin-2 is an intracellular calcium release channel. *Nat Cell Biol*, *4*(3), 191-197. https://doi.org/10.1038/ncb754

Kozminski, K. G., Johnson, K. A., Forscher, P., & Rosenbaum, J. L. (1993). A motility in the eukaryotic flagellum unrelated to flagellar beating. *Proceedings of the National Academy of Sciences*, *90*(12), 5519-5523. https://doi.org/doi:10.1073/pnas.90.12.5519

Kramer-Zucker, A. G., Olale, F., Haycraft, C. J., Yoder, B. K., Schier, A. F., & Drummond, I. A. (2005). Cilia-driven fluid flow in the zebrafish pronephros, brain and Kupffer's vesicle is required for normal organogenesis. *Development*, *132*(8), 1907-1921. https://doi.org/10.1242/dev.01772

Kumar, D., & Reiter, J. (2021). How the centriole builds its cilium: of mothers, daughters, and the acquisition of appendages. *Curr Opin Struct Biol*, *66*, 41-48. https://doi.org/10.1016/j.sbi.2020.09.006

Labarrere, P., Chatenet, D., Leprince, J., Marionneau, C., Loirand, G., Tonon, M. C., Dubessy, C., Scalbert, E., Pfeiffer, B., Renard, P., Calas, B., Pacaud, P., & Vaudry, H. (2003). Structure-activity relationships of human urotensin II and related analogues on rat aortic ring contraction. *J Enzyme Inhib Med Chem*, *18*(2), 77-88. https://doi.org/10.1080/1475636031000093507

Le Corre, S., Eyre, D., & Drummond, I. A. (2014). Modulation of the secretory pathway rescues zebrafish polycystic kidney disease pathology. *J Am Soc Nephrol*, *25*(8), 1749-1759. https://doi.org/10.1681/ASN.2013101060

Lechtreck, K. F. (2015). IFT-Cargo Interactions and Protein Transport in Cilia. *Trends Biochem Sci*, *40*(12), 765-778. https://doi.org/10.1016/j.tibs.2015.09.003

Leigh, M. W., Pittman, J. E., Carson, J. L., Ferkol, T. W., Dell, S. D., Davis, S. D., Knowles, M. R., & Zariwala, M. A. (2009). Clinical and genetic aspects of primary ciliary dyskinesia/Kartagener syndrome. *Genet Med*, *11*(7), 473-487. https://doi.org/10.1097/GIM.0b013e3181a53562

Lesko, S. L., & Rouhana, L. (2020). Dynein assembly factor with WD repeat domains 1 (DAW1) is required for the function of motile cilia in the planarian Schmidtea mediterranea. *Dev Growth Differ*, *62*(6), 423-437. https://doi.org/10.1111/dgd.12669

Leslie, J. S., Hjeij, R., Vivante, A., Bearce, E. A., Dyer, L., Wang, J., Rawlins, L., Kennedy, J., Ubeyratna, N., Fasham, J., Irons, Z. H., Craig, S. B., Koenig, J., George, S., Pode-Shakked, B., Bolkier, Y., Barel, O., Mane, S., Frederiksen, K. K., . . . Baple, E. L. (2022). Biallelic DAW1 variants cause a motile ciliopathy characterized by laterality defects and subtle ciliary beating abnormalities. *Genet Med*, *24*(11), 2249-2261. https://doi.org/10.1016/j.gim.2022.07.019

Levin, M. (2021). Life, death, and self: Fundamental questions of primitive cognition viewed through the lens of body plasticity and synthetic organisms. *Biochem Biophys Res Commun*, *564*, 114-133. https://doi.org/10.1016/j.bbrc.2020.10.077

Little, R. B., & Norris, D. P. (2021). Right, left and cilia: How asymmetry is established. *Seminars in Cell & Developmental Biology*, *110*, 11-18. https://doi.org/https://doi.org/10.1016/j.semcdb.2020.06.003

Liu, Q., Pong, S.-S., Zeng, Z., Zhang, Q., Howard, A. D., Williams, D. L., Davidoff, M., Wang, R., Austin, C. P., McDonald, T. P., Bai, C., George, S. R., Evans, J. F., & Caskey, C. T. (1999). Identification of Urotensin II as the Endogenous Ligand for the Orphan G-Protein-Coupled Receptor GPR14. *Biochemical and Biophysical Research Communications*, *266*(1), 174-178. https://doi.org/https://doi.org/10.1006/bbrc.1999.1796

Lu, H., Shagirova, A., Goggi, J. L., Yeo, H. L., & Roy, S. (2020). Reissner fibre-induced urotensin signalling from cerebrospinal fluid-contacting neurons prevents scoliosis of the vertebrate spine. *Biol Open*, *9*(5). https://doi.org/10.1242/bio.052027

Mangos, S., Lam, P. Y., Zhao, A., Liu, Y., Mudumana, S., Vasilyev, A., Liu, A., & Drummond, I. A. (2010). The ADPKD genes pkd1a/b and pkd2 regulate extracellular matrix formation. *Dis Model Mech*, *3*(5-6), 354-365. https://doi.org/10.1242/dmm.003194

Marie-Hardy, L., Cantaut-Belarif, Y., Pietton, R., Slimani, L., & Pascal-Moussellard, H. (2021). The orthopedic characterization of cfap298(tm304) mutants validate zebrafish to faithfully model human AIS. *Sci Rep*, *11*(1), 7392. https://doi.org/10.1038/s41598-021-86856-1

McGrath, J., Somlo, S., Makova, S., Tian, X., & Brueckner, M. (2003). Two populations of node monocilia initiate left-right asymmetry in the mouse. *Cell*, *114*(1), 61-73. https://doi.org/10.1016/s0092-8674(03)00511-7

Moreno-Mateos, M. A., Vejnar, C. E., Beaudoin, J. D., Fernandez, J. P., Mis, E. K., Khokha, M. K., & Giraldez, A. J. (2015). CRISPRscan: designing highly efficient sgRNAs for CRISPR-Cas9 targeting in vivo. *Nat Methods*, *12*(10), 982-988. https://doi.org/10.1038/nmeth.3543

Nauli, S. M., Alenghat, F. J., Luo, Y., Williams, E., Vassilev, P., Li, X., Elia, A. E., Lu, W., Brown, E. M., Quinn, S. J., Ingber, D. E., & Zhou, J. (2003). Polycystins 1 and 2 mediate mechanosensation in the primary cilium of kidney cells. *Nat Genet*, *33*(2), 129-137. https://doi.org/10.1038/ng1076

Nauli, S. M., & Zhou, J. (2004). Polycystins and mechanosensation in renal and nodal cilia. *Bioessays*, *26*(8), 844-856. https://doi.org/10.1002/bies.20069

Newman, L., Chopra, J., Dossett, C., Shepherd, E., Bercusson, A., Carroll, M., Walker, W., Lucas, J. S., & Cheong, Y. (2023). The impact of primary ciliary dyskinesia on female and male fertility: a narrative review. *Hum Reprod Update*, *29*(3), 347-367. https://doi.org/10.1093/humupd/dmad003

Nobata, S., Donald, J. A., Balment, R. J., & Takei, Y. (2011). Potent cardiovascular effects of homologous urotensin II (UII)-related peptide and UII in unanesthetized eels after peripheral and central injections. *Am J Physiol Regul Integr Comp Physiol*, *300*(2), R437-446. https://doi.org/10.1152/ajpregu.00629.2010

Nonaka, S., Tanaka, Y., Okada, Y., Takeda, S., Harada, A., Kanai, Y., Kido, M., & Hirokawa, N. (1998). Randomization of Left&#x2013;Right Asymmetry due to Loss of Nodal Cilia Generating Leftward Flow of Extraembryonic Fluid in Mice Lacking KIF3B Motor Protein. *Cell*, *95*(6), 829-837. https://doi.org/10.1016/S0092-8674(00)81705-5

Nothacker, H.-P., Wang, Z., McNeill, A. M., Saito, Y., Merten, S., O'Dowd, B., Duckles, S. P., & Civelli, O. (1999). Identification of the natural ligand of an orphan G-protein-coupled receptor involved in the regulation of vasoconstriction. *Nature Cell Biology*, *1*(6), 383-385. https://doi.org/10.1038/14081

Oda, T., Yanagisawa, H., Kamiya, R., & Kikkawa, M. (2014). A molecular ruler determines the repeat length in eukaryotic cilia and flagella. *Science*, *346*(6211), 857-860. https://doi.org/doi:10.1126/science.1260214

Olstad, E. W., Ringers, C., Hansen, J. N., Wens, A., Brandt, C., Wachten, D., Yaksi, E., & Jurisch-Yaksi, N. (2019). Ciliary Beating Compartmentalizes Cerebrospinal Fluid Flow in the Brain and Regulates Ventricular Development. *Curr Biol*, *29*(2), 229-241 e226. https://doi.org/10.1016/j.cub.2018.11.059

Oltean, A., Schaffer, A. J., Bayly, P. V., & Brody, S. L. (2018). Quantifying Ciliary Dynamics during Assembly Reveals Stepwise Waveform Maturation in Airway Cells. *Am J Respir Cell Mol Biol*, *59*(4), 511-522. https://doi.org/10.1165/rcmb.2017-0436OC

Omran, H., Kobayashi, D., Olbrich, H., Tsukahara, T., Loges, N. T., Hagiwara, H., Zhang, Q., Leblond, G., O'Toole, E., Hara, C., Mizuno, H., Kawano, H., Fliegauf, M., Yagi, T., Koshida, S., Miyawaki, A., Zentgraf, H., Seithe, H., Reinhardt, R., . . . Takeda, H. (2008). Ktu/PF13 is required for cytoplasmic pre-assembly of axonemal dyneins. *Nature*, *456*(7222), 611-616. https://doi.org/10.1038/nature07471

Orts-Del'Immagine, A., Kastner, A., Tillement, V., Tardivel, C., Trouslard, J., & Wanaverbecq, N. (2014). Morphology, distribution and phenotype of polycystin kidney disease 2-like 1-positive cerebrospinal fluid contacting neurons in the brainstem of adult mice. *PLoS One*, *9*(2), e87748. https://doi.org/10.1371/journal.pone.0087748

Parmentier, C., Hameury, E., Dubessy, C., Quan, F. B., Habert, D., Calas, A., Vaudry, H., Lihrmann, I., & Tostivint, H. (2011). Occurrence of two distinct urotensin II-related peptides in zebrafish provides new insight into the evolutionary history of the urotensin II gene family. *Endocrinology*, *152*(6), 2330-2341. https://doi.org/10.1210/en.2010-1500

Peeters, H., & Devriendt, K. (2006). Human laterality disorders. *Eur J Med Genet*, *49*(5), 349-362. https://doi.org/10.1016/j.ejmg.2005.12.003

Petersen, L. K., & Stowers, R. S. (2011). A Gateway MultiSite recombination cloning toolkit. *PLoS One*, *6*(9), e24531. https://doi.org/10.1371/journal.pone.0024531

Puri, B. K. (2020). Calcium Signaling and Gene Expression. In M. S. Islam (Ed.), *Calcium Signaling* (pp. 537-545). Springer International Publishing. https://doi.org/10.1007/978-3-030-12457-1_22

Quan, F. B., Dubessy, C., Galant, S., Kenigfest, N. B., Djenoune, L., Leprince, J., Wyart, C., Lihrmann, I., & Tostivint, H. (2015). Comparative distribution and in vitro activities of the urotensin II-related peptides URP1 and URP2 in zebrafish: evidence for their colocalization in spinal cerebrospinal fluid-contacting neurons. *PLoS One*, *10*(3), e0119290. https://doi.org/10.1371/journal.pone.0119290

Quan, F. B., Gaillard, A. L., Alejevski, F., Pezeron, G., & Tostivint, H. (2021). Urotensin II-related peptide (Urp) is expressed in motoneurons in zebrafish, but is dispensable for locomotion in larva. *Peptides*, *146*, 170675. https://doi.org/10.1016/j.peptides.2021.170675

Robinson, J. T., Thorvaldsdóttir, H., Winckler, W., Guttman, M., Lander, E. S., Getz, G., & Mesirov, J. P. (2011). Integrative genomics viewer. *Nature Biotechnology*, *29*(1), 24-26. https://doi.org/10.1038/nbt.1754

Rodríguez, E. M., Rodríguez, S., & Hein, S. (1998). The subcommissural organ. *Microscopy Research and Technique*, *41*(2), 98-123. https://doi.org/10.1002/(sici)1097-0029(19980415)41:2<98::Aid-jemt2>3.0.Co;2-m

Rolton, D., Nnadi, C., & Fairbank, J. (2014). Scoliosis: a review. *Pediatr Child Health*, *24*(5), 197-203.

Rose, C. D., Pompili, D., Henke, K., Van Gennip, J. L. M., Meyer-Miner, A., Rana, R., Gobron, S., Harris, M. P., Nitz, M., & Ciruna, B. (2020). SCO-Spondin Defects and Neuroinflammation Are Conserved Mechanisms Driving Spinal Deformity across Genetic

Models of Idiopathic Scoliosis. *Curr Biol*, *30*(12), 2363-2373 e2366. https://doi.org/10.1016/j.cub.2020.04.020

Ross, B., McKendy, K., & Giaid, A. (2010). Role of urotensin II in health and disease. *Am J Physiol Regul Integr Comp Physiol*, *298*(5), R1156-1172. https://doi.org/10.1152/ajpregu.00706.2009

Rossi, A., Kontarakis, Z., Gerri, C., Nolte, H., Holper, S., Kruger, M., & Stainier, D. Y. (2015). Genetic compensation induced by deleterious mutations but not gene knockdowns. *Nature*, *524*(7564), 230-233. https://doi.org/10.1038/nature14580

Schindelin, J., Arganda-Carreras, I., Frise, E., Kaynig, V., Longair, M., Pietzsch, T., Preibisch, S., Rueden, C., Saalfeld, S., Schmid, B., Tinevez, J. Y., White, D. J., Hartenstein, V., Eliceiri, K., Tomancak, P., & Cardona, A. (2012). Fiji: an open-source platform for biological-image analysis. *Nat Methods*, *9*(7), 676-682. https://doi.org/10.1038/nmeth.2019

Schottenfeld, J., Sullivan-Brown, J., & Burdine, R. D. (2007). Zebrafish curly up encodes a Pkd2 ortholog that restricts left-side-specific expression of southpaw. *Development*, *134*(8), 1605-1615. https://doi.org/10.1242/dev.02827

Shakil, H., Iqbal, Z. A., & Al-Ghadir, A. H. (2014). Scoliosis: review of types of curves, etiological theories and conservative treatment. *J Back Musculoskelet Rehabil*, *27*(2), 111-115. https://doi.org/10.3233/BMR-130438

Sharif-Naeini, R., Folgering, J. H., Bichet, D., Duprat, F., Lauritzen, I., Arhatte, M., Jodar, M., Dedman, A., Chatelain, F. C., Schulte, U., Retailleau, K., Loufrani, L., Patel, A., Sachs, F., Delmas, P., Peters, D. J., & Honore, E. (2009). Polycystin-1 and -2 dosage regulates pressure sensing. *Cell*, *139*(3), 587-596. https://doi.org/10.1016/j.cell.2009.08.045

Smith, K. A., Chocron, S., von der Hardt, S., de Pater, E., Soufan, A., Bussmann, J., Schulte-Merker, S., Hammerschmidt, M., & Bakkers, J. (2008). Rotation and asymmetric development of the zebrafish heart requires directed migration of cardiac progenitor cells. *Dev Cell*, *14*(2), 287-297. https://doi.org/10.1016/j.devcel.2007.11.015

Solomon, G. M., Francis, R., Chu, K. K., Birket, S. E., Gabriel, G., Trombley, J. E., Lemke, K. L., Klena, N., Turner, B., Tearney, G. J., Lo, C. W., & Rowe, S. M. (2017). Assessment of ciliary phenotype in primary ciliary dyskinesia by micro-optical coherence tomography. *JCI Insight*, *2*(5), e91702. https://doi.org/10.1172/jci.insight.91702

Spassky, N., & Meunier, A. (2017). The development and functions of multiciliated epithelia. *Nat Rev Mol Cell Biol*, *18*(7), 423-436. https://doi.org/10.1038/nrm.2017.21

Stainier, D. Y. R., Raz, E., Lawson, N. D., Ekker, S. C., Burdine, R. D., Eisen, J. S., Ingham, P. W., Schulte-Merker, S., Yelon, D., Weinstein, B. M., Mullins, M. C., Wilson, S. W., Ramakrishnan, L., Amacher, S. L., Neuhauss, S. C. F., Meng, A., Mochizuki, N., Panula, P., & Moens, C. B. (2017). Guidelines for morpholino use in zebrafish. *PLoS Genet*, *13*(10), e1007000. https://doi.org/10.1371/journal.pgen.1007000

Sternberg, J. R., Prendergast, A. E., Brosse, L., Cantaut-Belarif, Y., Thouvenin, O., Orts-Del'Immagine, A., Castillo, L., Djenoune, L., Kurisu, S., McDearmid, J. R., Bardet, P. L., Boccara, C., Okamoto, H., Delmas, P., & Wyart, C. (2018). Pkd2l1 is required for mechanoception in cerebrospinal fluid-contacting neurons and maintenance of spine curvature. *Nat Commun*, *9*(1), 3804. https://doi.org/10.1038/s41467-018-06225-x

Stooke-Vaughan, G. A., Huang, P., Hammond, K. L., Schier, A. F., & Whitfield, T. T. (2012). The role of hair cells, cilia and ciliary motility in otolith formation in the zebrafish otic vesicle. *Development*, *139*(10), 1777-1787. https://doi.org/10.1242/dev.079947

Su, Q., Hu, F., Ge, X., Lei, J., Yu, S., Wang, T., Zhou, Q., Mei, C., & Shi, Y. (2018). Structure of the human PKD1-PKD2 complex. *Science*, *361*(6406). https://doi.org/10.1126/science.aat9819

Sugo, T., Murakami, Y., Shimomura, Y., Harada, M., Abe, M., Ishibashi, Y., Kitada, C., Miyajima, N., Suzuki, N., Mori, M., & Fujino, M. (2003). Identification of urotensin II-related peptide as the urotensin II-immunoreactive molecule in the rat brain. *Biochemical and Biophysical Research Communications*, *310*(3), 860-868. https://doi.org/https://doi.org/10.1016/j.bbrc.2003.09.102

Sullivan-Brown, J., Schottenfeld, J., Okabe, N., Hostetter, C. L., Serluca, F. C., Thiberge, S. Y., & Burdine, R. D. (2008). Zebrafish mutations affecting cilia motility share similar cystic phenotypes and suggest a mechanism of cyst formation that differs from pkd2 morphants. *Dev Biol*, *314*(2), 261-275. https://doi.org/10.1016/j.ydbio.2007.11.025

Sun, Z., Amsterdam, A., Pazour, G. J., Cole, D. G., Miller, M. S., & Hopkins, N. (2004). A genetic screen in zebrafish identifies cilia genes as a principal cause of cystic kidney. *Development*, *131*(16), 4085-4093. https://doi.org/10.1242/dev.01240

Sung, S., Chae, H. W., Lee, H. S., Kim, S., Kwon, J. W., Lee, S. B., Moon, S. H., Lee, H. M., & Lee, B. H. (2021). Incidence and Surgery Rate of Idiopathic Scoliosis: A Nationwide Database Study. *Int J Environ Res Public Health*, *18*(15). https://doi.org/10.3390/ijerph18158152

Swinburne, I. A., Mosaliganti, K. R., Green, A. A., & Megason, S. G. (2015). Improved Long-Term Imaging of Embryos with Genetically Encoded alpha-Bungarotoxin. *PLoS One*, *10*(8), e0134005. https://doi.org/10.1371/journal.pone.0134005

Sztal, T. E., & Stainier, D. Y. R. (2020). Transcriptional adaptation: a mechanism underlying genetic robustness. *Development*, *147*(15). https://doi.org/10.1242/dev.186452

Taschner, M., Mourao, A., Awasthi, M., Basquin, J., & Lorentzen, E. (2017). Structural basis of outer dynein arm intraflagellar transport by the transport adaptor protein ODA16 and the intraflagellar transport protein IFT46. *J Biol Chem*, *292*(18), 7462-7473. https://doi.org/10.1074/jbc.M117.780155

Tavares, B., Jacinto, R., Sampaio, P., Pestana, S., Pinto, A., Vaz, A., Roxo-Rosa, M., Gardner, R., Lopes, T., Schilling, B., Henry, I., Saude, L., & Lopes, S. S. (2017). Notch/Her12 signalling modulates, motile/immotile cilia ratio downstream of Foxj1a in zebrafish left-right organizer. *Elife*, *6*. https://doi.org/10.7554/eLife.25165

Terhune, E. A., Monley, A. M., Cuevas, M. T., Wethey, C. I., Gray, R. S., & Hadley-Miller, N. (2022). Genetic animal modeling for idiopathic scoliosis research: history and considerations. *Spine Deform*, *10*(5), 1003-1016. https://doi.org/10.1007/s43390-022-00488-7

Thouvenin, O., Keiser, L., Cantaut-Belarif, Y., Carbo-Tano, M., Verweij, F., Jurisch-Yaksi, N., Bardet, P.-L., Niel, G. V., Gallaire, F., & Wyart, C. (2019). Origin of the bidirectionality of cerebrospinal fluid flow and impact on longrange transport between brain and spinal cord. *BioRxiv*. https://doi.org/10.1101/627166

Tostivint, H., Joly, L., Lihrmann, I., Parmentier, C., Lebon, A., Morisson, M., Calas, A., Ekker, M., & Vaudry, H. (2006). Comparative genomics provides evidence for close evolutionary relationships between the urotensin II and somatostatin gene families. *Proc Natl Acad Sci U S A*, *103*(7), 2237-2242. https://doi.org/10.1073/pnas.0510700103

Troutwine, B. R., Gontarz, P., Konjikusic, M. J., Minowa, R., Monstad-Rios, A., Sepich, D. S., Kwon, R. Y., Solnica-Krezel, L., & Gray, R. S. (2020). The Reissner Fiber Is Highly Dynamic In Vivo and Controls Morphogenesis of the Spine. *Curr Biol*, *30*(12), 2353-2362 e2353. https://doi.org/10.1016/j.cub.2020.04.015

Vaudry, H., Do Rego, J. C., Le Mevel, J. C., Chatenet, D., Tostivint, H., Fournier, A., Tonon, M. C., Pelletier, G., Conlon, J. M., & Leprince, J. (2010). Urotensin II, from fish to human. *Ann N Y Acad Sci*, *1200*, 53-66. https://doi.org/10.1111/j.1749-6632.2010.05514.x

Walker, R. V., Keynton, J. L., Grimes, D. T., Sreekumar, V., Williams, D. J., Esapa, C., Wu, D., Knight, M. M., & Norris, D. P. (2019). Ciliary exclusion of Polycystin-2 promotes kidney cystogenesis in an autosomal dominant polycystic kidney disease model. *Nat Commun*, *10*(1), 4072. https://doi.org/10.1038/s41467-019-12067-y

Wallmeier, J., Nielsen, K. G., Kuehni, C. E., Lucas, J. S., Leigh, M. W., Zariwala, M. A., & Omran, H. (2020). Motile ciliopathies. *Nature Reviews Disease Primers*, *6*(1), 77. https://doi.org/10.1038/s41572-020-0209-6

Wang, G., Xu, Y., Wang, Q., Chai, Y., Sun, X., Yang, F., Zhang, J., Wu, M., Liao, X., Yu, X., Sheng, X., Liu, Z., & Zhang, J. (2022). Rare and undiagnosed diseases: From disease-causing gene identification to mechanism elucidation. *Fundamental Research*, *2*(6), 918-928. https://doi.org/10.1016/j.fmre.2022.09.002

Wang, J., Taschner, M., Petriman, N. A., Andersen, M. B., Basquin, J., Bhogaraju, S., Vetter, M., Wachter, S., Lorentzen, A., & Lorentzen, E. (2020). Purification and crystal structure of human ODA16: Implications for ciliary import of outer dynein arms by the intraflagellar transport machinery. *Protein Sci*, *29*(6), 1502-1510. https://doi.org/10.1002/pro.3864

Wang, Y., Troutwine, B. R., Zhang, H., & Gray, R. S. (2022). The axonemal dynein heavy chain 10 gene is essential for monocilia motility and spine alignment in zebrafish. *Dev Biol*, *482*, 82-90. https://doi.org/10.1016/j.ydbio.2021.12.001

Waters, A. M., & Beales, P. L. (2011). Ciliopathies: an expanding disease spectrum. *Pediatr Nephrol*, *26*(7), 1039-1056. https://doi.org/10.1007/s00467-010-1731-7

Weiss, H.-R. M., Marc. (2016). Congenital Scoliosis (Mini-review). *Current Pediatric Reviews*, *12*, 43-47.

Wu, G., Markowitz, G. S., Li, L., D'Agati, V. D., Factor, S. M., Geng, L., Tibara, S., Tuchman, J., Cai, Y., Hoon Park, J., van Adelsberg, J., Hou, H., Kucherlapati, R., Edelmann, W., & Somlo, S. (2000). Cardiac defects and renal failure in mice with targeted mutations in Pkd2. *Nature Genetics*, *24*(1), 75-78. https://doi.org/10.1038/71724

Wu, R. S., Lam, II, Clay, H., Duong, D. N., Deo, R. C., & Coughlin, S. R. (2018). A Rapid Method for Directed Gene Knockout for Screening in G0 Zebrafish. *Dev Cell*, *46*(1), 112-125 e114. https://doi.org/10.1016/j.devcel.2018.06.003

Yamaguchi, H., Oda, T., Kikkawa, M., & Takeda, H. (2018). Systematic studies of all PIH proteins in zebrafish reveal their distinct roles in axonemal dynein assembly. *Elife*, *7*. https://doi.org/10.7554/eLife.36979

Yamamoto, S., Kanca, O., Wangler, M. F., & Bellen, H. J. (2024). Integrating non-mammalian model organisms in the diagnosis of rare genetic diseases in humans. *Nat Rev Genet*, *25*(1), 46-60. https://doi.org/10.1038/s41576-023-00633-6

Yoshiba, S., Shiratori, H., Kuo, I. Y., Kawasumi, A., Shinohara, K., Nonaka, S., Asai, Y., Sasaki, G., Belo, J. A., Sasaki, H., Nakai, J., Dworniczak, B., Ehrlich, B. E., Pennekamp, P., & Hamada, H. (2012). Cilia at the node of mouse embryos sense fluid flow for left-right determination via Pkd2. *Science*, *338*(6104), 226-231. https://doi.org/10.1126/science.1222538

Zhang, X., Jia, S., Chen, Z., Chong, Y. L., Xie, H., Feng, D., Wu, X., Song, D. Z., Roy, S., & Zhao, C. (2018). Cilia-driven cerebrospinal fluid flow directs expression of urotensin neuropeptides to straighten the vertebrate body axis. *Nat Genet*, *50*(12), 1666-1673. https://doi.org/10.1038/s41588-018-0260-3